# Università degli Studi di Cagliari

**DOTTORATO DI RICERCA**

In

**Scienze e Tecnologie Chimiche**

Ciclo XXIV

# Low temperature CO Oxidation and Preferential Oxidation of CO Over Nano-Structured Base Metal Oxide Catalysts

Settore/i scientifico disciplinari di afferenza

**CHIM-04 Chimica Industriale**


| | |
|---|---|
| Presentata da: | **Dott. Shaji varghese** |
| Coordinatore Dottorato: | **Prof. Mariano Casu** |
| Tutor: | **Prof.Italo Ferino** |


Esame finale anno accademico 2010 – 2011

# Low Temperature CO Oxidation and Preferential Oxidation of CO Over Nano-Structured Base Metal Oxide Catalysts

## Thesis

Submitted in partial fulfillment of the requirements of the degree of

**Doctor of Philosophy**

in

Chemical Sciences and Technology

by

**Shaji Varghese**

Under the Guidance of

**Prof. Italo Ferino**


**Department of Chemical Sciences**
**University of Cagliari**
**SS 554 Bivio Sestu 09042**
**Monserrato (CA)**
**ITALY**

**XXIV Cycle 2009-2011**

*Dedicated to my beloved parents and teachers*

## ACKNOWLEDGEMENTS

*I would like to gratefully acknowledge the following individuals for their assistance, support, guidance and inspiration during the time I have worked on this research.*

*My Supervisor:*

Prof. Italo Ferino

*My PhD Coordinator:*

Prof. Mariano Casu

*My Advisors:*

Prof. Roberto Monaci

Dott.ssa. E. Rombi

Dott.ssa. M.G. Cutrufello

Dott.ssa. Carla Cannas

*My Labmates:*

Dott.ssa. Daniela Meloni

Dott.ssa. Franca Sini

Dott.ssa. Valentina Spano

Dott.ssa. Zelda Zette

Dott.ssa. Sarah Lai

*The Department Staff:*

Dott.ssa. Silvia Porceda

Dott.ssa. Alexandra Pirras

Dott. Davide Peddis

Dott. Andrea Ardu

Dott. Maurizio Loi

All friends in Sala Dottorandi

*My family, teachers and friends, as well as everyone else I've met along the way.*

# Table of Contents


| Chapter | Title | Page No. |
|---|---|---|
| | Table of Contents | i |
| | List of Figures | viii |
| | List of Tables | xv |
| | List of Schemes | xvii |
| **1** | **State of the Art** | **1** |
| | 1.1 Hydrogen as an energy carrier | 2 |
| | 1.2 Hydrogen production | 4 |
| | 1.2.1 Steam Reforming | 5 |
| | 1.2.2 Partial Oxidation | 7 |
| | 1.2.3 Autothermal Reforming | 8 |
| | 1.3 Water Gas Shift Reaction | 9 |
| | 1.3.1 Thermodynamics | 10 |
| | 1.3.2 High Temperature Shift | 13 |
| | 1.3.3 Low Temperature Shift | 14 |
| | 1.4 Low Temperature Removal of Carbon Monoxide | 16 |

1.4.1 Low Temperature Oxidation of Carbon Monoxide 17

1.4.1.1 Noble Metal Reducible Oxide Catalysts 17

1.4.1.2 Gold Based Catalysts 18

1.4.1.3 Base Metal Oxide Catalysts 19

1.4.1.3.1 Unsupported Metal Oxide Catalysts 19

1.4.1.3.2 Supported Metal Oxide Catalysts 20

1.5 Preferential Oxidation of Carbon Monoxide 21

1.5.1 Catalysts for CO-PROX 22

1.5.1.1 Supported Noble Metal Catalysts 22

1.5.1.2 Nano-Gold Catalysts 24

1.5.1.3 Base Metal Oxide Catalyst 26

1.6 Conclusions 29

1.7 Outline of the Thesis 30

References 32

**2 Materials and Methods 44**

2.1 Introduction 44

2.2 Catalysts Development using Hard Template Method 45

2.2.1 The Hard Template Method 46

2.2.2 The Procedure of Hard Template Method 47

2.2.3 Factors Affecting Hard Template Method 48

2.2.3.1 Hydrogen Bonding 48

2.2.3.2 Co-ordination Bonding 48

2.2.3.3 Coulombic Interactions 48

2.2.3.4 Van-der Walls Forces 49

2.2.4 Advantages of Hard Template Method 49

2.3 Experimental Setup for Low Temperature CO Oxidation (LT-CO) and Preferential Oxidation of CO (PROX-CO) 49

References 51

**3 Low temperature CO oxidation and preferential oxidation of CO over CuO-$Co_3O_4$ spinel catalysts 53**

3.1 Introduction 53

3.2 Experimental 56

3.2.1 Materials 56

3.2.2 Synthesis of Mesoporous Silica SBA-15 56

3.2.3 Synthesis of Mesoporous Copper-Cobalt Mixed Oxides 56

3.2.4 Catalyst Characterization 57

3.2.5 Catalytic Rruns 58

3.3 Results and Discussion 59

3.3.1 Characterization of SBA-15 59

3.3.2 Characterization of CuCo-*x* Catalysts 61

3.4 Catalytic Activity of CuCo-*x* Catalysts 67

3.4.1 CO Oxidation in the Absence of $H_2$ 67

3.4.2 Preferential Oxidation of CO (PROX-CO) 70

3.5 Conclusions 77

References 78

**4 Low temperature CO oxidation and preferential oxidation of CO over $Fe_2O_3$-$Co_3O_4$ binary system 82**

4.1 Introduction 82

4.2 Experimental 83

4.2.1 Materials 83

4.2.2 Synthesis of Mesoporous Silica SBA-15 83

4.2.3 Synthesis of Mesoporous Iron-Cobalt Mixed Oxides 84

4.2.4 Gold deposition on $Fe_2O_3$- $Co_3O_4$ support 84

4.2.5 Catalyst characterization 84

4.2.6 Catalytic runs 85

4.3 Results and Discussion 86

4.3.1 Characterisation of SBA-15 86

4.3.2 Characterization of the FeCo-*x* catalysts 88

4.4 Catalytic activity of FeCo-*x* catalysts 94

4.4.1 CO Oxidation in the Absence of $H_2$ 94

4.4.2 Preferential oxidation of CO (PROX-CO) 95

4.5 Conclusions 99

References 100

**5 Low temperature CO oxidation and preferential oxidation of CO over mesoporous CuO-$CeO_2$ catalysts 102**

5.1 Introduction 102

5.1.2 Structural Properties of Ceria 103

5.2 Experimental 105

5.2.1 Materials 105

5.2.2 Synthesis of Mesoporous Silica SBA-15 106

5.2.3 Synthesis of mesoporous Cu-Ce catalysts 106

5.2.4 Characterisation 106

5.2.5 Catalytic runs 107

5.3 Results and Discussion 108

5.3.1 Characterization of SBA-15 108

5.3.2 Characterization of $Cu_xCe$ catalysts 110

5.4 Catalytic activity of $Cu_xCe$ catalysts 115

5.4.1 CO oxidation activity in the absence of $H_2$ 115

5.4.2 Preferential oxidation of CO (PROX-CO) 117

5.5 Conclusions 119

References 120

**6 Low temperature CO oxidation and preferential oxidation of CO over mesoporous $CuO/CeO_2$-$Fe_2O_3$ catalysts** **123**

6.1 Introduction 123

6.2 Experimental 124

6.2.1 Materials 124

6.2.2 Synthesis of Mesoporous Silica SBA-15 125

6.2.3 Preparation of Ceria-Iron Bimetal Oxides 125

6.2.4 Copper Deposition on $CeO_2$-$Fe_2O_3$ Support 126

6.2.5 Gold Deposition on $CeO_2$-$Fe_2O_3$ Support 126

6.2.6 Characterization 126

6.2.7 Catalytic Runs 127

6.3 Results and Discussion 128

6.3.1 Characterization of SBA-15 128

6.3.2 Characterization of CuO/CeFe-*25* catalysts 130

6.4 Catalytic activity of CuO/CeFe-*25* 135

6.4.1 CO oxidation activity in the absence of $H_2$ 135

6.4.2 Preferential oxidation of CO(PROX-CO) 137

6.5 Conclusions 141

References 142

**7 Summary and Conclusions 144**

# List of Figures


| No. | Caption | Page No. |
|---|---|---|
| Figure 1.1 | PEM fuel cell | 3 |
| Figure 1.2 | Schematic representation of an industrial hydrogen generation for ammonia synthesis | 10 |
| Figure 1.3 | Effects of S/G ratios at various temperatures on HTS (a) and LTS (b) equilibrium CO concentrations: gas from autothermal reformer | 11 |
| Figure 1.4 | Effect of $H_2$ concentration on CO equilibrium of HTS (a) and LTS (b): Autothermal vs steam methane reformer (SMR) | 12 |
| Figure 1.5 | Schematic representation of the fuel processor for PEMFC | 22 |
| Figure 2.1 | Schematic representation of the hard template concept | 74 |
| Figure 2.2 | Schematic representation of “wet impregnation” and “incipient wetness impregnation” techniques for the infiltration of precursor species into porous structure matrices | 47 |
| Figure 2.3 | Experimental setup for low temperature CO oxidation and preferential oxidation of CO | 50 |
| Figure 3.1 | Schematic representation of the unit cell $AB_2X_4$ | 54 |
| Figure 3.2 | Schematic representation of the polyhedral model of $Co_3O_4$ spinel | 55 |
| Figure 3.3 | Low angle XRD diffraction of the SBA-15 silica template | 59 |

| | | |
|---|---|---|
| Figure 3.4 | TEM images of the SBA-15 silica template | 60 |
| Figure 3.5 | Nitrogen adsorption/desorption isotherm and pore size distribution plot (inset) of the SBA-15 silica template | 60 |
| Figure 3.6 | XRD patterns of CuCo-*x* catalysts: (A), CuCo-*0*; (B), CuCo-*9*; (C), CuCo-*13*; (D), CuCo-*17*; (E), CuCo-*17* after $N_2$ treatment at 500 °C for 6 h | 61 |
| Figure 3.7 | FTIR spectra of (A), CuO; (B), CuCo-*0*; (C), CuCo-*17*; (D), CuCo-*17* after $N_2$ treatment at 500 °C for 6 h. | 62 |
| Figure 3.8 | TEM images of the CuCo-*0* (a) and CuCo-*17* (b, c) catalysts | 64 |
| Figure 3.9 | Nitrogen adsorption/desorption isotherm and pore size distribution plot (inset) of CuCo-*x* catalysts: CuCo-*0*, (a); CuCo-*9*, (b); CuCo-*13*, (c); CuCo-*17*, (d) | 65 |
| Figure 3.10 | $H_2$-TPR profiles of (A), CuO; (B), CuCo-*0*; (C), CuCo-*13*;(D), CuCo-*17* | 67 |
| Figure 3.11 | CO conversion vs. reaction temperature for the CuCo-*x* catalysts in the low temperature CO oxidation: (○), CuCo-*0*; (●), CuCo-*9*; (□) CuCo-*13*; (▲) CuCo-*17* | 68 |
| Figure 3.12 | CO conversion vs. reaction temperature for the CuCo-*17* catalyst in the low temperature CO oxidation: (▲) pretreated under air at 500 °C for 1 h; (■) pretreated under air at 150 °C for 1 h; (●) pretreated under $H_2$ at 350 °C for 2 h and then calcined in air for 1 h at the same temperature. | 70 |
| Figure 3.13 | CO PROX activity vs. reaction temperature for CuCo-*0* (○), CuCo-*9* (●), CuCo-*13* (□), and CuCo-*17* (▲): (a), CO conversion; (b), $CO_2$ selectivity from CO; (c), $O_2$ conversion; (d), $CO_2$ selectivity form $O_2$. Catalyst amount: 0.03 g | 71 |
| Figure 3.14 | $O_2$ conversion vs. reaction temperature for CO oxidation (■), $H_2$ oxidation (●), and CO PROX (▲): (a), CuCo-*0*; (b), CuCo-*17*. Catalyst amount: 0.03 g | 73 |

| | | |
|---|---|---|
| Figure 3.15 | Arrhenius plot of the specific rate constant of CO oxidation and $H_2$ oxidation over CuCo-*0* and CuCo-*13* catalysts | 74 |
| Figure 3.16 | CO PROX activity vs. reaction temperature for CuCo-*0* (○;●) and (△,▲) CuCo-*17*: (a), CO conversion; (b), $CO_2$ selectivity from CO; (c), $O_2$ conversion; (d), $CO_2$ selectivity form $O_2$. Catalyst amount: 0.1 g. Open and full symbols refer to fresh and regenerated samples, respectively | 76 |
| Figure 3.17 | FTIR spectra of (A), CuCo-*0* and (B), CuCo-*17* catalysts after CO PROX reaction | 77 |
| Figure 4.1 | Low angle XRD diffraction of SBA-15 silica template | 86 |
| Figure 4.2 | TEM of SBA-15 silica template | 87 |
| Figure 4.3 | Nitrogen adsorption-desorption isotherm and pore size distribution (insight) of SBA-15 silica template. | 88 |
| Figure 4.4 | XRD patterns of FeCo-*x* catalysts: (A), FeCo-0; (B), *FeCo-9*; (C), *FeCo-14*; (D), *FeCo-19*; (E), *2.4Au/FeCo-14* | 89 |
| Figure 4.5 | TEM of FeCo-*x* catalysts: (a), FeCo-0; (b), *FeCo-9*; (c), *FeCo-14*; (d), *FeCo-19* | 90 |
| Figure 4.6 | FTIR spectra of FeCo-*x* catalysts: (A), FeCo-*0* (B), FeCo-9; (C), FeCo-*14*; (D), FeCo-*19*; (E) 2.4 Au/FeCo-14 | 91 |
| Figure 4.7 | FTIR spectra of selected regions of FeCo-*x* catalysts: (A), FeCo-*0;* (B), FeCo-9; (C), FeCo-*14*; (D), FeCo-*19* | 91 |
| Figure 4.8 | $N_2$ adsorption-desorption isotherm and pore size distribution (insight) of (a) FeCo-0, (b) FeCo-*9*, (c) FeCo-*14* and (d) FeCo-*19* catalysts | 92 |
| Figure 4.9 | $H_2$-TPR of FeCo-*x* catalysts: FeCo-*0*, (a); FeCo-*9*, (b); FeCo-*14* (c); FeCo-*19* (d) | 94 |

| | | |
|---|---|---|
| Figure 4.10 | CO conversion *vs.* reaction temperature of the FeCo-*x* catalysts: (□) 2.4 Au/FeCo-14; (○) FeCo-*0*; (■) FeCo-9; (▲) FeCo-*14*; (▼) FeCo-*19* | 95 |
| Figure 4.11 | CO conversion *vs.* reaction temperature of the FeCo-*x* catalysts for PROX-CO: (○) FeCo-*0*; (■) FeCo-*9*; (▲) FeCo-*14*; (▼) FeCo-*19*; (□) *2.4* FeCo-*14*: (a), CO conversion; (b), $CO_2$ selectivity from CO; (c),$O_2$ conversion; (d), $CO_2$ selectivity form $O_2$. Catalyst amount: 0.03 g | 96 |
| Figure 4.12 | CO PROX activity vs. reaction temperature for FeCo-*0* (○;●) and FeCo-*14* (△,▲): (a), CO conversion; (b), $CO_2$ selectivity from CO; (c), $O_2$ conversion; (d), $CO_2$ selectivity form $O_2$. Catalyst amount: 0.1 g. Open and full symbols refer to fresh and regenerated samples, respectively | 97 |
| Figure 4.13 | FTIR spectra of FeCo-*x* catalysts after reaction: (A), FeCo-*0* (B), FeCo-9; (C), FeCo-*14*; (D), FeCo-*19*; (E), 2.4 Au/FeCo-14 | 98 |
| Figure 5.1 | Schematic representation of fcc cell of $CeO_2$ | 103 |
| Figure 5.2 | Proposed pathway for $CeO_2$ surface reduction | 104 |
| Figure 5.3 | Low angle XRD pattern of the SBA-15 silica template | 108 |
| Figure 5.4 | TEM images of the SBA-15 silica template | 109 |
| Figure 5.5 | Nitrogen adsorption/desorption isotherm and pore size distribution plot (inset) of the SBA-15 silica template | 110 |
| Figure 5.6 | XRD patterns of $Cu_xCe$ catalysts: (A), $Cu_{17}Ce$; (B), $Cu_{43}Ce$; (C), $Cu_{76}Ce$ | 111 |

| | | |
|---|---|---|
| Figure 5.7 | Nitrogen adsorption/desorption isotherm and pore size distribution plot (inset) of $Cu_xCe$ catalysts: $Cu_{17}Ce$, (a); $Cu_{43}Ce$, (b); $Cu_{76}Ce$, (c). | 112 |
| Figure 5.8 | $H_2$-TPR profile of (A) CuO, (B) $Cu_{17}Ce$, (C) $Cu_{43}Ce$, (D) $Cu_{76}Ce$ | 114 |
| Figure 5.9 | CO conversion *vs.* reaction temperature of the $Cu_xCe$ catalysts: (▲) $Cu_{17}Ce$; (■) $Cu_{43}Ce$; (♦) *$Cu_{73}Ce$* | 115 |
| Figure 5.10 | Temperature for 50% CO conversion vs CuO mol% | 116 |
| Figure 5.11 | Effect of copper deposition method on preferential CO oxidation of CuO/CeFe-25 catalysts: (▼) $Cu_{17}Ce$, (■) $Cu_{43}Ce$ (♦) $Cu_{76}Ce$: (a), CO conversion; (b), $CO_2$ selectivity from CO; (c), $O_2$ conversion; (d), $CO_2$ selectivity form $O_2$. Catalyst amount: 0.03 g | 118 |
| Figure 6.1 | Low angle XRD pattern of the SBA-15 silica template | 128 |
| Figure 6.2 | TEM images of the SBA-15 silica template | 129 |
| Figure 6.3 | Nitrogen adsorption/desorption isotherm and pore size distribution plot (inset) of the SBA-15 silica template | 129 |
| Figure 6.4 | XRD patterns of CeFe-*25* and CuO / CeFe-*25* catalysts: (A), CeFe-*25*; (B), *8* CuO/CeFe-*25*; (C), *12* CuO/CeFe-*25*; (D), *16* CuO/CeFe-*25*; (E), *24* CuO/CeFe-*25*; (F), *17* CuO/ CeFe-*25* (IWI). | 130 |
| Figure 6.5 | Nitrogen adsorption/desorption isotherm and pore size distribution plot (inset) of CeFe-*25* and CuO/CeFe-*25* catalysts: CeFe-*25*, (a); *8* CuO/CeFe-*25*, (b); *12* CuO/CeFe-*25*, (c); *16* CuO/ CeFe-*25* (d); *24* CuO/ CeFe-*25* (e); *17* CuO/ CeFe-*25* (IWI) (f) | 132 |

| | | |
|---|---|---|
| Figure 6.6 | $H_2$-TPR of CeFe-*25*(A) and CuO/CeFe-*25*(B) catalysts: *8* CuO/CeFe-*25*, (a); *12* CuO/CeFe-*25*, (b); *16* CuO/ CeFe-*25* (c); *24* CuO/ CeFe-*25* (d); *17* CuO/ CeFe-*25* (IWI) (e) | 134 |
| Figure 6.7 | CO conversion *vs.* reaction temperature of the *X* CuO/CeFe-25 catalysts: (■) CeFe-*25*; (●) *8* CuO/CeFe-*25*; (▲) *12* CuO/CeFe-*25*; (▼) *16* CuO/ CeFe-*25*; (♦) *24* CuO/ CeFe-*25*. | 136 |
| Figure 6.8 | Effect of copper deposition method on CO oxidation of CuO/CeFe-25 catalysts: (▼)16 CuO/CeFe-25 (CI), (□) 17CuO/CeFe-25 (IWI). | 136 |
| Figure 6.9 | CO oxidation over (○)1.8 Au/CeFe-25 and (▼) 16 CuO/CeFe-25 (CI) catalysts | 137 |
| Figure 6.10 | CO conversion *vs.* reaction temperature of the *X* CuO/CeFe-25 catalysts for PROX-CO: (■) CeFe-*25*; (●) *8* CuO/CeFe-*25*; (▲) *12* CuO/CeFe-*25*; (▼) *16* CuO/ CeFe-*25*; (♦) *24* CuO/ CeFe-*25*: (a), CO conversion; (b), $CO_2$ selectivity from CO; (c),$O_2$ conversion; (d), $CO_2$ selectivity form $O_2$. Catalyst amount: 0.03 g | 138 |
| Figure 6.11 | Effect of copper deposition method on preferential CO oxidation of CuO/CeFe-25 catalysts: (▼)16 CuO/CeFe-25 (CI), (□) 17CuO/CeFe-25 (IWI): (a), CO conversion; (b), $CO_2$ selectivity from CO; (c), $O_2$ conversion; (d), $CO_2$ selectivity form $O_2$. Catalyst amount: 0.03 g | 139 |
| Figure 6.12 | Preferential oxidation of CO over (○)1.8 Au/CeFe-25 and (▼) 16 CuO/CeFe-25 (CI) catalysts: (a), CO conversion; (b), $CO_2$ selectivity from CO; (c),$O_2$ conversion; (d), $CO_2$ | 140 |

selectivity form $O_2$. Catalyst amount: 0.03 g.

## List of Tables


| No. | Caption | Page No. |
|---|---|---|
| Table 1.1 | Main properties of Hydrogen | 2 |
| Table 1.2 | Characteristics of hydrogen as a fuel | 4 |
| Table 1.3 | Global Hydrogen production | 5 |
| Table 1.4 | Advantages and disadvantages of reforming technologies | 9 |
| Table 1.5 | WGS equilibrium constants at various temperatures | 11 |
| Table 1.6 | Effect of pressure on equilibrium CO concentrations (inlet dry gas: 13.2 % CO, 10.3% $CO_2$, 35.3% $H_2$, 41.2% $N_2$, S/G =0.5) | 12 |
| Table 1.7 | Effect of catalyst preparation method for preferential oxidation of CO over CuO-$CeO_2$ | 28 |
| Table 3.1 | Textural properties of the CuCo-*x* catalysts | 64 |
| Table 3.2 | Comparison of the experimental conditions used for CO oxidation in the present work with those of literature data | 69 |
| Table 4.1 | Textural properties of the FeCo-*x* catalysts | 93 |
| Table 5.1 | Structural parameters of $Cu_xCe$ catalysts | 111 |
| Table 5.2 | Textural properties of the SBA-15 and $Cu_xCe$ catalysts | 113 |
| Table 5.3 | Summary of TPR results over $Cu_xCe$ catalysts | 115 |
| Table 5.4 | Comparison of the preparation method and experimental conditions used for CO oxidation in the present work with | 117 |

those of literature data

Table 6.1 Structural parameters of CeFe-*25* and CuO/CeFe-*25* system 131

Table 6.2 Textural properties of the SBA-15, CeFe-*25* and *X* CuO/CeFe-*25* 131

## List of Schemes


| No. | Caption | Page No. |
|---|---|---|
| Scheme 1.1 | Reactions involved in the steam reforming of methane | 6 |
| Scheme 1.2 | Reactions involved in the steam reforming of methanol | 7 |
| Scheme 1.3 | Reaction mechanism of CO oxidation over $Au/TiO_2$ | 18 |
| Scheme 1.4 | Reaction scheme for the PROX over Pt-M (M= Ni or Co) catalysts | 24 |

CHAPTER

1

# State of the Art

World energy demand is growing with an alarming rate. It is predicted that global energy demand will be about 30 % higher in 2040 compared to 2010. Today's 80% of the world energy supply comes from fossil fuels[1-2]. Globally, about two-thirds of the primary energy uses for transportation and heating accounts more than half of the green house gas emissions and a significant fraction of air pollution. Because of the increasing demand of fuels, most of the energy forecasts project that greenhouse gas emissions and air pollution emissions will grow over the next century. Present atmospheric concentration of greenhouse gases is 30% higher than it was at the beginning of the industrial revolution. The Intergovernmental Panel on Climate Change (IPCC) projects a temperature increase of 1 to 3.5° C, which leads to many harmful environmental consequences[3]. A variety of alternative fuels are proposed for the future those includes methanol, ethanol, synthetic liquids from natural gas or coal and hydrogen. Of these, hydrogen offers the greatest potential environmental and energy supply benefits. Hydrogen is a versatile energy carrier that can be made from a variety of widely available primary energy sources including natural gas, coal, biomass, sunlight, wind and nuclear power[4-5].

## 1.1. Hydrogen as an energy carrier

Hydrogen has the highest energy content per unit mass of any fuel. For example, on a weight basis, hydrogen has nearly three times the energy content of gasoline (140.4 MJ/kg versus 48.6 MJ/kg). However, on a volume basis the situation is reversed: 8,491 $MJ/m^3$ for liquid hydrogen versus 31,150 $MJ/m^3$ for gasoline [6]. Electricity is presently the only energy carrier which does not create environmental impact when used. Hydrogen has the same advantage. Hydrogen is an energy carrier like electricity, not an energy source, but it can be produced from diverse renewable (for instance, wind, solar, geothermal and hydroelectric power to split water) and non- renewable sources (such as coal, natural gas and biomass or using nuclear energy). There are three main important reasons to opt hydrogen as a promising energy carrier of the future. The diversity of supply, which offers as the potential to replace our reliance on limited and insecure energy sources, such as fossil fuels is the first important reason. The second reason is the reduction of environmental impacts of the energy system. The third reason is the control of acceptable costs and the hope of stable price over time. Main properties of hydrogen are reported in table1.1[7-8]

**Table 1.1.** Main properties of Hydrogen[9]

| | |
|---|---|
| Gas density | 0.0899 $kg/Nm^3$ |
| Liquid density | 70.99 $kg/ m^3$ |
| Boiling point | 20.4 K |
| Melting point | 14 K |
| Lower heating value (LHV) | 121 MJ/kg |
| Burning range | 4 – 74.5 % volume |
| Detonation range | 18.3 – 59 % volume |
| Stoechiometric ratio | 34.5 |

Hydrogen gas is the ideal energy carrier, due to its pollutant-free combustion, which produces exclusively energy and water. The use of hydrogen as potential fuel is possible together with PEM fuel cells (Figure 1.1). Fuel cells are electro-chemical devices which transforms chemical energy to electrical energy with high efficiency.

Hydrogen can power highly efficient fuel cells that generate both electricity and heat with no emissions, other than pure, drinkable water. Hydrogen represents one of the few substitutes for oil as a transportation fuel that will not contribute to global warming- if generated by renewable sources, such as wind power, or even by coal, should the capture and storage of carbon dioxide ($CO_2$) on a massive scale prove practical and affordable[8]. A comparison of hydrogen with other fuels is reported in table 1.2. For small scale hydrogen power generation, such as for stationary and mobile applications hydrogen storage system is necessary, and it must meet simultaneously the following six requirements decided based on economical and environmental considerations (i) high gravimetric (>9 wt%) and volumetric (>36g $H_2$/L) densities, (ii) the operation temperature approximately in the range 333–393 K, (iii) reversibility of the thermal asorption/desorption cycle, (iv) low cost, (v) low-toxicity and (vi) safety[10]. Present hydrogen storage processes are unsuitable for small scale power generation applications, therefore an onboard reforming process is proposed.

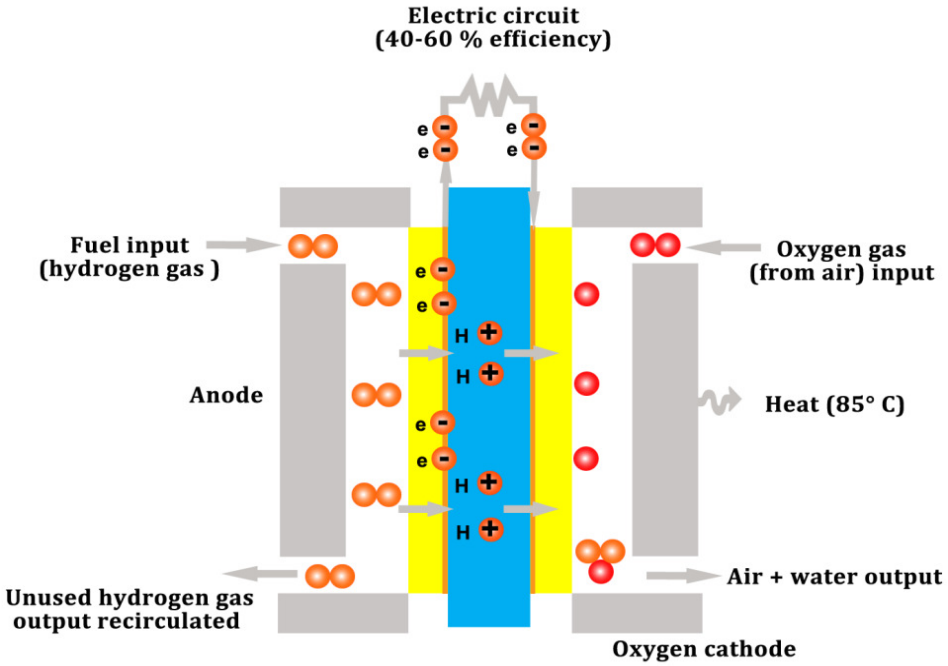


**Figure 1.1**. PEM fuel cell

**Table 1.2**. Characteristics of hydrogen as a fuel[4]

Physical properties of Hydrogen, Methane, and Gasoline

| **Properties** | **Hydrogen** | **Methane** | **Gasoline** |
|---|---|---|---|
| Molecular weight (g/mol) | 2.016 | 16.04 | ~110 |
| Mass density ($Kg/N_Am^3$) at P=1 atm=0.101 MPa, T=0°C | 0.09 | 0.72 | 720-780 (liquid) |
| Mass density of liquid $H_2$ at 20 K ($Kg/N_Am^3$) | 70.9 | - | - |
| Boiling point (K) | 20.2 | 111.6 | 310-478 |
| Higher heating value (MJ/Kg) | 142.0 | 55.5 | 47.3 |
| Lower heating value (MJ/Kg) | 120.0 | 50.0 | 44.0 |
| Flammability limits (% volume) | 4.0-75.0 | 5.3-15.0 | 1.0-7.6 |
| Detonability limits (% volume) | 18.3-59.0 | 6.3-13.5 | 1.1-3.3 |
| Diffusion velocity in air (m/s) | 2.0 | 0.51 | 0.17 |
| Buoyant velocity in air (m/s) | 1.2-9.0 | 0.8-6.0 | Nonbuoyant |
| Ignition energy (mJ) | | | |
| At stoichiometric mixture | 0.02 | 0.29 | 0.24 |
| At lower flammability limit | 10 | 20 | n.a. |
| Flame velocity in air (cm/s) | 265-325 | 37-45 | 37-43 |
| Toxicity | Nontoxic | Nontoxic | Toxic above 50 ppm |

## 1.2. Hydrogen Production

Hydrogen can be produced from a variety of processes, including electrochemical processes, thermochemical processes, photochemical processes, photocatalytic processes, or photo- electrochemical processes[11-12]. Thermochemical methods are normally used to derive hydrogen from hydrocarbons such as natural gas, coal, and biomass. Thermochemical production methods are the well established method and commercially used for the production of hydrogen which includes, steam reforming (SR), partial oxidation (POX) of hydrocarbon and gasification of biomass, coal, or wastes. The major chemical processes used today for the hydrogen production from hydrocarbons are steam reforming [Eq.(1.1)] times(SR), partial oxidation (POX) [Eq.(1.4)]times and autothermal reforming (ATR) [Eq.(1.5, 1.6)] (it is a balanced operation of SR and POX) [5, 13] followed by water gas shift reaction (WGS) and preferential oxidation of CO (PROX-CO) for the deep purification. Natural gas is

commonly used source for hydrogen production. Table 1.3 report the global hydrogen production from different sources.

**Table 1.3**. Global Hydrogen production

| Origin | Amount (billions of $Nm^3$/year ) | Percent |
|---|---|---|
| Natural gas | 240 | 48 |
| Oil | 150 | 30 |
| Coal | 90 | 18 |
| Electrolysis | 20 | 4 |
| **TOTAL** | **500** | **100** |

*Source*: U.S. Department of Energy,2003
*Note*: $Nm^3$ are normal cubic meters of hydrogen

### 1.2.1. Steam Reforming (SR)

Steam reforming is a well established reaction in the chemical industry for the production of synthesis gas for several decades since its first development in 1926[14-15]. About half of the world hydrogen production is based on steam reforming. Steam reforming is an endothermic reaction which is favorable at higher temperatures. Steam reforming process involves reacting hydrocarbon source with steam at 750-850°C to produce a synthesis gas (syngas), a mixture of hydrogen ($H_2$) and carbon monoxide (CO).

$$CH_4 + H_2O \rightleftharpoons CO + 3H_2 \qquad (H_2/CO = 3;\ \Delta H = 206.3\ kJ/mol) \qquad (1.1)$$

Industrially steam reforming is carried out at high temperature (>750°C) and pressure (>2Mpa), over a nickel – alumina catalyst with steam to carbon (S:C) ratio adjusted above to stoichiometric ratio. Methane is normally used as the hydrogen source due to its greater availability[16-18]. For methane, steam to carbon ratio is 2.5 – 3 are commonly used to reduce the coke formation during the process. Alkali metals such as K and alkaline earth metals such as Mg and Ca are frequently used to improve catalyst stability, which helps the gasification of coke formed during the reaction [19-20]. The presence of $CeO_2$ in the catalyst combination found to be effective for improving the catalytic activity and coke gasification through its high oxygen storage capacity[20]. Noble metal based catalysts such as Rh, Ru supported $Al_2O_3$ or MgO are highly active

and stable for this reaction but high cost of these materials reduces its application in industrial processes.

**Scheme 1.1**. Reactions involved in the steam reforming of methane[21]

$$CH_4 + H_2O \rightleftharpoons CO + 3H_2 \quad (1)$$

$$CH_4 \rightleftharpoons C + 2H_2 \quad (2)$$

$$C + H_2O \rightleftharpoons CO + H_2 \quad (3)$$

$$CO + H_2O \rightleftharpoons CO_2 + 3H_2 \quad (4)$$

$$2CO \rightleftharpoons C + CO_2 \quad (5)$$

Steam reforming can applied to higher hydrocarbons, naphtha, heavy oil fractions, methanol or coal for the hydrogen production.

$$C_nH_m + n\,H_2O \rightleftharpoons nCO + (n+ m/2)\,H_2 \qquad (\Delta H > 0) \qquad (1.2)$$

Higher hydrocarbons are much more active than methane, but these compounds readily lead to the formation of coke which deactivates the nickel catalysts.

Hydrogen can be produced from steam reforming of alcohols, such as methanol and ethanol. Recently, steam reforming [Eq. (1.3)] of methanol has received drawing interest as hydrogen source for portable fuel cell applications [22-23].

$$CH_3OH + H_2O \rightleftharpoons CO_2 + 3H_2 \qquad \Delta H^\circ_{298} = 50\ kJ/mol \qquad (1.3)$$

Methanol has many advantages as a hydrogen source in steam reforming, the miscibility of methanol with water is a distinct advantage in terms of fuel handling system. Methanol is a synthetic fuel, it does not suffer from sulfur contamination the way that typical automotive or residential fuels do. There is no C-C bond in methanol structure it reduces the risk of coke formation[22]. Compared to hydrocarbon reforming, methanol reforming reaction is only moderate endothermic, therefore it is possible to carry out the reaction at low temperatures (200 to 400°C) with low steam-to-carbon ratio to produce a reformate with high $H_2$ concentration. On the other hand, methanol decomposition causes CO formation, a byproduct that poisons fuel cells so water gas shift reaction is necessary for further purification of hydrogen.

**Scheme 1.2**. Reactions involved in the steam reforming of methanol[21]

$$CH_3OH + H_2O \rightleftharpoons CO_2 + 3H_2 \quad (1)$$

$$CH_3OH \rightleftharpoons CO + 2H_2 \quad (2)$$

$$CO + H_2O \rightleftharpoons CO_2 + H_2 \quad (3)$$

$$2CO \rightleftharpoons C + CO_2 \quad (4)$$

$$C + H_2O \rightleftharpoons CO + H_2 \quad (5)$$

Copper based catalysts are commercially used for methanol steam reforming. Copper is in combination with promoters ZnO and $Al_2O_3$ are used to enhance the activity of the catalyst. Pyrophoric nature of this catalyst makes them unsuitable for mobile and stationary applications. Recently developed Pd-supported catalysts are found to be highly active for methanol reforming and high selectivity towards $H_2$ formation [24].

### 1.2.2. Partial Oxidation (POX)

Partial oxidation, an exothermic non-catalytic reaction used for the production of syngas. In partial oxidation the hydrocarbon feed reacts with air or pure oxygen at

$$CH_4 + ½\ O_2 \rightleftharpoons CO + 2H_2\ (H_2/CO = 2;\ \Delta H^\circ_{298} = -35.6\ kJ/mol) \quad (1.4)$$

~1300°C and 30-100 atm [Eq.(1.4)][18]. One key advantage of partial oxidation is that it can be applied to all hydrocarbon feeds without the use of a catalyst. Commercially non-catalytic partial oxidation process in presence hydrocarbon feed with oxygen occurs at flame temperatures between 1300 and 1500°C to ensure the complete conversion and reduce the carbon formation[25].

Catalyst can be used to reduce the reaction temperature of partial oxidation. Ni or Rh based catalyst are used for the partial oxidation of methane[26-27], it is observed that Ni based catalysts have strong tendency to coke, which reduce the activity[25]. The reaction over precious metal catalysts at high temperature (~750°C) and short residence time (0.1 s) results above 90% methane conversion and 95-99% selectivity [17, 28-29]. Recently an economic approach made to maximize the hydrogen yield by combined partial oxidation reaction of methane and water gas shift reaction resulted a hydrogen production of 2.9 mol $H_2$ per mole of $CH_4$ reacted[17, 30]. Compared to steam reforming of methane, partial oxidation has several advantages: its greater selectivity to

synthesis gas production, its exothermic nature, and more desirable $CO/H_2$ ratio of the product are making this a suitable method for the production of hydrogen[29].

### 1.2.3. Autothermal Reforming (ATR)

An alternative approach for the production of syngas is autothermal reforming, a combination of partial oxidation (POX) and steam reforming (SR) process was first developed in the late 1970s by *Haldor Topsoe* [14, 31]. It is the most promising reforming technology for fuel cell applications because of its adiabatic design permitting a compact smaller reactor. In autothermal reforming the fuel is mixed with steam and sub-stoichiometric amount of oxygen or air [Eq.(1.5)(1.6)].

$$CH_4 + 3/2\ O_2 \rightleftharpoons CO + 2H_2\ (\Delta H^\circ_{298} = -519\ kJ/mol) \qquad (1.5)$$

$$CH_4 + H_2O \rightleftharpoons CO + 3H_2\ (\Delta H^\circ_{298} = 206\ kJ/mol) \qquad (1.6)$$

This reaction can be carried out in a single reactor or in separate reactors that are in good thermal contact. The autothermal reforming consists of two zones; the thermal zone and the catalytic zone. In thermal zone the partial combustion occurs and the heat generated is supplied to the catalytic zone where the endothermic steam reforming occurs[18].

The catalyst compositions used for autothermal reforming process is Ni promoted by Pt supported on $Al_2O_3$ [32-34]. Nickel catalysts exhibit high activity in steam reforming in the absence of oxygen, but in autothermal reforming it loses its reforming activity by the oxidation of nickel by the presence of oxygen in the feed. Surface modification with Pt increases the reduction rate and inhibit the Ni oxidation near the bed inlet, which favor the reforming reaction as well as the combustion reaction[32]. A detailed report of the advantages and disadvantages of steam reforming, partial oxidation, and autothermal reforming are reported in table 1. 4.

**Table 1.4**. Advantages and disadvantages of reforming technologies [25, 35]

| Technology | Advantages | Disadvantages |
|---|---|---|
| Steam reforming | Most extensive industrial experience<br>Oxygen not required<br>Lowest process temperature<br>Best $H_2$/CO ratio for $H_2$ production | Highest air emissions |
| Autothermal reforming | Lower process temperature than POX<br>Low methane slip | Limited commercial experience<br>Requires air or oxygen |
| Partial oxidation | Decreased desulfurization requirement<br>No catalyst required<br>Low methane slip | Low $H_2$/CO ratio<br>Very high processing temperatures<br>Soot formation/handling adds process complexity |

All the methods mentioned above are efficient for hydrogen production, but the production of carbon monoxide as a byproduct together with hydrogen are not suitable for many of the industrial process. Therefore, further purification processes like water gas shift and preferential oxidation of CO are necessary for the reducing the CO concentrations to ppm levels for its application in fuel cells.

## 1.3. Water Gas Shift Reaction (WGS)

"Water gas", a mixture of hydrogen and carbon monoxide is of particular importance in many industrial and petrochemical processes. Water gas is manufactured by the conversion of carbonaceous materials with steam [Eq.(1.1)], or oxygen [Eq.(1.4)]. Water gas shift (WGS) reaction [Eq.(1.7)] is a reversible exothermic chemical reaction in which carbon monoxide (CO) and water vapor ($H_2O$) reacts over

$$CO\ (g) + H_2O\ (g) \rightleftharpoons CO_2\ (g) + H_2\ (g) \qquad (\Delta H = -\ 41.1\ kJ/mol) \qquad (1.7)$$

a catalyst to form carbon dioxide ($CO_2$) and hydrogen ($H_2$). This reaction was discovered by *Italian* physicist ***Felice Fontana*** in *1780*.

It is a historically and industrially important chemical reaction. In industry this reaction is used together with steam reforming [Eq.(1)] of methane or other hydrocarbons to reduce carbon monoxide (CO) from the reformate gases and to produce additional hydrogen. Most of the hydrogen today is produced by steam reforming and

partial oxidation of hydrocarbons. However, these processes produces carbon monoxide as a side product together with hydrogen are not suitable for many of the industrial applications. For instance, purity of hydrogen is very important in ammonia production, a high level of carbon monoxide deactivates the synthesis catalyst [36-38]. In Industrial hydrogen plant (Fig) water gas shift reaction (WGS) is carried out in series of two adiabatic stages, high temperature(HTS) shift and low temperature(LTS) shift to reduce the CO concentration in the reformate stream. A schematic representation of the industrial hydrogen production plant is shown in figure 1.2.

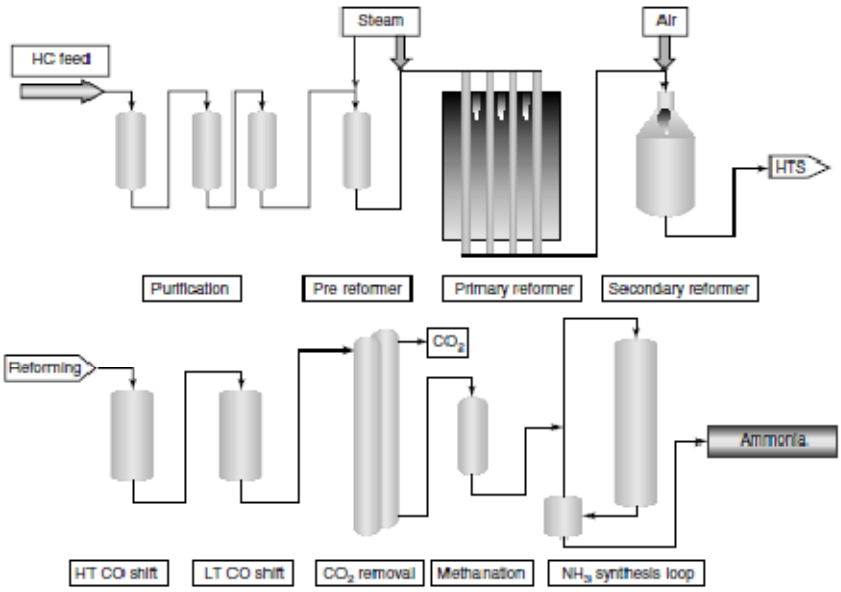


**Figure 1.2.** Schematic representation of an industrial hydrogen generation for ammonia synthesis[39]

### 1.3.1. Thermodynamics

Water gas shift (WGS) is a reversible exothermic (ΔH = - 41.1 kJ/mol) and equilibrium controlled chemical reaction [Eq.(1.7)]. The equilibrium constant $K_p$ for the water gas shift reaction is expressed by Eq. (1.8).[36]

$$K_p = \exp [(4577.8/ T) - 4.33] \quad (1.8)$$

Where T is in °K.

From the above equation it is clear that the equilibrium constant $K_p$ decreases as the temperature increases, a detailed report of the *WGS* equilibrium constants at various

temperatures are in table 1.5. To obtain higher CO conversion, it is desirable to perform the *WGS* at low temperatures [36, 40]. Concentration of water has a significant effect on the equilibrium CO concentration. The effects of S/G ratios (0.25-0.75) at various temperatures on the equilibrium CO concentrations are reported in figure 1.3 (a) and (b) for HTS and LTS, respectively. An increase of S/G ratio from 0.25 (20% $H_2O$) to 0.75 (42.9% $H_2O$) increases the equilibrium temperature to 100°C for maintaining 1% CO. This shift of equilibrium temperature by S/G ratio is useful to achieve a significant reduction of the reactor size and more favorable kinetics at higher temperature [38-39].

**Table 1.5**. WGS equilibrium constants at various temperatures[39]

| Temperature (°C) | $K_p$ | Temperature (°C) | $K_p$ |
|---|---|---|---|
| *93.3* | *4523* | *426.7* | *9.030* |
| *148.9* | *783.6* | *482.2* | *5.610* |
| *204.4* | *206.8* | *537.8* | *3.749* |
| *260.0* | *72.75* | *593.3* | *2.653* |
| *315.6* | *31.44* | *648.9* | *1.966* |
| *371.1* | *15.89* | *704.4* | *1.515* |

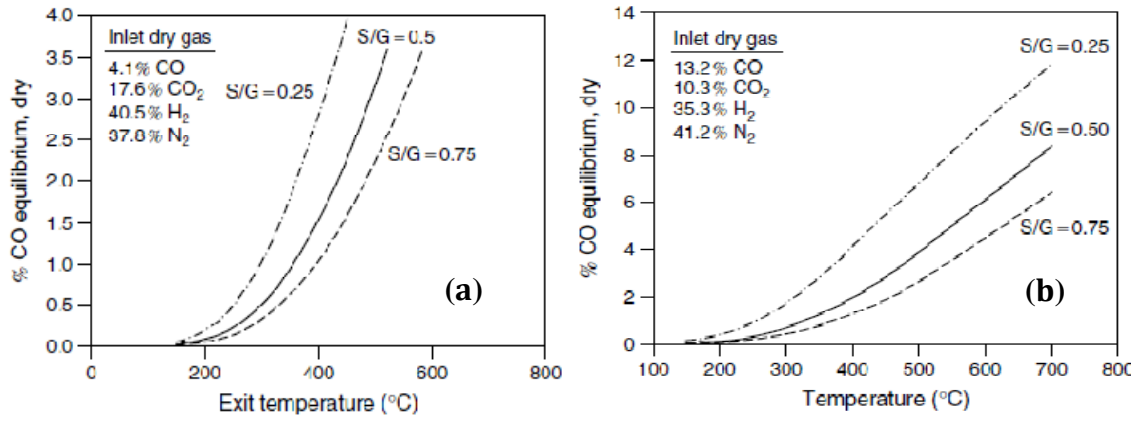


**Figure 1.3**. Effects of S/G ratios at various temperatures on HTS (a) and LTS (b) equilibrium CO concentrations: gas from autothermal reformer [38-39]

The syngas production method can also affect the WGS equilibrium. Hydrogen concentration is lower in autothermal reforming compared to steam reforming process. Hydrogen concentration in the gas stream affect the equilibrium CO conversion, lower

$H_2$ concentration from autothermal reformer improves the equilibrium CO conversion, whereas high $H_2$ concentration from steam reformer lowers the WGS reaction equilibrium conversion. Effect of $H_2$ concentration on the equilibrium CO conversion from ATR and SMR at constant CO and $CO_2$ concentrations are reported in figure 1.4 (a) and (b).

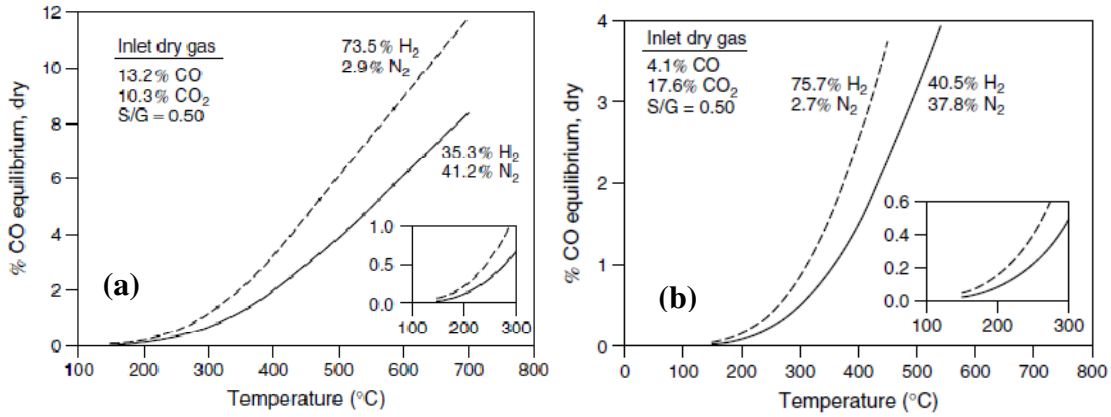


**Figure 1.4**. Effect of $H_2$ concentration on CO equilibrium of HTS (a) and LTS (b): Autothermal vs steam methane reformer (SMR)[38-39].

It is clear from the Figure that increase of $H_2$ concentration from 35% to 74% increases the CO equilibrium concentration. If we compare the equilibrium CO concentration for steam reforming and autothermal reforming with the hydrogen concentration, it is not significant as S/G ratio, but considerable when trying to maximize the efficiency and minimize volume of the WGS reactor.

**Table 1.6.** Effect of pressure on equilibrium CO concentrations (inlet dry gas: 13.2 % CO, 10.3% $CO_2$, 35.3% $H_2$, 41.2% $N_2$, S/G =0.5)[39]

| Temperature (°C) | *P*= 3 atm (% CO) | *P*= 30 atm (% CO) | *P*= 300 atm (% CO) |
|---|---|---|---|
| *200* | *0.12* | *0.12* | *0.07* |
| *300* | *0.68* | *0.65* | *0.48* |
| *400* | *1.98* | *1.94* | *1.61* |
| *500* | *3.93* | *3.88* | *3.46* |
| *600* | *6.15* | *6.10* | *5.68* |
| *700* | *8.38* | *8.34* | *7.95* |

The equilibrium CO concentration is not affected, significantly, by changes in total pressure. The effect of pressure on equilibrium CO concentrations is reported in table 1.6. No significant change observed by increasing pressure from 3 to 30 atm, however at 300 atm slight differences observed in the equilibrium CO concentration, but it is not practical to operate at a higher pressure to take the advantages of slight increase in the equilibrium CO conversion.

### 1.3.2. High- Temperature Shift (HTS)

High temperature shift reactor play a major role in reducing the CO concentration. Iron oxide-based catalysts are commercially used in HTS convertors for last few decades. The advantages of high temperature catalysts (Fe/Cr oxides) are low cost, long life and its reasonable sulphur resistance has been recognized for many years. Iron based catalyst usually contain about 8-12 wt. % of $Cr_2O_3$ and it forms a solid solution of $Fe_3O_4$-$Cr_2O_3$ spinel type. The specific activity and activation energy of the iron-based catalyst are same with or without $Cr_2O_3$, but the addition of $Cr_2O_3$ increases the stability of the catalyst and prevent the high temperature sintering and loss of surface area, there by increases the activity of the catalyst [36, 41]. The BET surface area of commercial Fe-Cr catalysts amount to 30-80 $m^2$ $g^{-1}$, it depends on the $Cr_2O_3$ content and calcination temperature [40, 42]. To improve the selectivity of the Fe HTS catalysts with respect to methane formation, sulfur resistance and mechanical strength, MgO and ZnO are sometimes present in the catalysts in addition to $Cr_2O_3$[36, 40]. The low activity of the Fe-Cr catalysts causes high reaction temperature and large reactor volume both are unsuitable for the stationary and mobile applications. During the last few decades efforts has been made to develop an improved HTS catalysts; (i) by replacing, at least partially Fe by more active elements (like noble metals) and (ii) replacing Cr, partially or completely by non-toxic elements like Cu, Ca, Ce, Zr, La etc [43-49]. Addition of small amounts of precious metals increases the activity of the HTS catalyst, among the precious metal promoters Rh was found to be the most active promoter for HTS reaction. It is found that the Rhodium promotion increases the rates of reduction/oxidation steps. Promotion of Fe-Cr catalysts with Ag, Cu, Ba, Pb and Hg were investigated for HTS reaction and the activity of the catalyst found to be Hg > Ag ~ Ba > Cu > Pb > unpromoted Fe-Cr > B. Ag and Ba promoted catalysts are promising

among the series, a 10-15% increase in CO conversion observed over these catalysts [43]. It was found that the addition of promoters decreases the activation energy of the reaction, CO adsorption is an important factor controlling the relative catalytic activity of the samples in the WGS reaction [38].

Due to the toxic nature of the $Cr^{6+}$ in commercial Fe-Cr catalysts, efforts has been made to replace Cr from Fe catalysts or to develop combinations without chromium[50-52]. Fe-Ca, Fe-Ce, Fe-Zr, Fe-Mg and Fe-Zn combinations were investigated for HTS reaction and found that these systems are not as active as the commercial Fe-Cr catalysts [50]. Catalysts combinations Co-Mn were found to be more active and sulfur resistant than commercial catalyst, but methane formation was observed over this catalyst is a drawback [51]. Pure oxides such as ZnO, MgO, $SnO_2$, $Al_2O_3$, $TiO_2$, $SiO_2$ and Na-mordenite were investigated for HTS reaction and found that these systems are less active compared to commercial Fe-Cr catalyst[50].

### 1.3.3. Low- Temperature Shift (LTS)

Up to the late 1950s the industrial ammonia synthesis plant employed with Fe-Cr oxide catalyst in the high temperature shift as well as in the second stage converter at low temperatures. Limited activity of the iron based catalysts in lower temperature range motivated further investigations to develop an active catalyst combination for the lower temperature shift reaction [38-39]. Unsupported metallic copper or copper supported on $Al_2O_3$, $SiO_2$, MgO, and $Cr_2O_3$ were investigated as a low temperature catalysts. But in 1960s a more active combination of CuO- ZnO or $CuO/ZnO/Al_2O_3$ catalyst developed for the low temperature shift (LTS) reaction. This catalyst typically composed of 32-33 % CuO, 34-53 % ZnO, 15-33 % $Al_2O_3$ [53-54]. The active species for the reaction is copper metal, ZnO provides the structural support and $Al_2O_3$ helps for the dispersion. It is extensively used in the industry in low temperature shift reactor to reduce the CO concentrations to about 0.3%.

The Cu-Zn catalyst is active in the low temperature WGS reaction, however its stringent activation procedure before and after reaction and poor thermal stability above 300°C are the drawbacks of the catalyst, which reduces its use in stationary and mobile power generation applications. It is necessary to develop a catalyst combination besides

higher activity and improved stability but also the combination which must possess other important characteristics compared to the traditional catalyst: non-pyrophoric, stability towards condensation and poisoning, fast startup and no requirement for exceptional pretreatments [55-56].

Many efforts have been made to develop catalyst combinations active and stable for fuel processing applications. Last few years many catalysts combinations are investigated for the low temperature WGS reaction, which includes noble metal based catalysts and base metal oxide combinations with partially reducible metal oxide supports. The noble metal catalyst combinations mainly includes Pt, Rh, Ru, Au and Pd deposited on partially reducible oxides such as ceria, zirconia, titania, iron oxide, and mixed oxides of ceria[57-69]. These combinations maintain the crucial requirement of the fuel processor catalysts by its quite active performance in the 250-400°C range, non pre-reduction requirement and non-pyrophoric nature. Among the noble metal based catalysts investigated, gold catalysts showed promising activity at low temperatures compared to Pt based catalysts; Pt- based catalysts are less active below 250°C in WGS reaction. Activity of the gold catalysts at low temperature is explained due to the synergism of gold-metal oxide. Activity of the gold catalyst is depending on many factors: preparation conditions, dispersion, gold particle size, metal-support interaction[70]. Improvement in the performance of the gold catalyst is observed by the addition of another metal (like Pt) in the catalyst combination. The bimetallic Au-Pt-Ce catalyst exhibit much higher activity compared to Au-ceria at the same temperature [71]. The superior activity of the bimetallic Au-Pt-ceria catalyst in WGS reaction was strongly correlated with the ease of surface reducibility compared to Au-ceria. Promising activity of the precious metals catalysts are useful for its application in fuel processing, however high cost and less availability is a drawbacks of these catalysts.

Base metal combinations with partially reducible metal oxides are investigated for WGS reaction. These include Cu-$CeO_2$ [69, 72], Ag-$TiO_2$, Cu-$TiO_2$ [60], Cu-$ZrO_2$ [73], Cu-$Fe_2O_3$. Among base metal combinations Cu-$CeO_2$ catalysts are promising alternative for the traditional low temperature WGS catalyst. Compared to other low temperature WGS catalyst, Cu-Ce catalysts exhibit high activity, and thermal stability. Improved thermal stability observed in ceria by doping with La [74-75]. Activity of the Cu-Ce catalysts are comparable with the ceria- supported noble metal catalysts,

however, less sulfur resistant is a drawback. Low cost, better thermal stability and ease of availability makes it more attractive for fuel processing applications.

## 1.4. Low-temperature removal of carbon monoxide

Carbon monoxide is a highly flammable gas, its combustion together with air can occur between 12 and 75 vol%, but its homogeneous combustion at much lower concentrations (50 - 50 000 ppm) is virtually impossible. To achieve the elimination of CO particularly at the lower concentration range, it is necessary to catalyze its oxidation. There for catalytic oxidation is an efficient way to convert lower amount of CO to $CO_2$ [76]. CO oxidation (CO-OX) at lower temperature is important for several technological applications, which include automotive exhaust abatement, CO sensors, closed-cycle $CO_2$ pulsed. It is also involved in the CO removal from hydrogen streams by preferential oxidation (CO-PROX), a process which would make feasible the required deep clean-up of the hydrogen feeds to proton exchange membrane fuel cells for mobile applications.

The polymer electrolyte membrane fuel cell (PEM-FC) is the most promising technology for generating electricity at low temperature (~80-120°C) together with hydrogen. It offers efficient and clean energy production for mobile and stationary applications. High purity hydrogen is one requirement for the efficient functioning of the PEM fuel cells. The fuel cells anodes are based on precious metals and are highly sensitive to deactivation by carbon monoxide adsorption at low temperatures[77-78]. The reformate coming out from the fuel processor normally contains ~75 vol% $H_2$, ~ 24 vol% $CO_2$ and ~ 1-3 vol% CO. Using high $H_2O$/CO ratio the CO reduction below 100 ppm cannot be achieved using water gas shift reaction, 1 vol% CO is usually contained in the hydrogen stream [79]. The amount of CO present in the hydrogen stream strongly poisons the Pt or Pt-Ru anodes, thereby blocking the active sites where the dissociation/oxidation of $H_2$ can take place and deteriorating cell performance.

The CO concentration at the WGS reactors exit is too high and not suitable for PEM fuel cells. Final purification is necessary for its use in PEM fuel cells efficient functioning. For platinum anode acceptable CO concentration is below 10 ppm and below 100 ppm for CO-tolerant alloy anodes [80-81]. Final purification to less than 10 ppm is achieved by several processes: (i) Pressure Swing Adsorption (PSA), (ii)

methanation of residual CO, (iii) membrane separation or (iv) preferential CO oxidation (PROX). The processes (i) and (ii) are commonly used in mass production of hydrogen and the last two processes are more suitable for small-sized stationary and mobile hydrogen production units[82]. Among this Preferential oxidation of CO is the low cost method to reduce CO to the desired level.

### 1.4.1. Low temperature oxidation of carbon monoxide (LT-CO)

Catalytic oxidation of CO may be the most extensively studied reaction in history of heterogeneous catalysis. The catalytic oxidation of CO at ambient temperatures is important in the control of environmental pollution, particularly in the cleanup of vehicle emission. It has application in mine rescue devices, CO sensors, closed-cycle $CO_2$ pulsed lasers [83-85]. CO oxidation is often used as a probe reaction for the oxide surface characterization. Supported noble metal catalysts are typically used to catalyze the reaction. Precious metals used for the reaction are not suitable to oxidize CO at lower temperature and low $O_2$/CO ratios due to the competition of adsorption of $O_2$ and CO for the same site. An efficient catalyst must accommodate CO chemisorptions and simultaneous dissociative adsorption of $O_2$ at low temperature, for this purpose composite materials with different components are used. This includes noble metal supported reducible oxides, and base metal oxides catalysts are used for the oxidation of CO at low temperatures.

#### 1.4.1.1. Noble metal-reducible oxide catalysts

Noble metal- reducible oxide combinations are intensively studied material for carbon monoxide oxidation reaction. The material combinations studied for this reaction includes Pt/$SnO_2$[86-87], Pt/$MnO_x$, Pt/$CoO_x$ [88], Pt/$CeO_2$, Pd/$SnO_2$ [89], Pd/$MnO_x$ [90], Pd/$CeO_2$, Pd/$ZrO_2$ [91], Rh/$TiO_2$, Au/$MnO_x$ [92-94], Au/$CeO_2$, Au/$Fe_2O_3$ [95-97], Au/$Co_3O_4$ [96, 98], Au/$TiO_2$ [99-100], etc. The activity of these catalysts at low temperatures are claimed to be due to the strong metal- support interaction (SMSI). It is proposed that the reaction is proceeds through the adsorption of CO on the metal surface and oxygen is provided by the support. High price and less availability of precious metals motivate further research to find a suitable base metal oxide catalyst.

However, gold supported reducible metal oxides are promising catalyst for the low temperature CO oxidation reaction.

### 1.4.1.2. Gold- based catalysts

Gold is supposed to be an inactive material for long period of time, but the research conducted by *Haruta* and co-workers have shown that gold nano-particles can catalyze CO oxidation at room temperature or even below, if it highly dispersed on reducible oxide support such as $TiO_2$ [96, 99-100], $Fe_2O_3$ [95-97], $Co_3O_4$ [96, 98], $ZrO_2$[101], $MnO_x$ [92-94], NiO[98]and $CeO_2$ [102-103]or mixed oxides: $CeO_2$-$ZrO_2$ [104], $CeO_2$-$TiO_2$, Fe-$TiO_2$[105] Zn, Fe/$CeO_2$-$Al_2O_3$[106], $MnO_x$-$CeO_2$ [107-108], etc. Ordered mesoporous silicas such as SBA-15, MCM-48, MCM-41[109-111] and metal oxides doped mesoporous silicas also served as a support for gold [112-114]. High CO oxidation activity observed over these catalysts due to the high dispersion of gold nano-particle on the supports. Gold deposited SBA-15 showed CO oxidation activity only when the material under goes subsequent $H_2$/He treatment at higher temperatures. The higher temperature pretreatment generates E' centers which is responsible for the formation of $O_2^-$ on silica surface upon exposure of oxygen[111, 115]. Activity of gold catalysts depends on many factors: preparation method, $p^H$, particle size, types of support used for the deposition[116]. Mechanism of CO oxidation over gold-based catalysts is not clear. Schematic representation of the proposed reaction mechanism of CO oxidation over Au/$TiO_2$ catalysts are reported in scheme 1.3.

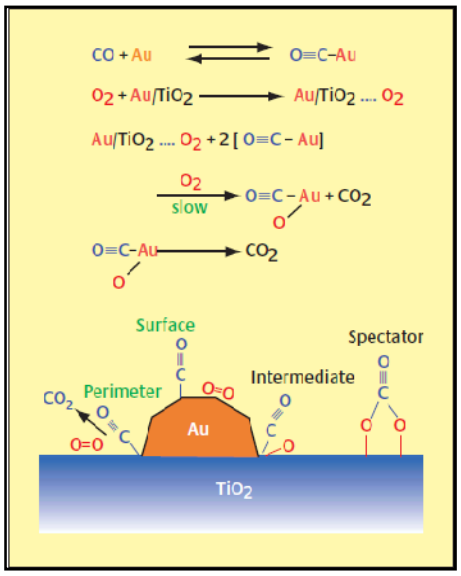


**Scheme 1.3**. Reaction mechanism of CO oxidation over Au/$TiO_2$ [117]

#### 1.4.1.3. Base- metal oxide catalysts

Base metal oxides have got intense research attention as catalyst for CO oxidation before noble metals proved their dominant activity in automotive exhaust gas catalysis. Compared to noble metal catalysts, their undesirable behavior in cycled transient conditions and high deactivation in presence of sulfur and water were the main reason to its withdrawal from catalytic converters. Hopcalite (combination of $CuO/MnO_2$) was the active base metal oxide catalyst for CO oxidation at ambient temperatures. Activity of the material at low temperature promotes its application in life-rescue equipment, however deactivation in presence of moisture is a major drawback of this catalyst [76, 118]. It is necessary to develop a catalyst which is active in the low temperature range with good stability and moisture resistance is of recent research interest. Several combinations of base metal oxides were investigated for the low temperature CO oxidation reaction, those are classified as supported and unsupported metal oxides [76].

##### 1.4.1.3.1. Unsupported metal oxide catalysts

Cobalt oxide and copper oxide catalysts showed interesting activity for CO oxidation reaction. Cobalt oxide a cubic spinel type transition metal oxide composed of $Co^{2+}$ and $Co^{3+}$ ions in the tetrahedral and octahedral sites, respectively. This material intensively studied for CO oxidation and found that the materials intrinsic activity is very close to that of noble metals. The co-existence $Co^{2+}$- $Co^{3+}$ ion pairs seems to be essential for the catalytic activity of the material. Steam and pretreatment conditions strongly affect the activity of the catalyst in CO oxidation. Presence of steam in the reaction mixture dramatically inhibits the CO oxidation activity [119].Catalysts pretreatment in reducing conditions (CO or $H_2$ in $N_2$) make drastic change in the $Co^{2+}/Co^{3+}$ balance this makes negative effect on CO oxidation activity of the catalyst [120]. Recent study suggest that the morphological control of $Co_3O_4$ is very rewarding, cobalt oxide nano-rod catalyst exhibit high activity and stability for CO oxidation in presence of $H_2O$ and $CO_2$ at 200-400°C [121].

Unlike cobalt oxide, copper oxides are more rarely used in CO oxidation. Copper oxides are not very stable, its oxidation state varies during the course of the reaction. Many efforts have been made to identify the active sites for the CO oxidation

reaction. Excellent CO oxidation activity at room temperatures was observed over $Cu_2O$ catalyst by Garner et al but Jermnigan and Somorjai observed superior CO oxidation activity of metallic copper at 275°C and the activation energies were 37, 70, and 57 kJ $mol^{-1}$ for $Cu^0$, $Cu_2O$, and CuO[122]. Huang and Tsai observed superior activity of $Cu_2O$ surface for CO oxidation in oxygen rich and oxygen lean conditions at 140 and 205°C[123]. Langmuir- Hinshelwood mechanism proposed for CO oxidation over Cu and CuO, whereas Mars-van Krevelan mechanism observed over $Cu_2O$ [122].

#### 1.4.1.3.2. Supported metal oxide catalysts

Huge numbers of supported metal oxides are investigated for CO oxidation reaction, most studied combinations are supported copper oxide based catalyts such as $CuO/Al_2O_3$, $CuO/CeO_2$, $CuO/TiO_2$, CuO/ZnO, $CuO/ZrO_2$ and many other mixed oxides like $CeZrO_x$, $CeSnO_x$, $CeTiO_x$ [76]. Supported copper oxides combinations are of particular interest due to its promising activity, $SO_2$ tolerance compared to other combinations. Ceria based materials are of great interest in the field of catalysis, the suitability of ceria is mainly due to its high oxygen storage capacity [124]. Ceria supported or mixed oxides of ceria (like $CeZrO_x$) supported copper oxides are intensively studied for CO oxidation reaction. Pure ceria shows CO oxidation activity at 300°C, but a very small amount of copper promotes its activity at lower temperatures [125]. Liu and Flytzani- Stephanopoulos first reported the high activity of Cu-$CeO_2$ catalysts for CO oxidation reaction[126-127] and they concluded that the high activity is related to the special Cu-Ce-O interaction and not due to the dispersion of copper. Some other approaches proposed that the high CO oxidation activities of Cu-$CeO_2$ catalyst are due to the finely dispersed CuO surface species. For this reason they prepared high surface area $CuCeO_2$ catalysts by different preparation methods [128-131]. Improvement in the oxygen storage capacity and thermal stability of ceria was observed by the introduction of other metal ions in to the ceria lattice [132-133]. Copper promoted mixed oxides of ceria are more active for CO oxidation compared to Cu-$CeO_2$. Most investigated combinations are $CuO/CeZrO_x$, $CuO/CeSnO_x$, $CuO/CeTiO_x$ [134-136]. These mixed oxides support helps to increase the dispersion and stability of copper oxides.

## 1.5. Preferential oxidation of carbon monoxide (PROX-CO)

Preferential oxidation of CO is the most studied and most effective method for the removal of traces of the CO from the reformate stream. Carbon monoxide in the exit of the water gas shift reactor is selectively oxidized in the PROX reactor over oxidation catalysts with externally supplied oxygen. In a PROX system the following three reactions can occur. A schematic representation of the fuel processor for PEMFC is reported in Figure 1.5.

$$CO\,(g) + 1/2\,O_2\,(g) \longrightarrow CO_2\,(g) \quad \Delta H = -282.98\ J/mol \tag{1.9}$$

$$H_2\,(g) + 1/2\,O_2\,(g) \longrightarrow H_2O\,(g) \quad \Delta H = -241.82\ J/mol \tag{1.10}$$

$$CO\,(g) + 3\,H_2\,(g) \longrightarrow CH_4\,(g) + H_2O\,(g)\ \Delta H = -205.81\ J/mol \tag{1.11}$$

The PROX catalysts need to be active and selective between the outlet temperature of the WGS reactor and the inlet temperature of the fuel cell (~80°C). An efficient catalyst must selectively oxidize 0.5 - 1 vol% CO from the reformate to levels applicable to a fuel cell. Hydrogen is the major component in the reformate, its oxidation reduces the overall fuel efficiency and the water formation (by hydrogen oxidation) affect the catalytic activity of the catalysts. Therefore, high CO oxidation activity and low hydrogen oxidation activities are the essential requirement for PROX catalysts [55, 137-138].

The performance of the PROX catalysts is affected by the $O_2$/CO ratio, reactor temperature, and space velocity. Higher $O_2$/CO ratio promote the CO and $H_2$ oxidation resulting heat generation due to its exothermic nature, which promote the reverse water gas shift (RWGS) and methanation of CO and $CO_2$ reaction [Eq.(1.11)] consumes large amount of hydrogen compared with preferential oxidation of CO (PROX) [79].

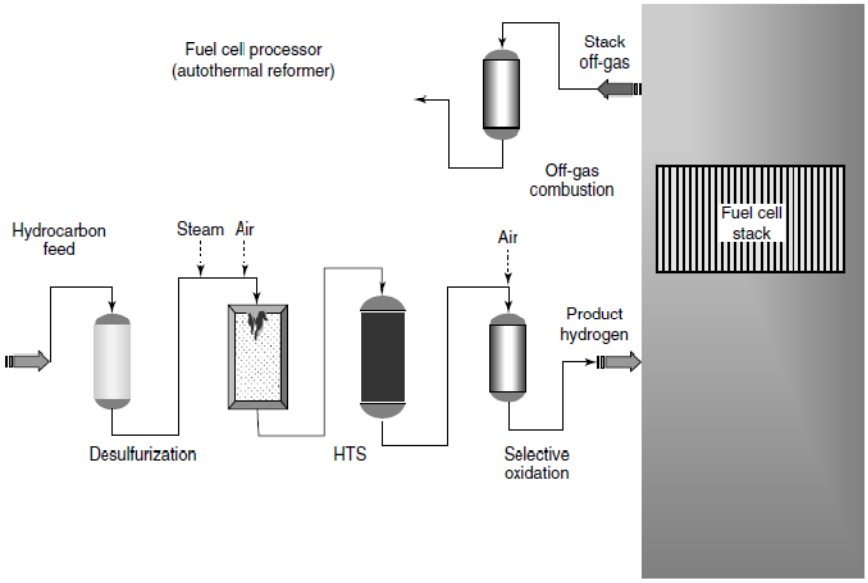


**Figure 1.5**. Schematic representation of the fuel processor for PEMFC

### 1.5.1. Catalysts for CO-PROX

Many catalytic systems are reported to be active for the preferential oxidation of CO (PROX). They can be grouped into three classes: supported noble metal catalysts (Pt, Pd, Ir, Ru or Rh), nano-gold catalysts, and base metal oxide catalysts.

#### 1.5.1.1. Supported noble metal catalysts

Commercially used catalysts for selective oxidation of CO are alumina supported noble metal catalysts (alumina supported Pt, Ru, and Rh), operating at temperatures in the 120-160°C range [139-141]. Among these metals, platinum based catalysts are the most studied system for preferential oxidation of CO. A comparative study of $\gamma$-$Al_2O_3$ supported Pt, Ru and Rh were investigated for the preferential oxidation reaction and the selectivity of the catalyst observed as ~40%, ~80%, and ~80% for Pt- $\gamma$-$Al_2O_3$, Ru/$\gamma$-$Al_2O_3$, and Rh/$\gamma$-$Al_2O_3$, respectively, at CO conversion close to 100% in presence of $H_2$[140]. Zeolite and alumina supported platinum catalysts investigated for PROX in a reaction mixture similar to the reformate gases, superior selectivity observed for Pt based catalysts compared to alumina supported Ru and Rh catalysts. Ru and Rh based catalysts showed 25% selectivity and Pt based catalysts showed selectivity between 40% and 50% for almost complete CO conversion [142-143]. Platinum catalysts supported on different zeolites are claimed to be active for

preferential oxidation (NaY zeolite, NaX zeolite, Na mordenite, KL zeolite, NaZSM-5 zeolite and Naβ zeolite)[138]. A comparative study of selective CO oxidation in $H_2$ rich fuels at 150-200°C was investigated over zeolite supported Pt catalysts (5.8-6 wt%) and alumina supported Pt catalysts, the reaction mixture consisting of 1% CO, 2% $O_2$, and balance $H_2$. The selectivity was found to decrease in the following order Pt- zeolite A > Pt- mordenite > Pt- zeolite X > Pt- alumina. The zeolite supported platinum catalysts oxidize CO much more selectively with less oxygen consumption compared to conventional Pt-$Al_2O_3$. Pt-mordenite require only 1.5 % oxygen to remove CO whereas conventional Pt-$Al_2O_3$ catalyst require 3% oxygen for the removal of CO. Pt-morenite catalyst are suggested as a promising catalyst for PROX because it had resistance to water in the feed [144].

Base metal oxides promoted platinum catalysts are active for the selective oxidation of CO. The addition of a second metal to the platinum based catalysts enhances its activity in PROX at low temperatures. Metals such as Sn [145-146], Fe[147-148], Ce [149-150], Mn [151-152], Co[153-154], Ni [152, 155], Nb [156], and alkali metals [157-159] were the active promoters for platinum based catalysts. Addition of these promoters provides the active oxygen for the selective CO oxidation and also the presence promoters creates a non-competitive dual site adsorption pathway enhancing the CO activity for the promoted catalyst. A dual site non- competitive mechanism over Pt-M (M= Ni or Co) are shown in scheme 1.4.

Among the commercial catalysts studied, both Ru/$Al_2O_3$ and Rh-$Al_2O_3$ are the most active catalysts for the selective CO oxidation at 100°C, their $T_{50}$ values ~70°C lower than that for Pt/γ $Al_2O_3$. The activity of the commercial catalysts in preferential oxidation of CO in $H_2$- rich gas (between 100 and 200°C) is found to be decreased in the order Ru/γ-$Al_2O_3$ > Rh/γ-$Al_2O_3$ > Pt/ γ-$Al_2O_3$ > Pd/ γ-$Al_2O_3$ [118, 140]. Rhodium supported catalysts are promising candidate for selective CO oxidation [140], Rh/MgO catalysts showed superior activity in preferential oxidation compared to Ru/γ$Al_2O_3$ and Pt/γ $Al_2O_3$. The better performance of Rh/MgO at higher temperature (250°C) in the presence of $H_2O$ and $CO_2$ may be due to its poor activity for reverse water gas shift reaction and methantion reaction compared to CO oxidation activity[160].

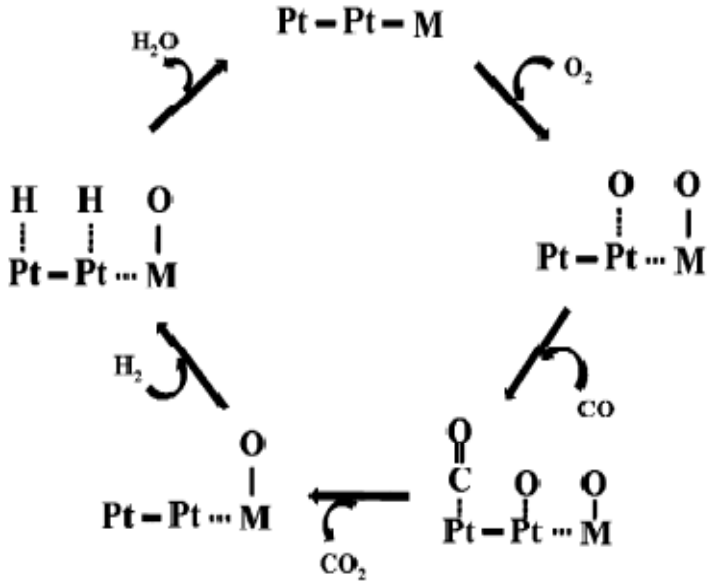


**Scheme 1.4**. Reaction scheme for the PROX over Pt-M (M= Ni or Co) catalysts [138].

The detailed mechanism of the preferential oxidation of CO over noble metals is not revealed. Due to the strong chemisorption of CO over noble metal surface compared to $H_2$ and $O_2$, hydrogen oxidation is strongly inhibited [161-162]. CO displaces the weakly chemisorbed $H_2$ and $O_2$ species from the metal surfaces and prevents the reaction. Desorption of CO happens when the temperature is high enough to desorbs some of the CO on the surface [163-164]. This indicates that the light-off behavior of the noble metal catalysts in CO-$H_2$-$O_2$ mixtures is dominated by the kinetic features characteristics of the CO-$O_2$ reaction rather than by the kinetics of $H_2$ oxidation. The hydrogen in the feed can interact with the chemisorbed CO to form a complex such as H-CO, its easier desorption from the surface may increase the CO oxidation activity significantly [140].

### 1.5.1.2. Nano - gold catalysts

Gold has a rich coordination and organo-metallic chemistry, but was considered to be catalytically inactive for a long time. The remarkable catalytic activity shown by gold depends on forming it into very small particles thereby forming a number of low-coordination surfaces atoms which chemisorb the reactant molecules strongly compared to its large particles[165]. Supported gold catalyst has been a subject of intense investigation since the report of its exceptionally high CO oxidation activity at a temperature as low as 200 K [96, 98]. Numerous investigations have been made over

Au based catalysts for CO oxidation and preferential oxidation of CO (PROX). The nature of the support and gold particle size affect the catalytic activity to different extents[166]. The suitable supports are the metal oxides which could be partially reduced, such as $TiO_2$, $Fe_2O_3$, $Co_3O_4$ and NiO [96, 98, 167-168], $MnO_x$ [169-170], $SnO_2$ and $CeO_2$ [171-172] or mixed oxides: $MnO_2$-$CeO_2$ [173], $CeO_2$-$Fe_2O_3$ [174], ZnO–$Fe_2O_3$ [175], and $CeO_2$–$TiO_2$[176], $CeO_2$-$Co_3O_4$[177]. Supported gold catalysts showed promising activity for PROX especially at lower temperatures however, the selectivity for CO oxidation over $H_2$ oxidation decreased rapidly with increasing reaction temperature. The DFT calculations showed that for PROX reaction, OH formation step is compete with the CO oxidation step and the relative rates of these two steps appear to determine the selectivity of PROX. The activation energy barrier for CO oxidation on Au (111) was calculated to be 0.18 eV and for OH formation was 0.90 eV. At higher temperatures weaker CO adsorption was observed on Au surfaces, which cause a loss in selectivity of CO oxidation [178]. Bimetallic Au-Cu catalysts showed good selectivity for CO oxidation with less $H_2$ consumption. The interaction between Cu and Au seemed to be able to modify the catalytic properties of Au active sites for CO oxidation. There is an optimal Cu content to benefit the CO oxidation, as high contents of copper lead to blocking of gold active sites [179].

Deposition-precipitation technique using NaOH or $Na_2CO_3$ [180]or urea [181] are used to prepare finely dispersed gold particle (2-3 nm) on reducible supports. Chloride ions have a crucial role in the deactivation of gold catalyst; the presence of chloride ions in the catalyst agglomerates gold particles faster at elevated temperatures thereby poisoning the active sites. Chloride ions accelerates the Au sintering and strongly deactivates the catalyst in PROX reaction, so the elimination of chloride ions from the catalysts prior to PROX reaction is mandatory[182]. The reaction mechanism of gold supported catalysts is not clear but it claimed that the reaction occurs at the metal/support interface [183]. Compared to Pt based catalysts, gold based catalyst are more active and selective in a large temperature range but deactivation due to sintering during the reaction is a drawback of this catalyst.

### 1.5.1.3. Base metal oxide catalysts

The high cost and less availability of the precious metals has encouraged the researchers around the world to develop alternative base metal oxide catalysts for preferential oxidation. It is worthy to develop a catalyst without precious metals in their combinations that is active, selective and stable during reaction is of particular interest. Transition metal oxides have a remarkable role as a catalyst or as a catalyst support for catalyzing various chemically and industrially important reactions. Preferential oxidation of CO was a subject of intense research over transition metals and transition metals promoted base metal oxides. Cobalt oxide show the best performance among the 3d transition metal oxides for PROX, its supported combinations with $CeO_2$, $ZrO_2$, $Al_2O_3$, $SiO_2$ and $TiO_2$ [184-185] were investigated for PROX, Co-Zr combination found to be most active among the series. However, CO methanation in the presence of excess hydrogen is the drawback of this catalyst. Transition metals (Co, Cu, Cr, Ni, and Zn) supported on base metal oxides with different acidic, basic and redox properties (MgO, $La_2O_3$, $SiO_2$–$Al_2O_3$, $CeO_2$, $CeO_2$-$ZrO_2$) investigated for preferential oxidation [186]. Out of them, ceria- and ceria- zirconia- supported copper catalysts showed promising activity compared to the platinum group catalysts classically used for this reaction. A comparative study of preferential oxidation of CO was carried out over Pt/$\gamma Al_2O_3$, Au/$\alpha Fe_2O_3$ and Cu-$CeO_2$ with same reaction conditions. Noble metal catalysts showed superior activity at lower temperature range but the selectivity of Cu-$CeO_2$ catalysts at 100-200°C range is higher than the selectivity of Pt or Au catalysts [187]. Copper–ceria catalysts are promising alternative catalyst to noble metal and gold based catalysts, less cost, ease of availability and remarkably higher resistance to carbon dioxide and water poisoning makes it more suitable for the preferential oxidation.

Among the mixed oxide catalysts, CuO-$CeO_2$ is intensively studied material for preferential oxidation. The catalytic properties of CuO-$CeO_2$ systems are studied in detail for PROX with effect of preparation method[188-193], copper content and calcinations temperature[194], promoters [195-198] and support [135, 199-201]. The effect of preparation method on the preferential oxidation of CO over CuO-$CeO_2$ was investigated with different preparation methods, activity of the catalyst according to the preparation method is found in the following order urea-nitrates combustion > citrate-hydrothermal > co-precipitation > impregnation[188]. Superior activity of the catalysts

prepared by unrea-nitrate combustion method is claimed to be related to the formation of well-dispersed copper oxide species in strong interaction with ceria and the absence of bulk CuO. A detailed report regarding the effect of preparation method on PROX of CO over CuO-$CeO_2$ is reported in Table 7. Amount of copper content in the CuO-$CeO_2$ catalysts increases the CO oxidation activity but the amount beyond the dispersion capacity (1.2 mmol CuO/100 $m^2$ $CeO_2$) of ceria promotes the undesirable $H_2$ oxidation (due to the formation of bulk copper on ceris surface) decreases the selectivity [202].

Calcination temperature promotes the PROX activities of the CuO-$CeO_2$ catalyst to a particular extend. Increasing calcination temperature not only decreases the surface area of the material, but also in a better interaction between CuO and $CeO_2$, which promotes the activity of the catalyst [192, 194]. Increase of calcination temperature to a particular extend favor the activity of the catalyst, beyond that CuO phase separation occurs, which results weak interaction between CuO and $CeO_2$ thereby reduces the specific reaction rate. Doping ceria with promoters such as, $ZrO_2$, $SnO_2$, $Fe_2O_3$, $TiO_2$, and $La_2O_3$ improves its oxygen storage capacity, redox properties and thermal stability. Oxygen storage capacity of $Ce_xZr_{1-x}O_2$ solid solution is three to five times larger than pure $CeO_2$ [203]. Copper promoted $Ce_{0.9}Zr_{0.1}O_2$ catalysts shows increased mobility of lattice oxygen and promote activity in selective CO oxidation compared to CuO-$CeO_2$ catalyst [204].

The enhancement of CO oxidation activity of Cu-$CeO_2$ catalysts is attributed to the “synergistic” effect [205]. It is proposed that well dispersed copper on ceria is reducible at lower temperature compared to bulk CuO. The Cu-O-Ce interface is proposed to be the active site for the preferential oxidation of CO [190]. Copper content and calcination temperature has some role in promoting the activity of the catalyst. Doping of ceria with promoters improves oxygen storage capacity, redox properties, thermal stability of the material compared to its pure form.

**Table 1.7**. Effect of catalyst preparation method for preferential oxidation of CO over $CuO\text{-}CeO_2$

| Catalyst | Preparation method | Feed composition | Temperature (K) | CO conversion (%) | Space velocity | Reference |
|---|---|---|---|---|---|---|
| 20% $CuO\text{-}CeO_2$ | Co-precipitation | 1% CO, 1% $O_2$, 13.5% $CO_2$, 50% $H_2$, 20% $H_2O$, and He balance | 438-448 | ~100 | 250 ml/min/$g_{cat}$ | [206] |
| 3% $Cu\text{-}CeO_2$ | Impregnation | 2% CO, 1% $O_2$, 70% $H_2$, and He balance | 409 | 76.2 | 1000/h | [186] |
| $Cu_{0.1}Ce_{0.9}O_{2-y}$ | Sol-gel | 1% CO, 1.25% $O_2$, and $H_2$ balance | 393 | ~80 | 1000 ml/min/ $g_{cat}$ | [207] |
| $Cu_{0.15}Ce_{0.85}$ | Urea nitrate combustion | 1% CO, 1.25% $O_2$, 15% $CO_2$, 50% $H_2$, 10% $H_2O$, and He balance | 463 | 99 | 417ml/min/ $g_{cat}$ | [188] |
| 15% $Cu\text{-}CeO_2$ | Single-step citrate | 0.03% CO, 0.03% $O_2$, 1% $H_2$, and He balance | 473 | 98 | 83,000/h | [189] |
| 5% $CuO\text{-}CeO_2$ | Urea gelation/co-precipitation | 1% CO, 1.25% $O_2$, 20% $CO_2$, 50% $H_2$, 10% $H_2O$, and He balance | 438 | 99 | 1333 ml/min/$g_{cat}$ | [190] |
| 25% $CuO\text{-}CeO_2$ | Citrate- hydrothermal | 1% CO, 1.25% $O_2$, 15% $CO_2$, 50% $H_2$, 10% $H_2O$, and He balance | 473-483 | 99 | 417 ml/min/$g_{cat}$ | [192] |
| $Cu_{0.8}Ce_{0.2}O_2$ | Microemulsion | 1% CO, 1.25% $O_2$, 50% $H_2$, and Ar balance | 353-363 | ~100 | 80,000/h | [208] |
| $Cu/CeO_2$ | Hydrothermal synthesis with cetyltrimethylammonium bromide | $CO/O_2/H_2/H_2O/CO_2$ (1/1/50/10/20) | 393 | 97.3 | 1.12 $g_{cat}$ h/mol | [193] |
| 4% Cu-CeO2 | Impregnation | 0.5% CO, 0.5% $O_2$, 50% $H_2$, and $N_2$ balance | 383 | 99.8 | 120 ml/min/$g_{cat}$ | [209] |

## 1.6. Conclusions

A detailed literature survey about the hydrogen production and purification processes is carried out in this chapter and the conclusions are as follows:

- ✓ Hydrogen is the most attractive alternative fuel to fossil fuels due to its pollution energy production with PEM fuel cells.
- ✓ Hydrogen can be produced from a variety of sources, however thermo-chemical methods are commercially well established methods.
- ✓ Steam reforming of methane is the cheapest method to produce hydrogen.
- ✓ Water gas shift reaction and preferential oxidation of CO have crucial role in purifying the hydrogen.
- ✓ Noble metal catalysts are active for these reaction, but high cost and less availability reduces its use in industrial processes.
- ✓ Compared to precious metal catalysts, copper-ceria catalysts are the promising alternative catalyst for water gas shift (WGS) reaction and preferential oxidation (PROX) reaction.
- ✓ Preparation methods, promoters, pre-treatment conditions affect the performance of the copper-ceria catalysts.
- ✓ Further research is needed to find a suitable catalyst which is active, selective, stable and cost effective for the hydrogen production and purification processes.

## 1.7. Outline of the thesis

Present PhD thesis deals with the investigation on the development of active, selective and stable base metal oxide catalyst combinations for CO oxidation and preferential oxidation of CO at low temperatures. Four base metal oxide catalytic systems were developed by hard template method using SBA-15 mesoporous silica as a hard template. Among the four base metal oxide catalytic systems developed, two of them are cobalt based catalysts and other two are ceria based catalysts. Cobalt oxide and ceria based catalysts have remarkable role in catalyzing various chemically and industrially important reactions. One of the most important properties of cobalt oxide spinel is its ability to accommodate wide range of metal cations and oxidation states into its structure. Cerium and cerium containing materials got special research interest in catalysis due to its exceptional oxygen storage capacity. In present study we developed transition metal ions doped cobalt oxide and ceria based catalyst combinations for low temperature CO oxidation and preferential oxidation of CO.

Chapter three gives the detailed report about the synthesis, characterization and catalytic activity of $Cu^{2+}$ doped cobalt oxide (CuCo-*x* systems). All the catalysts show similar activity in CO oxidation and preferential oxidation of CO till 100°C, beyond this point copper doped catalysts found to be superior compared to pure cobalt oxide. Chapter four report the synthesis and characterization of $Fe^{3+}$ doped cobalt oxide and gold deposited FeCo-*x* spinels for CO oxidation and preferential oxidation of CO. Gold based catalyst was superior in CO oxidation reaction compared to FeCo-*x* spinels, but in the presence of hydrogen gold based catalyst completely lost its CO oxidation activity. Superior activity of the FeCo-*x* spinels observed in preferential oxidation of CO compared to pure cobalt oxide.

Chapter five report the details about the synthesis, characterization and catalytic activity of copper-ceria mixed oxide catalysts with 17 to 76 mol% of copper deposited on the ceria. All copper-ceria catalysts show similar activity in CO oxidation. In preferential oxidation of CO minor difference in activity observed over $Cu_{76}Ce$ catalyst compared to $Cu_{17}Ce$ and $Cu_{43}Ce$. Chapter six report the details about the synthesis, characterization and catalytic activity of a tri-component copper-ceria-iron oxide and gold-ceria-iron oxide catalysts. Ceria-iron oxide support were synthesized by hard

template method. Copper deposition on the support carried out using chelating-impregnation (CI) and incipient wetness impregnation (IWI) method. Gold deposition carried out using deposition-precipitation method. No significant differences observed in CO oxidation activity of the copper-ceria–iron oxide catalysts prepared with chelating-impregnation (CI) and incipient wetness impregnation (IWI). Copper based and gold based catalysts showed similar activity in CO oxidation reaction. For preferential oxidation reaction copper based catalysts show superior activity and selectivity. Gold based catalysts seems to be deactivated in presence of hydrogen in the feed.

## References


[1] The Outlook for Energy: A View to 2040, in.

[2] G. Kolb, Fuel Processing, Wiley-VCH Verlag GmbH & Co. 2008, pp. 1-2.

[3] http://www.hydrogensociety.net/hydrogen_challenge.htm.

[4] J.M. Ogden, Hydrogen: The Fuel of the Future?, Physics Today, 55 (2002) 69-75.

[5] J.M. Ogden, Annual Review of Energy and the Environment, 24 (1999) 227-279.

[6] K.K.P.a.R.B. Gupta, Hydrogen Fuel: Production, Transport, and Storage, *Chapter 1* Production and Use of Hydrogen Fundamentals and Use of Hydrogen as a Fuel (2008 ) 9.

[7] Hydrogen as an energy carrier"Royal Belgian Academy council of Applied Science (2006) Page 4.

[8] J.H. Gibbons, The hype about hydrogen, *Chapter 4*. Hydrogen production, (2004) 67.

[9] Hydrogen as an energy carrier"Royal Belgian Academy council of Applied Science (2006) 33.

[10] A. Züttel, Materials Today, 6 (2003) 24-33.

[11] M. Momirlan, T. Veziroğlu, Renewable and Sustainable Energy Reviews 3 (1999) 219-231.

[12] M. Momirlan, T.N. Veziroglu, Renewable and Sustainable Energy Reviews, 6 (2002) 141-179.

[13] C. Hulteberg, International Journal of Hydrogen Energy, 37 (2012) 3978-3992.

[14] S.S. Bharadwaj, L.D. Schmidt, Fuel Processing Technology, 42 (1995) 109-127.

[15] M.A. Pen˜a, J.P. Gómez, J.L.G. Fierro, Applied Catalysis A: General, 144 (1996) 7-57.

[16] K. Kusakabe, K.-I. Sotowa, T. Eda, Y. Iwamoto, Fuel Processing Technology, 86 (2004) 319-326.

[17] D.L. Trimm, Z.I. Önsan, Catalysis Reviews, 43 (2001) 31-84.

[18] J.N. Armor, Applied Catalysis A: General, 176 (1999) 159-176.

[19] O. Sidjabat, D.L. Trimm, Topics in Catalysis 11-12 (2000) 279-282.

[20] D.L. Trimm, Catalysis Today, 37 (1997) 233-238.

[21] I. Chorkendorff, J.W. Niemantsverdriet, Heterogeneous Catalysis in Practice: Hydrogen, in: Concepts of Modern Catalysis and Kinetics, Wiley-VCH (2005) 301-348.

[22] D.R. Palo, R.A. Dagle, J.D. Holladay, Chemical Reviews, 107 (2007) 3992-4021.

[23] C. Song, Catalysis Today 77 (2002) 17-49.

[24] N. Iwasa, S. Kudo, H. Takahashi, S. Masuda, N. Takezawa, Catalysis Letters, 19 (1993) 211-216.

[25] J.D. Holladay, J. Hu, D.L. King, Y. Wang, Catalysis Today 139 (2009) 244-260.

[26] K. Heitnes Hofstad, J.H.B.J. Hoebink, A. Holmen, G.B. Marin Catalysis Today, 40 (1998) 157-170.

[27] D. Dissanayake, M.P. Rosynek, K.C.C. Kharas, J.H. Lunsford, Journal of Catalysis 132 (1991) 117-127.

[28] P.D.F. Vernon, M.L.H. Green, A.K. Cheetham, A.T. Ashcroft, Catalysis Today 13 (1992) 417-426.

[29] A.T. Ashcroft, A.K. Cheetham, M.L.H. Green, P.D.F. Vernon, Nature 352 (1991) 225- 226.

[30] P. S. Maiya, T. J. Anderson, R. L. Mieville, J. T. Dusek, J. J. Picciolo, U. Balachandran, Applied Catalysis A: General, 196 (2000) 65-72.

[31] J.R. Rostrup-Nielsen, Catalysis Today 71 (2002) 243-247.

[32] B. Li, S. Kado, Y. Mukainakano, T. Miyazawa, T. Miyao, S. Naito, K. Okumura, K. Kunimori, K. Tomishige, Journal of Catalysis, 245 (2007) 144-155.

[33] B.S. Çağlayan, A.K. Avcı, Z.İ. Önsan, A.E. Aksoylu, Applied Catalysis A: General 280 (2005) 181-188.

[34] B.S. Çağlayan, Z. İlsen Önsan, A. Erhan Aksoylu, Catalysis Letters 102 (2005) 63-67.

[35] D.J. Wilhelm, D.R. Simbeck, A.D. Karp, R.L. Dickenson, Fuel Processing Technology 71 (2001) 139-148.

[36] D.S. Newsome, Catalysis Reviews 21 (1980) 275-318.

[37] Y. Choi, H.G. Stenger, Journal of Power Sources 124 (2003) 432-439.

[38] C. Ratnasamy, J.P. Wagner, Catalysis Reviews, 51 (2009) 325-440.

[39] J.R. Ladebeck, J.P. Wagner, Catalyst development for water–gas shift, in: Handbook of Fuel Cells, John Wiley & Sons, Ltd, 2010.

[40] K.-O. Hinrichsen, K. Kochloefl, M. Muhler, Water Gas Shift and COS Removal, in: Handbook of Heterogeneous Catalysis, Wiley-VCH Verlag GmbH & Co. KGaA, 2008.

[41] G. J. C.Gonzalez, M. G.,, M.A. Laborde, N. Moreno, Applied Catalysis, 3 (1986) 3-13.

[42] J.C. Gonzalez, M.G. Gonzalez, M.A. Laborde, N. Moreno, Applied Catalysis 20 (1986) 3-13.

[43] Y. Lei, N.W. Cant, D.L. Trimm, Catalysis Letters, 103 (2005) 133-136.

[44] S. Natesakhawat, X. Wang, L. Zhang, U.S. Ozkan, Journal of Molecular Catalysis A: Chemical, 260 (2006) 82-94.

[45] G.C. de Araújo, M. do Carmo Rangel, Catalysis Today 62 (2000) 201-207.

[46] C. Rhodes, B. Peter Williams, F. King, G.J. Hutchings, Catalysis Communications 3 (2002) 381-384.

[47] G.C. Araujo, M.C. Rangel, An environmental friendly catalyst for the high temperature shift reaction, in: F.V.M.S.M. Avelino Corma, G.F. José Luis (Eds.) Studies in Surface Science and Catalysis, Elsevier, 2000, pp. 1601-1606.

[48] A. Andreev, V. Idakiev, D. Mihajlova, D. Shopov, Applied Catalysis, 22 (1986) 385-387.

[49] P. Kappen, J.-D. Grunwaldt, B.S. Hammershøi, L. Tröger, B.S. Clausen, Journal of Catalysis, 198 (2001) 56-65.

[50] D.G. Rethwisch, J.A. Dumesic, Applied Catalysis 21 (1986) 97-109.

[51] F.M. Gottschalk, R.G. Copperthwaite, M. Van Der Riet, G.J. Hutchings, Applied Catalysis, 38 (1988) 103-108.

[52] F.M. Gottschalk, G.J. Hutchings, Applied Catalysis 51 (1989) 127-139.

[53] C. Callaghan, I. Fishtik, R. Datta, M. Carpenter, M. Chmielewski, A. Lugo, Surface Science 541 (2003) 21-30.

[54] C. Rhodes, G.J. Hutchings, A.M. Ward, Catalysis Today 23 (1995) 43-58.

[55] A. Faur Ghenciu, Current Opinion in Solid State and Materials Science 6 (2002) 389-399.

[56] D. Mendes, A. Mendes, L.M. Madeira, A. Iulianelli, J.M. Sousa, A. Basile, Asia- Pacific Journal of Chemical Engineering 5 (2010) 111-137.

[57] D. Andreeva, V. Idakiev, T. Tabakova, A. Andreev, Journal of Catalysis 158 (1996) 354-355.

[58] A. Luengnaruemitchai, S. Osuwan, E. Gulari, Catalysis Communications 4 (2003) 215-221.

[59] D. Andreeva, V. Idakiev, T. Tabakova, L. Ilieva, P. Falaras, A. Bourlinos, A. Travlos, Catalysis Today 72 (2002) 51-57.

[60] F. Boccuzzi, A. Chiorino, M. Manzoli, D. Andreeva, T. Tabakova, L. Ilieva, V. Iadakiev, Catalysis Today 75 (2002) 169-175.

[61] O. Goerke, P. Pfeifer, K. Schubert, Applied Catalysis A: General, 263 (2004) 11-18.

[62] P. Panagiotopoulou, J. Papavasiliou, G. Avgouropoulos, T. Ioannides, D.I. Kondarides, Chemical Engineering Journal, 134 (2007) 16-22.

[63] A. Goguet, F. Meunier, J.P. Breen, R. Burch, M.I. Petch, A. Faur Ghenciu, Journal of Catalysis, 226 (2004) 382-392.

[64] G. Germani, Y. Schuurman, AIChE Journal, 52 (2006) 1806-1813.

[65] E. Xue, M. O'Keeffe, J.R.H. Ross, Catalysis Today, 30 (1996) 107-118.

[66] P. Panagiotopoulou, D.I. Kondarides, Journal of Catalysis, 225 (2004) 327-336.

[67] A. Basińska, T.P. Maniecki, W.K. Jóźwiak, Reaction Kinetics and Catalysis Letters, 89 (2006) 319-324.

[68] X. Wang, R.J. Gorte, J.P. Wagner, Journal of Catalysis, 212 (2002) 225- 230.

[69] W. Ruettinger, X. Liu, R.J. Farrauto, Applied Catalysis B: Environmental, 65 (2006) 135-141.

[70] S. Golunski, R. Rajaram, N. Hodge, G.J. Hutchings, C.J. Kiely, Catalysis Today, 72 (2002) 107-113.

[71] M. A. Hurtado-Juan, C. M.Y. Yeung, S .C. Tsang, Catalysis Communications, 9 (2008) 1551-1557.

[72] A.S. Quiney, Y. Schuurman, Chemical Engineering Science, 62 (2007) 5026-5032.

[73] J.B. Ko, C.M. Bae, Y.S. Jung, D.H. Kim, Catalysis Letters, 105 (2005) 157-161.

[74] Y. Li, Q. Fu, M. Flytzani-Stephanopoulos, Applied Catalysis B: Environmental, 27 (2000) 179-191.

[75] R.J. Gorte, S. Zhao, Catalysis Today, 104 (2005) 18-24.

[76] S. Royer, D. Duprez, ChemCatChem 3 (2011) 24-65.

[77] V.M. Schmidt, P. Bröckerhoff, B. Höhlein, R. Menzer, U. Stimming, Journal of Power Sources, 49 (1994) 299-313.

[78] H.A. Gasteiger, N. Markovic, P.N. Ross, E.J. Cairns, The Journal of Physical Chemistry 98 (1994) 617-625.

[79] Z.İ. ÖNSAN, Turkish Journal of Chemistry 31 (2007) 531.

[80] H. Igarashi, T. Fujino, M. Watanabe, Journal of Electroanalytical Chemistry, 391 (1995) 119-123.

[81] H.F. Oetjen, V.M. Schmidt, U. Stimming, F. Trila, Journal of the Electrochemical Society, 143 (1996) 3838-3842.

[82] N. Bion, F. Epron, M. Moreno, F. Mariño, D. Duprez, Topics in Catalysis 51 (2008) 76-88.

[83] B. Wen, M. He, Applied Catalysis B: Environmental, 37 (2002) 75-82.

[84] B. Srinivasan, S.D. Gardner, Surface and Interface Analysis, 26 (1998) 1035-1049.

[85] D.S. Stark, M.R. Harris, Journal of Physics E: Scientific Instruments 16 (1983) 492.

[86] D.R. Schryer, B.T. Upchurch, J.D. Van Norman, K.G. Brown, J. Schryer, Journal of Catalysis, 122 (1990) 193-197.

[87] D.R. Schryer, B.T. Upchurch, B.D. Sidney, K.G. Brown, G.B. Hoflund, R.K. Herz, Journal of Catalysis, 130 (1991) 314-317.

[88] P. Thormählen, M. Skoglundh, E. Fridell, B. Andersson, Journal of Catalysis, 188 (1999) 300-310.

[89] G.C. Bond, L.R. Molloy, M.J. Fuller, Journal of the Chemical Society, Chemical Communications, (1975) 796-797.

[90] A.V. Salker, R.K. Kunkalekar, Catalysis Communications 10 (2009) 1776-1780.

[91] G. Dong, J. Wang, Y. Gao, S. Chen, Catalysis Letters, 58 (1999) 37-41.

[92] S.D. Gardner, G.B. Hoflund, M.R. Davidson, H.A. Laitinen, D.R. Schryer, B.T. Upchurch, Langmuir 7 (1991) 2140-2145.

[93] S.D. Gardner, G.B. Hoflund, B.T. Upchurch, D.R. Schryer, E.J. Kielin, J. Schryer, Journal of Catalysis, 129 (1991) 114-120.

[94] Au/MnOx catalytic performance characteristics for low-temperature carbon monoxide oxidation, Applied Catalysis B Environmental, 6 (1995) 117.

[95] S. Minicò, S. Scirè, C. Crisafulli, A.M. Visco, S. Galvagno, Catalysis Letters, 47 (1997) 273-276.

[96] M. Haruta, S. Tsubota, T. Kobayashi, H. Kageyama, M.J. Genet, B. Delmon, Journal of Catalysis, 144 (1993) 175-192.

[97] A.P. Kozlova, A.I. Kozlov, S. Sugiyama, Y. Matsui, K. Asakura, Y. Iwasawa, Journal of Catalysis, 181 (1999) 37-48.

[98] M. Haruta, N. Yamada, T. Kobayashi, S. Iijima, Journal of Catalysis, 115 (1989) 301-309.

[99] M.A.P. Dekkers, M.J. Lippits, B.E. Nieuwenhuys, Catalysis Letters, 56 (1998) 195-197.

[100] S.D. Lin, M. Bollinger, M.A. Vannice, Catalysis Letters, 17 (1993) 245-262.

[101] J.-D. Grunwaldt, M. Maciejewski, O.S. Becker, P. Fabrizioli, A. Baiker, Journal of Catalysis, 186 (1999) 458-469.

[102] U.R. Pillai, S. Deevi, Applied Catalysis A: General, 299 (2006) 266-273.

[103] S.A.C. Carabineiro, S.S.T. Bastos, J.J.M. Órfão, M.F.R. Pereira, J.J. Delgado, J.L. Figueiredo, Applied Catalysis A: General, 381 (2010) 150-160.

[104] I. Dobrosz-Gómez, I. Kocemba, J. Rynkowski, Catalysis Letters, 128 (2009) 297-306.

[105] K.M. Parida, N. Sahu, P. Mohapatra, M.S. Scurrell, Journal of Molecular Catalysis A: Chemical, 319 (2010) 92-97.

[106] T.R. Reina, S. Ivanova, M.I. Domínguez, M.A. Centeno, J.A. Odriozola, Applied Catalysis A: General, 419–420 (2012) 58-66.

[107] Y.-B. Tu, J.-Y. Luo, M. Meng, G. Wang, J.-J. He, International Journal of Hydrogen Energy, 34 (2009) 3743-3754.

[108] L.-H. Chang, N. Sasirekha, B. Rajesh, Y.-W. Chen, Separation and Purification Technology, 58 (2007) 211-218.

[109] Y.-S. Chi, H.-P. Lin, C.-Y. Mou, Applied Catalysis A: General, 284 (2005) 199-206.

[110] C.-m. Yang, M. Kalwei, F. Schüth, K.-j. Chao, Applied Catalysis A: General, 254 (2003) 289-296.

[111] E. Rombi, M.G. Cutrufello, C. Cannas, M. Casu, D. Gazzoli, M. Occhiuzzi, R. Monaci, I. Ferino, Physical Chemistry Chemical Physics, 11 (2009) 593-602.

[112] C.L. Peza-Ledesma, L. Escamilla-Perea, R. Nava, B. Pawelec, J.L.G. Fierro, Applied Catalysis A: General, 375 (2010) 37-48.

[113] L. Escamilla-Perea, C.L. Peza-Ledesma, R. Nava, E.M. Rivera-Muñoz, B. Pawelec, J.L.G. Fierro, Catalysis Communications, 15 (2011) 108-112.

[114] L. Escamilla-Perea, R. Nava, B. Pawelec, M.G. Rosmaninho, C.L. Peza-Ledesma, J.L.G. Fierro, Applied Catalysis A: General, 381 (2010) 42-53.

[115] M. Cutrufello, E. Rombi, C. Cannas, M. Casu, A. Virga, S. Fiorilli, B. Onida, I. Ferino, Journal of Materials Science, 44 (2009) 6644-6653.

[116] M. Comotti, W.-C. Li, B. Spliethoff, F. Schüth, Journal of the American Chemical Society, 128 (2005) 917-924.

[117] M. Haruta, Gold as a novel catalyst in the 21st century: Gold Bulletin, 37 (2004) 27-36.

[118] ONBOARD FUEL CONVERSION FOR HYDROGEN-FUEL-CELL-DRIVEN VEHICLES, Catalysis Reviews, 43 (2001) 31.

[119] H.-K. Lin, C.-B. Wang, H.-C. Chiu, S.-H. Chien, Catalysis Letters, 86 (2003) 63- 68.

[120] Y. Yu, T. Takei, H. Ohashi, H. He, X. Zhang, M. Haruta, Journal of Catalysis, 267 (2009) 121-128.

[121] X. Xie, Y. Li, Z.-Q. Liu, M. Haruta, W. Shen, Nature, 458 (2009) 746-749.

[122] G.G. Jernigan, G.A. Somorjai, Journal of Catalysis, 147 (1994) 567-577.

[123] T.-J. Huang, D.-H. Tsai, Catalysis Letters, 87 (2003) 173-178.

[124] H. Imagawa, A. Suda, K. Yamamura, S. Sun, The Journal of Physical Chemistry C, 115 (2011) 1740-1745.

[125] W. Liu, M. Flytzani-Stephanopoulos, The Chemical Engineering Journal and the Biochemical Engineering Journal, 64 (1996) 283-294.

[126] W. Liu, M. Flytzanistephanopoulos, Journal of Catalysis, 153 (1995) 304-316.

[127] W. Liu, M. Flytzanistephanopoulos, Journal of Catalysis, 153 (1995) 317-332.

[128] M.-F. Luo, J.-M. Ma, J.-Q. Lu, Y.-P. Song, Y.-J. Wang, Journal of Catalysis, 246 (2007) 52-59.

[129] W. Shen, X. Dong, Y. Zhu, H. Chen, J. Shi, Microporous and Mesoporous Materials, 85 (2005) 157-162.

[130] J. Zhu, Q. Gao, Z. Chen, Applied Catalysis B: Environmental, 81 (2008) 236-243.

[131] M.-F. Luo, Y.-P. Song, J.-Q. Lu, X.-Y. Wang, Z.-Y. Pu, The Journal of Physical Chemistry C, 111 (2007) 12686-12692.

[132] H. Bao, X. Chen, J. Fang, Z. Jiang, W. Huang, Catalysis Letters, 125 (2008) 160-167.

[133] G. Dutta, U.V. Waghmare, T. Baidya, M.S. Hegde, K.R. Priolkar, P.R. Sarode, Chemistry of Materials, 18 (2006) 3249-3256.

[134] J.-L. Cao, Q.-F. Deng, Z.-Y. Yuan, Journal of Materials Science, 44 (2009) 6663-6669.

[135] R. Lin, M.-F. Luo, Y.-J. Zhong, Z.-L. Yan, G.-Y. Liu, W.-P. Liu, Applied Catalysis A: General, 255 (2003) 331-336.

[136] Z.-Q. Zou, M. Meng, L.-H. Guo, Y.-Q. Zha, Journal of Hazardous Materials, 163 (2009) 835-842.

[137] D.L. Trimm, Applied Catalysis A: General, 296 (2005) 1-11.

[138] E.D. Park, D. Lee, H.C. Lee, Catalysis Today, 139 (2009) 280-290.

[139] M.J. Kahlich, H.A. Gasteiger, R.J. Behm, Journal of Catalysis 171 (1997) 93.

[140] S.H. Oh, R.M. Sinkevitch, Journal of Catalysis, 142 (1993) 254-262.

[141] M.M. Schubert, H.A. Gasteiger, R. Jürgen Behm, Journal of Catalysis, 172 (1997) 256-258.

[142] M. Brown, A. Green, G. Cohn, H. Andersen, Industrial & Engineering Chemistry, 52 (1960) 841-844.

[143] M. Watanabe, H. Uchida, H. Igarashi, M. Suzuki, Chemistry Letters, 24 (1995) 21-22.

[144] H. Igarashi, H. Uchida, M. Suzuki, Y. Sasaki, M. Watanabe, Applied Catalysis A: General, 159 (1997) 159-169.

[145] M.M. Schubert, M.J. Kahlich, G. Feldmeyer, M. Huttner, S. Hackenberg, H.A. Gasteiger, R.J. Behm, Physical Chemistry Chemical Physics, 3 (2001) 1123-1131.

[146] G. Uysal, A. Akın, Z. Önsan, R. Yıldırım, Catalysis Letters, 111 (2006) 173-176.

[147] O. Korotkikh, R. Farrauto, Catalysis Today, 62 (2000) 249-254.

[148] X. Liu, O. Korotkikh, R. Farrauto, Applied Catalysis A: General, 226 (2002) 293-303.

[149] I.H. Son, A.M. Lane, Catalysis Letters, 76 (2001) 151-154.

[150] E. Şimşek, Ş. Özkara, A.E. Aksoylu, Z.I. Önsan, Applied Catalysis A: General, 316 (2007) 169-174.

[151] J.L. Ayastuy, M.P. González-Marcos, J.R. González-Velasco, M.A. Gutiérrez-Ortiz, Applied Catalysis B: Environmental, 70 (2007) 532-541.

[152] D.J. Suh, C. Kwak, J.-H. Kim, S.M. Kwon, T.-J. Park, Journal of Power Sources, 142 (2005) 70-74.

[153] J. Choi, C.B. Shin, D.J. Suh, Catalysis Communications, 9 (2008) 880-885.

[154] T. İnce, G. Uysal, A.N. Akın, R. Yıldırım, Applied Catalysis A: General, 292 ( 2005) 171-176.

[155] E.-Y. Ko, E. Park, K. Seo, H. Lee, D. Lee, S. Kim, Catalysis Letters, 110 (2006) 275-279.

[156] S. Guerrero, J.T. Miller, E.E. Wolf, Applied Catalysis A: General, 328 (2007) 27-34.

[157] S.-H. Cho, J.-S. Park, S.-H. Choi, S.-H. Kim, Journal of Power Sources, 156 (2006) 260-266.

[158] Y. Minemura, S.-i. Ito, T. Miyao, S. Naito, K. Tomishige, K. Kunimori, Chemical Communications, (2005) 1429-1431.

[159] C. Pedrero, T. Waku, E. Iglesia, Journal of Catalysis, 233 (2005) 242-255.

[160] Y.F. Han, M.J. Kahlich, M. Kinne, R.J. Behm, Applied Catalysis B: Environmental, 50 (2004) 209-218.

[161] D.W. Dabill, S.J. Gentry, H.B. Holland, A. Jones, Journal of Catalysis, 53 (1978) 164-167.

[162] J.R. Stetter, K.F. Blurton, Industrial & Engineering Chemistry Product Research and Development, 19 (1980) 214-215.

[163] S.H. Oh, G.B. Fisher, J.E. Carpenter, D.W. Goodman, Journal of Catalysis, 100 (1986) 360-376.

[164] P.J. Berlowitz, C.H.F. Peden, D.W. Goodman, The Journal of Physical Chemistry, 92 (1988) 5213-5221.

[165] G.C. Bond, D.T. Thompson, Catalysis Reviews, 41 (1999) 319-388.

[166] M.M. Schubert, V. Plzak, J. Garche, R.J. Behm, Catalysis Letters, 76 (2001) 143-150.

[167] A. Wootsch, C. Descorme, D. Duprez, Journal of Catalysis, 225 (2004) 259-266.

[168] M.J. Kahlich, H.A. Gasteiger, R.J. Behm, Journal of Catalysis, 182 (1999) 430-440.

[169] R.M. Torres Sanchez, A. Ueda, K. Tanaka, M. Haruta, Journal of Catalysis, 168 (1997) 125-127.

[170] A. Luengnaruemitchai, D. Thi Kim Thoa, S. Osuwan, E. Gulari, International Journal of Hydrogen Energy, 30 (2005) 981-987.

[171] A. Luengnaruemitchai, S. Osuwan, E. Gulari, International Journal of Hydrogen Energy, 29 (2004) 429-435.

[172] F. Moreau, G.C. Bond, Catalysis Today, 114 (2006) 362-368.

[173] L.-H. Chang, N. Sasirekha, Y.-W. Chen, W.-J. Wang, Industrial & Engineering Chemistry Research, 45 (2006) 4927-4935.

[174] T. Tabakova, G. Avgouropoulos, J. Papavasiliou, M. Manzoli, F. Boccuzzi, K. Tenchev, F. Vindigni, T. Ioannides, Applied Catalysis B: Environmental, 101 (2011) 256-265.

[175] P. Naknam, A. Luengnaruemitchai, S. Wongkasemjit, International Journal of Hydrogen Energy, 34 (2009) 9838-9846.

[176] P. Sangeetha, Y.-W. Chen, International Journal of Hydrogen Energy, 34 (2009) 7342-7347.

[177] H. Wang, H. Zhu, Z. Qin, F. Liang, G. Wang, J. Wang, Journal of Catalysis, 264 (2009) 154-162.

[178] S. Kandoi, A.A. Gokhale, L.C. Grabow, J.A. Dumesic, M. Mavrikakis, Catalysis Letters, 93 (2004) 93-100.

[179] T.S. Mozer, D.A. Dziuba, C.T.P. Vieira, F.B. Passos, Journal of Power Sources, 187 (2009) 209-215.

[180] F. Moreau, G.C. Bond, A.O. Taylor, Journal of Catalysis, 231 (2005) 105-114.

[181] R. Zanella, S. Giorgio, C.R. Henry, C. Louis, The Journal of Physical Chemistry B, 106 (2002) 7634-7642.

[182] H.S. Oh, J.H. Yang, C.K. Costello, Y.M. Wang, S.R. Bare, H.H. Kung, M.C. Kung, Journal of Catalysis, 210 (2002) 375-386.

[183] M. Haruta, Catalysis Today, 36 (1997) 153-166.

[184] Z. Zhao, M.M. Yung, U.S. Ozkan, Catalysis Communications, 9 (2008) 1465-1471.

[185] T. Bao, Z. Zhao, Y. Dai, X. Lin, R. Jin, G. Wang, T. Muhammad, Applied Catalysis B: Environmental, 119–120 (2012) 62-73.

[186] F. Mariño, C. Descorme, D. Duprez, Applied Catalysis B: Environmental, 58 (2005) 175-183.

[187] G. Avgouropoulos, T. Ioannides, C. Papadopoulou, J. Batista, S. Hocevar, H.K. Matralis, Catalysis Today, 75 (2002) 157-167.

[188] G. Avgouropoulos, T. Ioannides, H. Matralis, Applied Catalysis B: Environmental, 56 (2005) 87-93.

[189] G. Marbán, A.B. Fuertes, Applied Catalysis B: Environmental, 57 (2005) 43-53.

[190] Y. Liu, Q. Fu, M.F. Stephanopoulos, Catalysis Today, 93–95 (2004) 241-246.

[191] C.M. Bae, J.B. Ko, D.H. Kim, Catalysis Communications, 6 (2005) 507-511.

[192] G. Avgouropoulos, T. Ioannides, Applied Catalysis B: Environmental, 67 (2006) 1-11.

[193] M. Tada, R. Bal, X. Mu, R. Coquet, S. Namba, Y. Iwasawa, Chemical Communications, (2007) 4689-4691.

[194] C.R. Jung, J. Han, S.W. Nam, T.H. Lim, S.A. Hong, H.I. Lee, Catalysis Today, 93–95 (2004) 183-190.

[195] E.-Y. Ko, E.D. Park, K.W. Seo, H.C. Lee, D. Lee, S. Kim, Catalysis Today, 116 (2006) 377-383.

[196] J.B. Wang, S.-C. Lin, T.-J. Huang, Applied Catalysis A: General, 232 (2002) 107-120.

[197] J.-W. Park, J.-H. Jeong, W.-L. Yoon, H. Jung, H.-T. Lee, D.-K. Lee, Y.-K. Park, Y.-W. Rhee, Applied Catalysis A: General, 274 (2004) 25-32.

[198] J. Won Park, J. Hyeok Jeong, W.L. Yoon, C.S. Kim, D.K. Lee, Y.-K. Park, Y.W. Rhee, International Journal of Hydrogen Energy, 30 (2005) 209-220.

[199] E. Moretti, M. Lenarda, L. Storaro, A. Talon, R. Frattini, S. Polizzi, E. Rodríguez-Castellón, A. Jiménez-López, Applied Catalysis B: Environmental, 72 (2007) 149-156.

[200] P. Ratnasamy, D. Srinivas, C.V.V. Satyanarayana, P. Manikandan, R.S. Senthil Kumaran, M. Sachin, V.N. Shetti, Journal of Catalysis, 221 (2004) 455-465.

[201] Y.-Z. Chen, B.-J. Liaw, W.-C. Chang, C.-T. Huang, International Journal of Hydrogen Energy, 32 (2007) 4550-4558.

[202] L. Dong, Y. Hu, M. Shen, T. Jin, J. Wang, W. Ding, Y. Chen, Chemistry of Materials, 13 (2001) 4227-4232.

[203] C.E. Hori, H. Permana, K.Y.S. Ng, A. Brenner, K. More, K.M. Rahmoeller, D. Belton, Applied Catalysis B: Environmental, 16 (1998) 105-117.

[204] Y.-Z. Chen, B.-J. Liaw, H.-C. Chen, International Journal of Hydrogen Energy, 31 (2006) 427-435.

[205] V. Ramaswamy, S. Malwadkar, S. Chilukuri, Applied Catalysis B: Environmental 84 (2008) 21-29.

[206] D.H. Kim, J.E. Cha, Catalysis Letters, 86 (2003) 107-112.

[207] G. Sedmak, S. Hočevar, J. Levec, Journal of Catalysis, 213 (2003) 135-150.

[208] D. Gamarra, G. Munuera, A.B. Hungría, M. Fernández-García, J.C. Conesa, P.A. Midgley, X.Q. Wang, J.C. Hanson, J.A. Rodríguez, A. Martínez-Arias, Journal of Physical Chemistry C, 111 (2007) 11026-11038.

[209] T. Caputo, L. Lisi, R. Pirone, G. Russo, Industrial & Engineering Chemistry Research, 46 (2007) 6793-6800.

CHAPTER

2

# Materials and methods

## 2.1. Introduction

Catalysis has pivotal role in chemical transformations. Most of the chemical and biological reactions require catalysts. Catalysts are the backbone of many chemical and industrial processes. Heterogeneous catalysts are the most important and most sophisticated materials, which found applications in different sectors of society for instance, in environmental protection, (a well known example is catalytic converter for automobiles), energy production, polymer, textiles, food and agrochemical industries [1]. Their high demand in diverse applications and the necessity to obtain new catalytic morphologies stimulates the discovery of new approaches to the preparation of highly dispersed solids[2]. Catalytic technologies reduces many environmental issues related to the energy production [3]. The development of selective, active and stable catalytic combinations are necessary for meeting the standards of sustainable chemistry.

Recently, the demand of hydrogen as a fuel increases considerably by the development of fuel cell technology. Hydrogen is considered as an environmentally attractive fuel because of its pollution free combustion together with PEM fuel cells. Fuel cells offers high efficiency, pollution free energy production compared to internal

combustion engine. Last few decades, many efforts has been made for the development of transforming hydrocarbons into hydrogen. Industrial hydrogen production is based on steam reforming of hydrocarbons followed by water gas shift reaction and preferential oxidation to reduce the CO to an appreciable level. Present industrial catalysts for water gas shift (WGS) and preferential oxidation of CO (PROX-CO) are not appropriate for mobile and stationary applications. As far as hydrogen is not safely stored in vehicle, an on-board reforming processes is necessary for the hydrogen production. The drawbacks of the industrial catalysts (less activity and complex activation procedure) for mobile and stationary applications extends the research to the development of active, selective and stable catalytic combinations.

## 2.2. Catalyst development using hard template method

Nanoscience and nanotechnology has made remarkable development in heterogeneous catalysis. Last few decades, the development of many different preparation methods helped to optimize the properties of catalysts. To design a catalysts with desirable activity and selectivity continues to be a goal yet to be reached. The ultimate control of a catalytic process remains a great challenge[4]. Catalysis research aimed to understand the activity, selectivity and stability of a catalysts in a particular reaction at the molecular level. A heterogeneous catalytic transformation deals with the detailed understanding of the active species (reactant) adsorbed on specific sites of the catalyst, its chemical transformation, and desorption of products [5]. Nano-materials with controlled size, shape and large specific surface area is of fundamental importance in many research and technological applications, such as lithium ion batteries, gas sensors, catalysis and energy storage[6-10]. Controlling the shape of the catalysts provides a powerful tool for tailoring their catalytic properties.

The development of ordered mesoporous silicas of the M41S family have attracted much research attention owing to their highly ordered structure, tunable pore size and high surface area[11]. These specific properties makes it useful for many applications, ranging from catalysis, adsorption, sensing, and separation to biotechnology. In subsequent years research on mesoporous materials was under tremendous development. Materials with 2D-hexagonal, cubic and lamellar pore structures (MCM-41, SBA-15, MCM-48, SBA-16, KIT-6, MCM-50) prepared by using

cationic surfactants and amphiphilic block copolymers as structure directing agents (SDA). Since these pioneering studies, significant efforts has been made to develop nonsiliceous materials with controlled composition and structural ordering. But the surfactant template approach was not successful for the preparation of ordered non-siliceous materials, because of some limitations such as (i) the lack of suitable precursors, (ii) structure collapse of the material during the thermal treatments, (iii) resulting materials in most cases are lacking long range order [12-13]. But the development of nanocasting method (hard template method) seems to be an attractive alternative for the preparation of non-siliceous mesoporous materials. This method successfully applied first time for preparation of ordered mesoporous carbon (CMK – type family) by Ryoo etal [14]. After that this method successfully applied for the synthesis of metal oxides[15-18].

### 2.2.1. The Hard Template Method

The hard template (HT) is a versatile strategy for preparing ordered nano-structured porous materials, which involves the synthesis of a mesoporous solid (the template), which acts as a hard host for the growth, from an appropriate molecular precursor, of the guest metal oxide. Such growth is confined into the pore system of the template, which can then be removed (by leaching, for instance) leaving the guest replica of the topological structure of the host. Using ordered mesoporous silicas as hard templates, for instance, the two-dimensional hexagonal SBA-15 and the three-dimensional cubic KIT-6, a hard template process can be carried out to obtain replicated mesostrutures constructed by nanorod, nanowire or nanotube array. Hard template (HT) method resembles the concept of the casting method in metallurgy this method conceptually scale down to the nanoscale range to synthesize nano-structured material using mesoporous silicas (Fig.)[19].

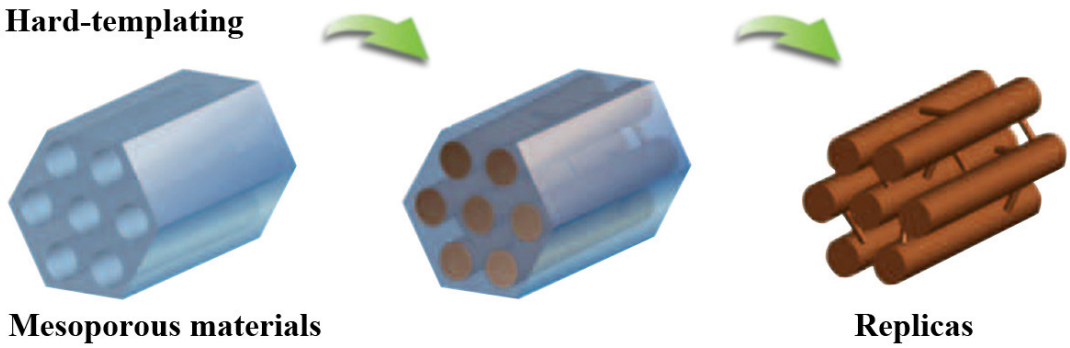


**Figure 2.1**. Schematic representation of the hard template concept [19]

### 2.2.2. The procedure of hard template method

In the hard template method the first step is to fill the mesopores of the silicas by the precursor for the desired product either by "wet impregnation" or by the "incipient wetness" technique (Fig.2.2). In the former case, the template (mesoporous silica) is dispersed in dilute solution of the precursor; the dissolved precursor species in solution diffuse into the pores where they adsorbed into the pore walls. The impregnation process continued several cycles to get better loading of the precursor. In the latter method, a saturated precursor solution is used, the volume of the solution is restricted to the pore volume of the template to be filled. The purpose of this method is to avoid the precursor deposition on the outer surface of the template matrix and to obtain higher loading of the precursor inside the pores by capillary forces[19-20].

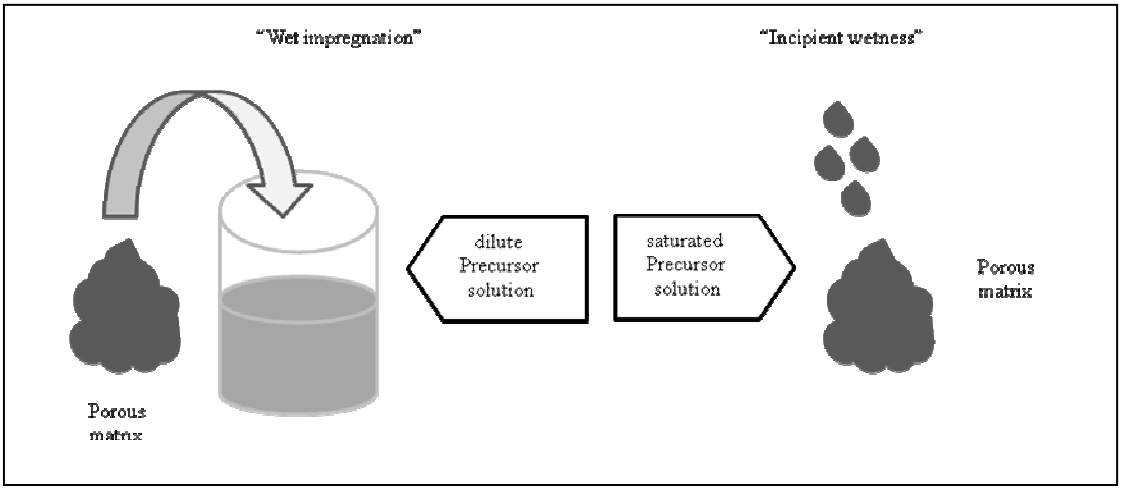


**Figure 2.2.** Schematic representation of "wet impregnation" and "incipient wetness impregnation" techniques for the infiltration of precursor species into porous structure matrices[20].

### 2.2.3. Factors affecting hard template method

The most important process in hard template method is to increase the loading of the guest molecules in the mesopore channels of the host (template). The main driving force that promoting the movement of the guest molecules into the mesopores is comes from capillary force[21]. The interaction of the inorganic precursor (guest) with the mesopore surface of the host is also a fundamental point, weak interaction between silica wall and precursor may decrease the capillary function and thereby results a partial loading, thus producing disordered nanowires or nanoparticles[22]. The complicated factors that determined the interaction between the silica wall and the precursor are: Hydrogen bonding, Co-ordination boning, Coulombic interactions, Van der walls forces [23].

#### *2.2.3.1. Hydrogen bonding*

The amorphous pore walls of the mesoporous silicas containing silanol groups (Si-OH) are noticeable in attracting guest molecules, which participates in the hydrogen bonding with electronegative atoms (e.g., oxygen atoms) of the guest precursors. The more silanol group on the pore walls retained, the stronger interaction between the host and guest may occur or otherwise we can say the interaction between the hard template and the precursor solution is directly proportional to the amount of silanol groups on the pore walls [24].

#### *2.2.3.2. Co-ordination bonding*

The hydroxy group on the amorphous silica wall of the template can act as ligands. The metal- ligand interactions between the template and the precursors results the formation of a co-ordination bond thereby the production of complexes[25]. This type of interactions (chelation) can also increase the loading rate of the precursors into the mesopore channels of the host.

#### *2.2.3.3. Coulombic interactions*

The amorphous silica walls of the templates possess abundant negatively charged oxygen atoms distributed on the surface. During the impregnation process, Coulombic

Interactions between the silica walls and the precursors exist, which influence the loading rate of the precursor in the mesopore channels of the template.

*2.2.3.4. Van der Waals forces*

Van der Waals interaction is extremely important for the migration of precursor metal ions into the surface of the mesopore channels. The ion migration helps to transfer the precursors completely into the mesopores. This force is also important for inter-linking of the nanoparticles in the annealing stage. This interaction also enhances the precursor loading.

### 2.2.4. Advantages of Hard Template Method

Hard template method offers many advantages using mesoporous silica as template structure. First of all it opens an alternative route for preparing various mesoporous metal oxides which is very complicated to synthesize using traditional surfactant template method. The mesoporous silica template with the mesopore, 2-10 nm range can serve as nanoreactors and the obtained materials are also in nanometer range. Variable mesostructure of the silica hosts helps to obtain alternative topologies, such as 1-D nanowire arrays or 3-D bicontinuous nanowire array. Thermal stability of the silica material is another advantage of the hard template method, which helps to carried out the synthesis at much higher temperatures with controlled structure and morphology.

## 2.3. Experimental setup for low temperature CO oxidation (LT-CO) and preferential oxidation of CO (PROX-CO)

The experimental setup used for the low temperature CO oxidation (LT-CO) and preferential oxidation of CO (PROX-CO) are shown in Fig.2.3. For low temperature CO oxidation 1:1 vol% of CO and $O_2$ (5 vol% in He) with He (total flow, 55 $cm^3$ $min^{-1}$) is passed through the reactor contain 30 mg of catalyst. For preferential oxidation 1:1 vol% of CO and $O_2$, 46 vol% $H_2$, balance He (total flow, 55 $cm^3$ $min^{-1}$) is used. Temperature programmer connected with a thermocouple is used to programme the reaction temperatures (for both reaction 40-200°C temperature range is used). Gas flow rate is controlled by using mass flow controller connected in the gas lines. Every 30 min

the effluent gas coming out from the reactor in analyzed with a HP 6890 gas chromatograph equipped with a HP Poraplot Q capillary column and both TCD and FID (coupled with a methanator) detectors. Liquid $CO_2$ is used to cool down the oven temperature of the GC to -40°C.

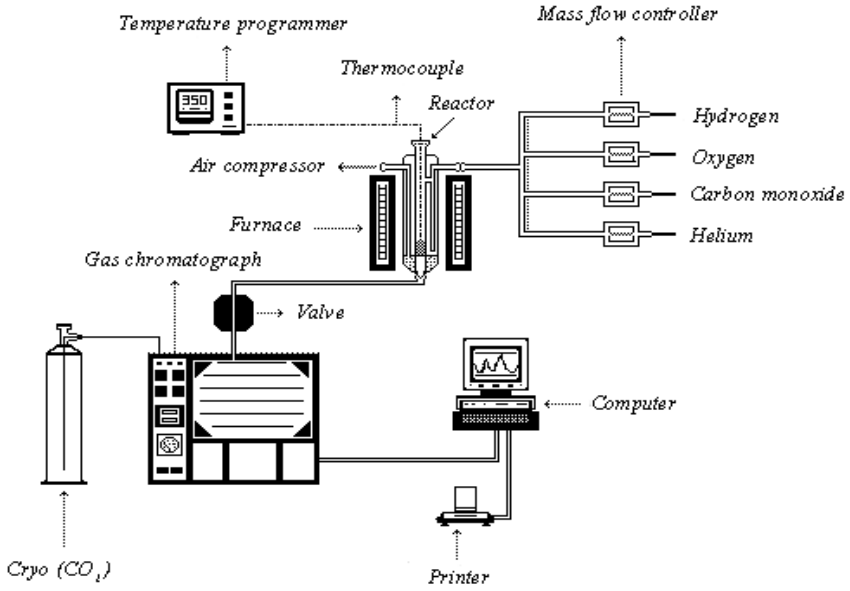


**Figure 2.3.** Experimental setup for low temperature CO oxidation and preferential oxidation of CO

## References

[1] J. Hagen, Industrial Catalysis, Wiley-VCH Verlag GmbH & Co. KGaA, 2006, pp. 1-14.

[2] B. Delmon, Solid State Ionics 16 (1985) 243-249.

[3] K.I. Zamaraev, Catalysis Today 35 (1997) 3-13.

[4] S.H. Bing Zhou, Robert Raja and Gabor A. Somorjai, Nanotechnology in Catalysis Vol.3 P.1.

[5] K. Zhou, Y. Li, Angewandte Chemie International Edition 51 (2012) 602-613.

[6] G.J. Thorogood, B.J. Kennedy, C.S. Griffith, M.M. Elcombe, M. Avdeev, J.V. Hanna, S.K. Thorogood, V. Luca, Chemistry of Materials 22 (2010) 4222-4231.

[7] S. Sun, H. Zeng, Journal of the American Chemical Society 124 (2002) 8204-8205.

[8] A.R. Armstrong, P.G. Bruce, Nature 381 (1996) 499-500.

[9] A.J. Zarur, J.Y. Ying, Nature 403 (2000) 65-67.

[10] L. Hu, Q. Peng, Y. Li, Journal of the American Chemical Society 130 (2008) 16136-16137.

[11] C.T. Kresge, M.E. Leonowicz, W.J. Roth, J.C. Vartuli, J.S. Beck, Nature 359 (1992) 710-712.

[12] P. Yang, D. Zhao, D.I. Margolese, B.F. Chmelka, G.D. Stucky, Nature 396 (1998) 152-155.

[13] A. Sayari, P. Liu, Microporous Materials 12 (1997) 149-177.

[14] R. Ryoo, S.H. Joo, S. Jun, The Journal of Physical Chemistry B 103 (1999) 7743-7746.

[15] A. Rumplecker, F. Kleitz, E.-L. Salabas, F. Schüth, Chemistry of Materials 19 (2007) 485-496.

[16] F. Jiao, A.H. Hill, A. Harrison, A. Berko, A.V. Chadwick, P.G. Bruce, Journal of the American Chemical Society 130 (2008) 5262-5266.

[17] C. Dickinson, W. Zhou, R.P. Hodgkins, Shi, Zhao, He, Chemistry of Materials 18 (2006) 3088-3095.

[18] S.C. Laha, R. Ryoo, Chemical Communications (2003) 2138-2139.

[19] Y. Yamauchi, N. Suzuki, L. Radhakrishnan, L. Wang, The Chemical Record 9 (2009) 321-339.

[20] M. Tiemann, Chemistry of Materials 20 (2007) 961-971.

[21] Y. Wan, H. Yang, D. Zhao, Accounts of Chemical Research 39 (2006) 423-432.

[22] B.J. Scott, G. Wirnsberger, G.D. Stucky, Chemistry of Materials 13 (2001) 3140-3150.

[23] H. Yang, D. Zhao, Journal of Materials Chemistry 15 (2005) 1217-1231.

[24] B. Tian, X. Liu, C. Yu, F. Gao, Q. Luo, S. Xie, B. Tu, D. Zhao, Chemical Communications (2002) 1186-1187.

[25] Y. Wang, C.M. Yang, W. Schmidt, B. Spliethoff, E. Bill, F. Schüth, Advanced Materials 17 (2005) 53-56.

CHAPTER

3

# Low temperature CO oxidation and preferential oxidation of CO over $CuO\text{-}Co_3O_4$ spinel catalysts

## 3.1. Introduction

Spinels are a group of crystalline compounds with the general formula $AB_2X_4$, where A and B represents the divalent and trivalent cation in the tetrahedral and octahedral site, respectively and X is chalcogen (X= O, S, Se, Te). Spinels have received great deal of research interest due to its diverse properties and wide range of applications including magnetism, electronics and catalysis, energy storage and conversion[1-4]. Spinels are built with a cubic close packed array of $X^{2-}$ ions, with $A^{2+}$ and $B^{3+}$ cations occupying all of the tetrahedral and octahedral holes, respectively (Fig.3.1) [5]. The unit cell of a normal spinel consists of 32 cubic-close-packed oxygen anions. In this unit cell, 8 of the 64 tetrahedral (A site) interstices are filled with divalent metal cations, and 16 of the 32 octahedral (B site) interstices are filled with trivalent metal cations (Fig.3.1)[6].

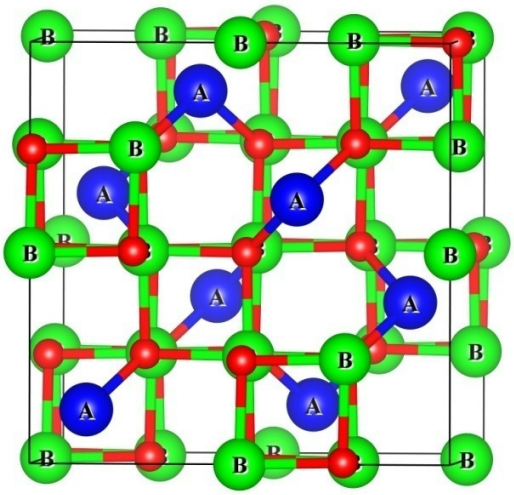


**Figure 3.1**. Schematic representation of the unit cell $AB_2X_4$

There are about 1000 known spinels including ~130 oxides, among these, transition metal oxide spinels for instance, tricobalt tetroxide ($Co_3O_4$) have received great research attention as active component in Li-ion batteries, gas sensing[7], electronic devices and heterogeneous catalysts[8]. Cobalt oxide is composed of cubic spinel type structure with $Co^{2+}$ and $Co^{3+}$ cations mostly occupying in the tetrahedral and octahedral sites, respectively. The unit cell contains 56 atoms (32 $O^{2-}$ anions, 16 $Co^{3+}$ and 8 $Co^{2+}$ cations).The $Co^{2+}$ ions in the tetrahedral site has a $d^7$ electronic configuration of high-spin state ($e^4t_2^3$), whereas the $Co^{3+}$ ions in the octahedral site has a $d^6$ configuration of low-spin state ($t^6_{2g}$) [9]. Fig. 3.2 show a polyhedral model of $Co_3O_4$ spinel, where A represents the divalent $Co^{2+}$ cation in the tetrahedral sites and B represents the $Co^{3+}$ cations in the octahedral sites.

Spinel structures are versatile due to its ability to accommodate a wide range of metal cations and oxidation states, these properties make it as a model system for many fundamental studies. Recently, mixed oxide spinel structures are of intense interest in material research because of its remarkable optical, magnetic, and catalytic properties. Partial substitution of spinels with other 3d-transition metals are useful for tuning the structural, optical and catalytic properties of the material [9-10]. Cobalt oxide and cobalt

oxide based materials are extensively used as a heterogeneous catalyst for many chemical transformations such as, CO oxidation [8, 11-14], $NO_x$ abatement, Fischer- Tropsch synthesis[15-16], preferential oxidation of CO [17-19]. Spinel cobaltite ($MCo_2O_4$; M= Cu, Mn, Ni, Mg, etc.) are found to be more active, selective, stable and resistance to poisoning in a number of catalytic or electrocatalytic processes compared to pure cobalt oxide. The stabilization of the active species and special synergistic interactions between the two different oxides favor the performance improvement of the cobaltite[20-21]. Particle size, morphology, and porosity also have significant influence on the properties of spinels [22]. Several synthetic approaches such as, nitrate decomposition[23], urea combustion[24], co-precipitation [25], sol-gel [26], hydrothermal[27], aero-sol pyrolysis[10], anodic electrodeposition[22] are applied for the preparation of spinel cobaltites.

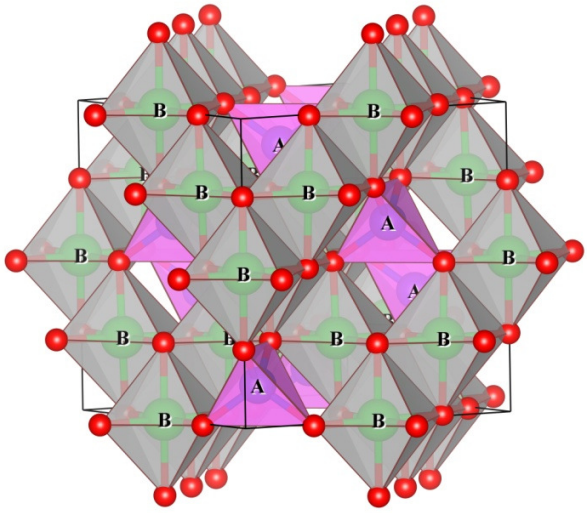


**Figure 3.2.** Schematic representation of the polyhedral model of $Co_3O_4$ spinel

The present work deals with the catalytic activity of hard-templated mesoporous CuO-$Co_3O_4$ oxides for both the low temperature CO oxidation and CO PROX in a hydrogen-rich stream. Four catalysts, with 0, 9, 13 and 17 Cu/(Co+Cu) atomic ratio (%), respectively, were prepared by using SBA-15 as a hard template. They were characterized as to their structure, morphology, texture and redox features by X-ray diffraction (XRD),

FTIR spectroscopy, transmission electron microscopy (TEM), $N_2$ physisorption and temperature-programmed reduction with hydrogen ($H_2$-TPR). The catalytic activity was tested in the 40-140 °C range for CO oxidation in the absence of hydrogen and in the 40-200 °C range for the CO PROX in a hydrogen-rich stream. In both cases a continuous-flow microreactor operated under atmospheric pressure was used.

## 3.2. **Experimental**

### *3.2.1. Materials*

Tetraethylorthosilicate (TEOS, 98 %), Pluronic copolymer P123 ($EO_{20}PO_{70}EO_{20}$), $Cu(NO_3)_2 \cdot 2.5H_2O$, $Co(NO_3)_2 \cdot 6H_2O$, NaOH and $Co_3O_4$ were supplied by Aldrich. CuO was supplied by Thermo Quest as a standard for the calibration of the TPD/R/O 1100 apparatus. HCl (37 %) was provided by Merck. All the materials were of reagent grade.

### *3.2.2. Synthesis of mesoporous silica SBA-15*

Mesostructured silica SBA-15 was prepared under hydrothermal conditions according to[28]. In a typical synthesis, 4 g of Pluronic 123 were added to 120 g of HCl (2M) and 30 g of bi-distilled water. After 15 h under stirring at 308 K, 8.5 g of TEOS were added and the solution was maintained at 308 K for 24 h under stirring. The resulting gel was then transferred into a stainless-steel autoclave and kept at 373 K for 24 h under static conditions. The obtained suspension was filtered and the recovered solid was washed with de-ionized water, dried at 313 K overnight and finally calcined in air at 823 K for 5 h.

### *3.2.3. Synthesis of mesoporous copper-cobalt mixed oxides*

copper-cobalt oxides were prepared by a hard template pathway using SBA-15 as the hard template. In a typical synthesis, cobalt and copper nitrates, in appropriate amounts to obtain the desired Cu/(Co+Cu) atomic ratio, were dissolved in 25 $cm^3$ of ethanol. 1 g of SBA-15 was then added to 15 $cm^3$ of the obtained solution and the suspension was stirred at room temperature for 1 h. Next, the solvent was evaporated at 60 °C overnight and the impregnation step was then repeated with the aim of completely filling the SBA-15 pores. The resulting solid was subsequently transferred into a furnace and kept at 550 °C for 3 h to

decompose the nitrates into oxides. Removal of the SBA-15 template was then performed by leaching with 2 M NaOH at 50 °C. Finally, the resulting material was washed up to pH 7 with distilled water and dried at 50 °C for 12 h. The obtained samples were named CuCo-*x*, where *x* (= 0, 9, 13, 17) represents the experimental Cu/(Co+Cu) atomic ratio (%).

### *3.2.4. Catalyst Characterization*

Inductively coupled plasma atomic emission spectroscopy (ICP-AES) analyses were performed with a Varian Liberty 200 spectrophotometer to determine the Cu content. Samples (0.03 g) were dissolved in concentrated nitric acid and the solution was diluted to 250 $cm^3$ with bi-distilled water.

X-ray diffraction patterns were recorded on a Seifert X3000 diffractometer with a θ-θ Bragg Brentano geometry with Cu Kα radiation.

The absorption spectra in the medium IR region (4000-400 $cm^{-1}$) were collected using an Equinox 55 (Bruker) spectrophotometer. Pellets of the samples were prepared by dispersing the finely ground powders in KBr.

Transmission electron microscopy (TEM) images were obtained on a JEOL 200CX microscope equipped with a tungsten cathode operating at 200 kV. Finely ground samples were dispersed in n-octane in an ultrasonic bath. The suspension was then dropped on a carbon-coated copper grid for observation.

Textural analysis was carried out on a Sorptomatic 1990 System (Fisons Instruments), by determining the nitrogen adsorption/desorption isotherms at -196 °C. Before analysis, the sample was heated overnight under vacuum up to 250 °C (heating rate = 1 °C $min^{-1}$).

TPR profiles were recorded on a TPD/R/O 1100 apparatus (Thermo Quest), under the following conditions: sample weight, 0.05 g; heating rate (from 40 to 800 °C), 10 °C $min^{-1}$; flow rate, 30 $cm^3$ $min^{-1}$; $H_2$, 5 vol% in $N_2$. The hydrogen consumption was monitored by a thermal conductivity detector (TCD).

### *3.2.5. Catalytic runs*

CO oxidation in the absence of hydrogen and in a hydrogen-rich stream (CO PROX) were carried out under atmospheric pressure in a quartz-glass fixed-bed continuous-flow microreactor in the 40-140 °C and 40-200 °C temperature range, respectively. The catalyst (0.03 g) was contacted with either a $CO/O_2$ mixture (total flow, 55 $cm^3$ $min^{-1}$; 1.5 vol% CO, 1.5 vol% $O_2$, balance He) or a $CO/O_2/H_2$ stream (total flow, 55 $cm^3$ $min^{-1}$; 1.5 vol% CO, 1.5 vol% $O_2$, 46 vol% $H_2$, balance He). On selected samples (CuCo-*0* and CuCo-*17*) the CO PROX reaction was also performed by using 0.1 g of catalyst. Such samples were also tested in the $H_2$ oxidation reaction by contacting 0.03 g of catalyst with an $O_2/H_2$ stream (total flow, 55 $cm^3$ $min^{-1}$; 1.5 vol% $O_2$, 46 vol% $H_2$, balance He) in the 40-200 °C temperature range. On-line analysis of the reactor effluent was performed on a HP 6890 GC, equipped with a HP Poraplot Q capillary column and both TCD and FID (coupled with a methanator) detectors. At each reaction temperature, samples were collected after 30 min on-stream to allow the attainment of steady-state conditions. Prior to the reaction the catalysts were pretreated in air (15 $cm^3$ $min^{-1}$) at 500 °C (heating rate, 1 °C $min^{-1}$) for 1 h. In the case of CO oxidation in the absence of hydrogen, a selected sample (CuCo-*17*) was also submitted to the following activation procedures: (i), pretreatment in air (15 $cm^3$ $min^{-1}$) at 150 °C (heating rate, 1 °C $min^{-1}$) for 1 h; (ii), reduction in $H_2$ (15 $cm^3$ $min^{-1}$) at 350 °C (heating rate, 5 °C $min^{-1}$) for 2 h and successive re-oxidation in air flow (15 $cm^3$ $min^{-1}$) for 1 h at the same temperature. Conversion and selectivity towards $CO_2$ have been calculated for both CO ($X_{CO}$; $S^{CO}_{CO_2}$) and $O_2$ ($X_{O_2}$; $S^{O_2}_{CO_2}$) by the following equations:

$$X_{CO}\ (\text{mol}\%) = \frac{[CO]_{in} - [CO]_{out}}{[CO]_{in}} \cdot 100; \qquad S^{CO}_{CO_2}\ (\text{mol}\%) = \frac{[CO_2]_{out}}{[CO]_{in} - [CO]_{out}} \cdot 100$$

$$X_{O_2}\ (\text{mol}\%) = \frac{[O_2]_{in} - [O_2]_{out}}{[O_2]_{in}} \cdot 100; \qquad S^{O_2}_{CO_2}\ (\text{mol}\%) = \frac{0.5 \cdot [CO_2]_{out}}{[O_2]_{in} - [O_2]_{out}} \cdot 100$$

where terms in brackets are the inlet and outlet concentrations.

## 3.3. Results and discussion

### *3.3.1 Characterization of SBA-15*

The low angle X-ray diffraction pattern of SBA-15 (Fig.3.3) shows three well-resolved peaks which can be indexed as the (100), (110), and (220) reflections characteristic of the 2-D hexagonal (*P6mm*) structure. The internal architecture of SBA-15 is clearly visible in the TEM images shown in Fig. 3.4: both the viewing directions, parallel (Fig. 3.4a) and perpendicular (Fig.3.4b) to the main axis of the pores, confirm the highly ordered 2-D hexagonal regularity. The ordered arrays of silica channels have a mean diameter of *ca.* 6-7 nm with a wall thickness of about 3 nm.

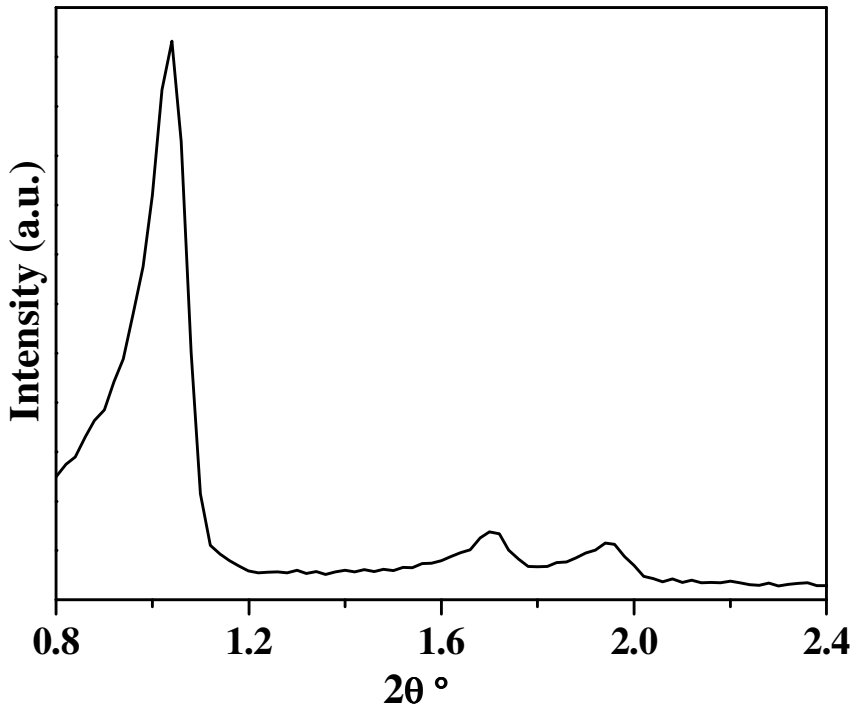


**Figure 3.3**. Low angle XRD diffraction of the SBA-15 silica template.

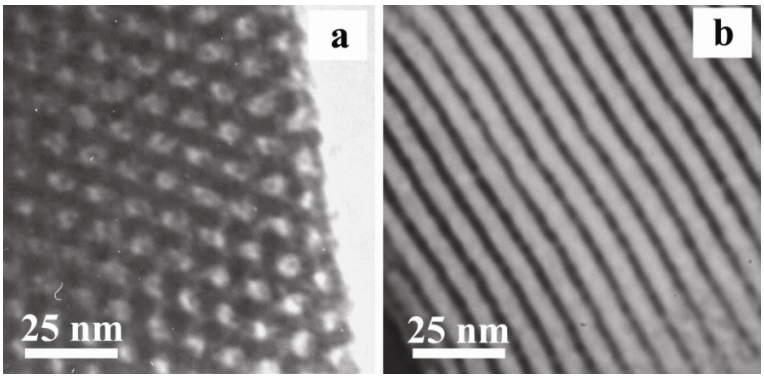


**Figure 3.4.** TEM images of the SBA-15 silica template.

Nitrogen physorption results are summarized in Fig.3.5, which shows a type IV isotherm with an H1 hysteresis loop at high relative pressures, typical of SBA-15. A surface area, $S_{BET}$, of 1080 $m^2$ $g^{-1}$ and a pore volume, $V_p$, of 1.58 $cm^3$ $g^{-1}$ were calculated from the BET equation. The BJH method was applied to the desorption branch of the isotherm to obtain the pore size distribution curve (Fig. 3.5, inset) which appears quite narrow and centered at 6.1 nm ($d_p$), in agreement with the TEM results.

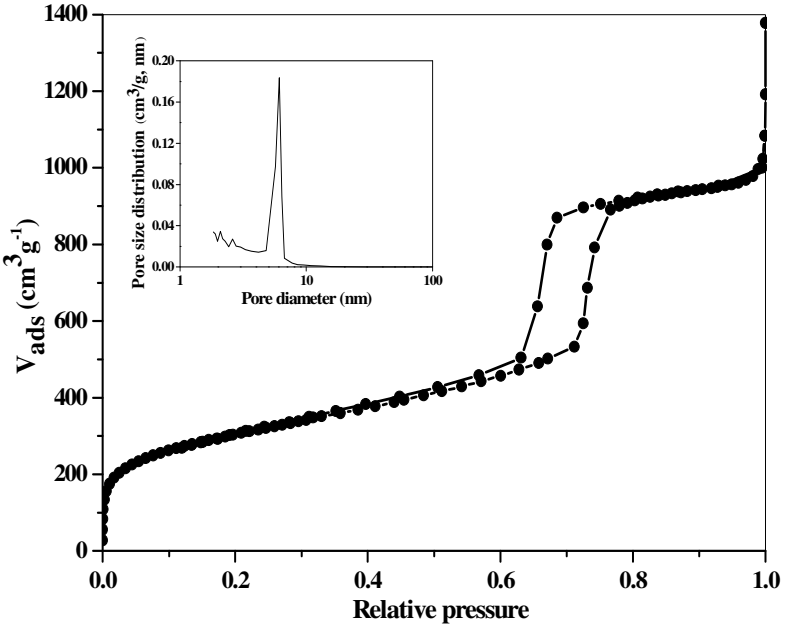


**Figure 3.5.** Nitrogen adsorption/desorption isotherm and pore size distribution plot (inset) of the SBA-15 silica template.

### *3.3.2. Characterization of CuCo-x catalysts*

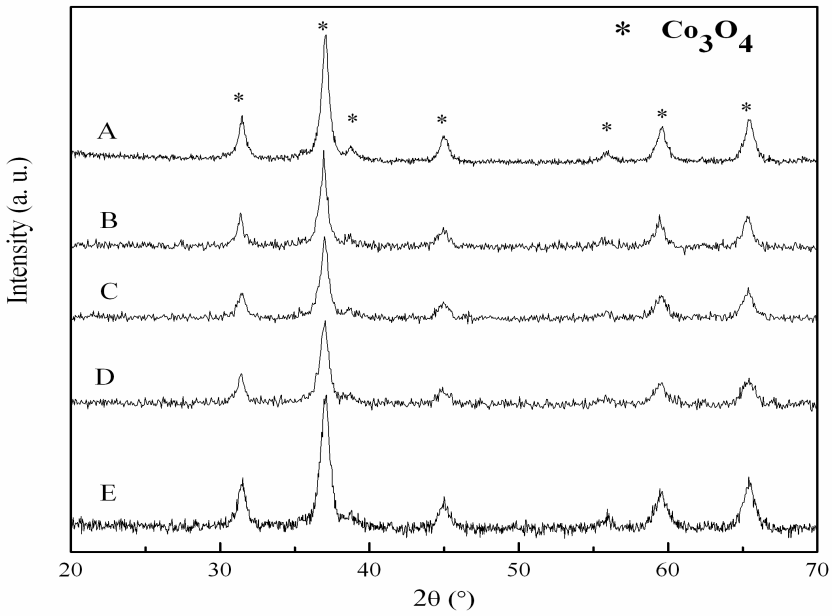


**Figure 3.6**. XRD patterns of CuCo-*x* catalysts: (A), CuCo-*0*; (B), CuCo-*9*; (C), CuCo-*13*; (D), CuCo-*17*; (E), CuCo-*17* after $N_2$ treatment at 500 °C for 6 h.

The XRD patterns of the CuCo-*x* mixed oxides are presented in Fig.3.6. The diffraction profile of the CuCo-*0* sample matches the JCPDS (PDF 74-1656) file identifying $Co_3O_4$ with face-centered cubic spinel structure (space group F*d*-3*m*), in which one eight of the tetrahedral sites are occupied by $Co^{2+}$ cations while one half of the octahedral sites are occupied by $Co^{3+}$ cations. The spinel phase is the only phase visible in the patterns of CuCo-*9,* CuCo-*13* and CuCo-*17*: no peaks corresponding to CuO or any other ordered Cu-containing phase can be detected, even at the highest loading. This seems to suggest that both $Co^{2+}$ and $Cu^{2+}$, whose diameters are very close (74.5 and 73 pm [29]), are located inside the tetrahedral holes of the cubic closely-packed structure of $O^{2-}$. In principle, the lack of evidence for a CuO phase might also depend on its high dispersion. Should this be the case, however, sharpening of the peaks induced by a high-temperature treatment would make visible such copper oxide phase. Inspection of the XRD pattern of the CuCo-*17* sample treated at 500 °C for 6 h under nitrogen (curve E in Fig. 3.6) does not

reveal any other phase besides the spinel, which supports the view that no segregated CuO phase forms during the catalyst preparation.

The presence of a CuO phase can definitely be ruled out on the basis of the FTIR results. In Fig. 3.7 the spectra of CuCo-*0* (as-made) and CuCo-*17* (either as-made or after $N_2$ treatment at 500 °C for 6 h) are compared with the spectrum of pure CuO. For the latter, in agreement with the literature [30], the typical modes of CuO are visible, located at 484 $cm^{-1}$, 538 $cm^{-1}$ (TO) and 580 $cm^{-1}$ (LO). No contribution of such bands is detected in the spectra of the CuCo-*x* samples, for which only the spinel phase is present, as revealed by the bands at 568 and 660 $cm^{-1}$. According to the literature [31-33]these bands originate from the stretching vibrations of the metal-oxygen bonds: the one at 568 $cm^{-1}$ is associated with the $OB_3$ vibration in the spinel lattice (B denotes $Co^{3+}$ in an octahedral hole) and the band at 660 $cm^{-1}$ is attributed to the $ABO_3$ vibration (A denotes the bivalent cation in a tetrahedral hole). The presence of small bands at ca. 990, 1635 and 3430 $cm^{-1}$, ascribable [34] to ν(Si-OH), δ($H_2O$) and ν($H_2O$), respectively, suggests that very low amounts of residual silica remain after the leaching process. Compared to CuCo spinels prepared by conventional coprecipitation, which undergo segregation of CuO phase upon calcination at 500 °C for 4 h [35], the present CuCo spinels appear quite stable.

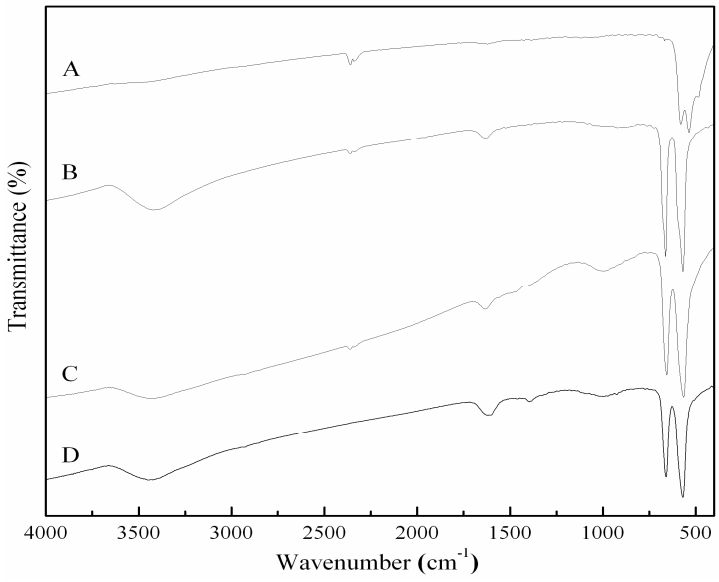

**Figure 3.7.** FTIR spectra of (A), CuO; (B), CuCo-*0*; (C), CuCo-*17*; (D), CuCo-*17* after $N_2$ treatment at 500 °C for 6 h.

The $N_2$ adsorption-desorption isotherms and the pore size distribution curves of the CuCo-*x* catalysts are reported in Fig.3.9. All the samples exhibit a type IV isotherm. The hysteresis loop reveals two relatively well-resolved steps: an H1 loop, indicative of an ordered mesopore system and a feature, observable in the region of high relative pressure, typical of the filling range of textural porosity. Similar results have been reported by other authors for SBA-15-templated $Co_3O_4$[36] and $CuCo_2O_4$ spinel [13]. Surface area, $S_{BET}$, and pore volume, $V_p$, were calculated from the BET equation. The BJH method was applied to the desorption branch of the isotherms to obtain the pore size distribution curves (Fig. 3.9, inset) which appear rather narrow. The textural results are summarized in Table 3.1. The surface area of all the catalysts is very close to 90 $m^2\ g^{-1}$, being not affected by the Cu content. These values are one order of magnitude higher than those (< 10 $m^2\ g^{-1}$) obtained for similar samples prepared by conventional methods [37] and comparable with the values (80-120 $m^2\ g^{-1}$) reported in the literature for mesoporous cobalt and copper-cobalt oxides synthesized by HT method [13-14, 36, 38]. Both the pore volume and the pore size of the CuCo-*x* samples seem unaffected by the Cu loading. The $V_p$ values (0.141-0.184 $cm^3\ g^{-1}$, Table 1) are in agreement with the result (0.167 $cm^3\ g^{-1}$) reported in [38] for a mesoporous silica-templated $Co_3O_4$. The pore size values ($d_p$ = 3.4 - 3.8 nm) are consistent with the pore wall thickness of the parent SBA-15, which seems to suggest that the materials are replicas of the topological structure of the template. This is confirmed by TEM observations: micrographs of the CuCo-*17* catalyst clearly show the ordered rod-like morphology of the material (Fig. 3.4a); at higher magnification (Figs. 3.8 b and c), the shape-reversed moulded structure of the silica template is visible, the channels being void replicas of the former walls of the SBA-15 host and the oxide appearing as rods, of ca. 7 nm in diameter.

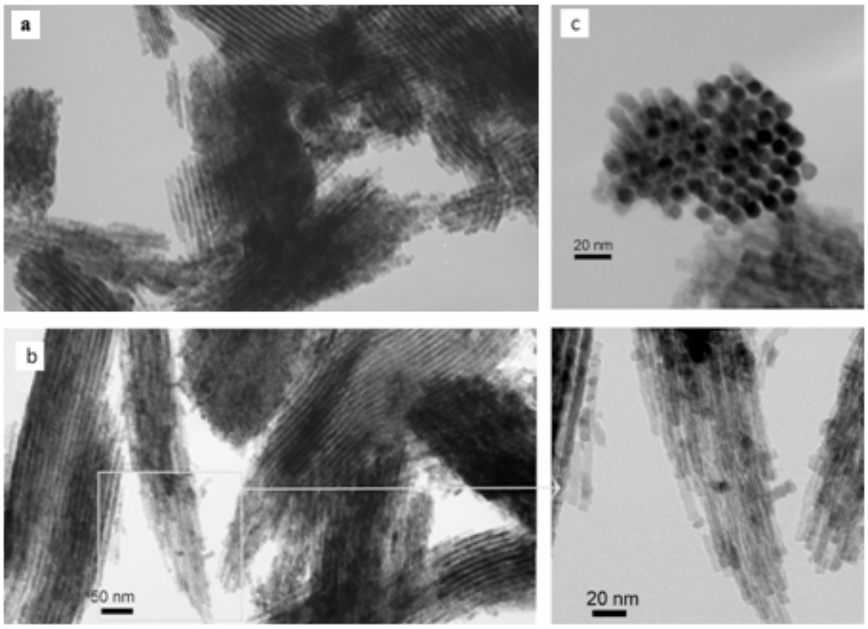


**Figure 3.8.** TEM images of the CuCo-*0* (a) and CuCo-*17* (b, c) catalysts.

**Table 3.1.** Textural properties of the CuCo-*x* catalysts.

| Catalyst | $S_{BET}$ ($m^2 g^{-1}$) | $V_p$ ($cm^3 g^{-1}$) | $d_p$ (nm) |
|---|---|---|---|
| CuCo-*0* | 93 | 0.173 | 3.7 |
| CuCo-*9* | 89 | 0.184 | 3.4 |
| CuCo-*13* | 92 | 0.141 | 3.8 |
| CuCo-*17* | 94 | 0.167 | 3.6 |

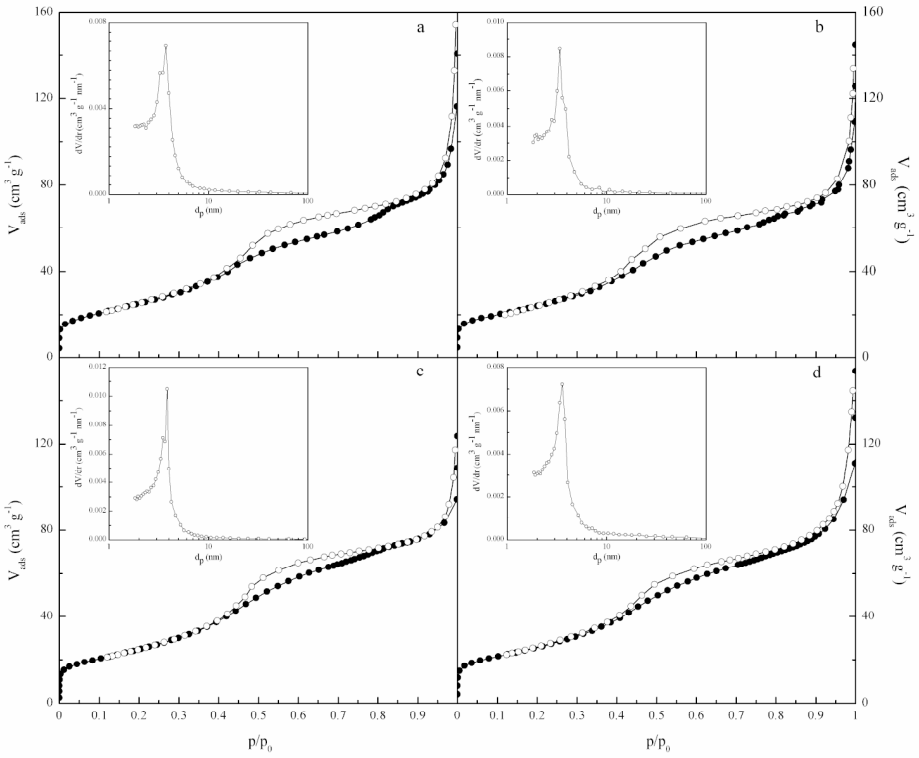


**Figure 3.9**. Nitrogen adsorption/desorption isotherm and pore size distribution plot (inset) of CuCo-*x* catalysts: CuCo-*0*, (a); CuCo-*9*, (b); CuCo-*13*, (c); CuCo-*17*, (d).

$H_2$-TPR results are presented in Fig. 3.10. The reduction profile of pure CuO shows a signal centred at 367 °C. The occurrence of a single-step reduction is in agreement with the literature [39-40], where the reported temperatures of the maximum $H_2$ consumption range from 310 °C to 380 °C, reasonably owing to differences in sample particle sizes and/or experimental conditions. The reduction features of CuCo-*x* samples are more complex. In the reduction behaviour of pure $Co_3O_4$ (CuCo-*0*) two temperature regimes can be individuated: (i) a low-temperature regime, characterized by a relatively well-defined peak centred at 335 °C; (ii) a high-temperature regime, whose main feature is a broad peak with its maximum at 484 °C, showing some heading and a shoulder at 384 °C). The hydrogen consumption associated with regions (i) and (ii) are in the ratio of ca. 1:3. Such two regimes are well-documented in the literature [33, 41-43]. They are generally ascribed to the reduction of $Co_3O_4$ to CoO (Eq.3.1), resulting in the collapsing of the spinel structure, and the reduction of CoO to metallic cobalt (Eq.3.2).

$$Co_3O_4 + H_2 \rightarrow 3\ CoO + H_2O \quad (3.1)$$

$$3\ CoO + 3\ H_2 \rightarrow 3\ Co + 3\ H_2O \quad (3.2)$$

The TPR profiles reported for $Co_3O_4$ by the various authors differ in some minor details: thus, according to [33] both regimes (i) and (ii) are characterized by a single, well-defined peak, whereas in [44] regime (i) appears as a pronounced shoulder of the prominent, markedly asymmetric peak representing regime (ii). Again, in both [42] and [43] one (relatively symmetric) peak is reported in region (ii), and two peaks in region (i), one of them being however very small and located at the low-temperature side of the TPR spectrum. According to [43], the latter can be ascribed to the reduction of surface species. It should be noted that, in general, factors such as particle size and non-uniform composition between surface and bulk (which in turn could be influenced by the preparation method) may well be responsible for the minor differences among the profiles reported by the different authors. Such details are not discussed in the literature, nor will be for the present TPR results. Concerning the reduction profiles of CuCo-*9*, CuCo-*13* and CuCo-*17*, a common feature is their shift towards lower temperatures. Such copper-promoted easier reducibility with respect to the pure $Co_3O_4$ and CuO oxides reveals that a strong interaction occurs between cobalt and copper. It is also worthy of note that the two reduction regimes observed for $Co_3O_4$ can still be singled out in the copper-containing samples. However the two regimes tend to merge in the presence of copper. No further discussion can be attempted, the collapsing of the spinel structure and the further reduction to the metallic state being now complicated by the presence, besides $Co^{2+}$, of $Cu^{2+}$ in the tetrahedral sites and the interaction of both with $Co^{3+}$ in the octahedral holes.

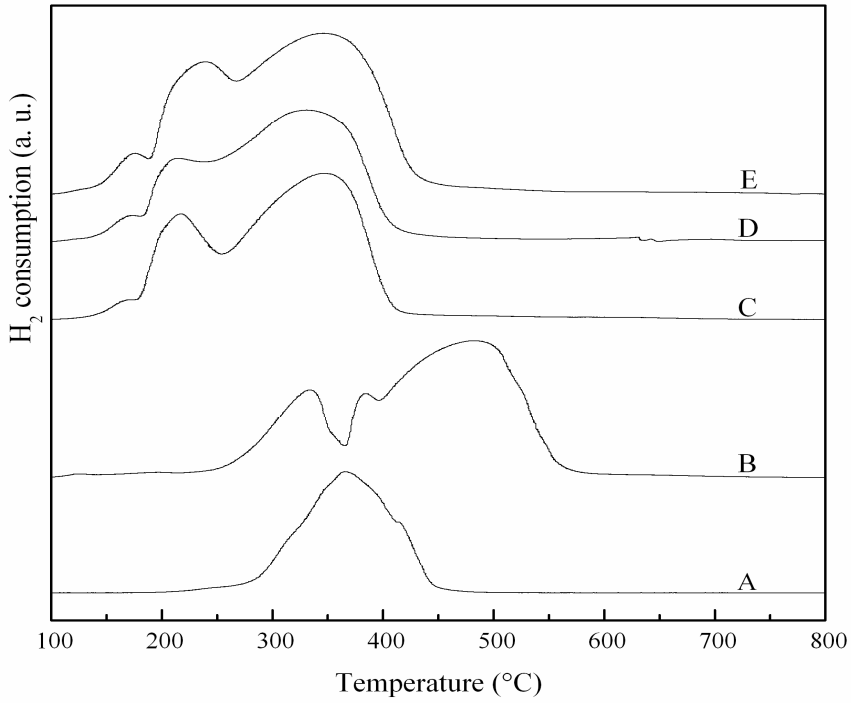


**Figure 3.10**. $H_2$-TPR profiles of (A), CuO; (B), CuCo-*0*; (C), CuCo-*13*; (D), CuCo-*17*.

## 3.4. Catalytic activity of CuCo-*x* catalysts

### *3.4.1. CO oxidation activity in the absence of $H_2$*

Catalytic testing results are shown in Fig. 3.11, where the CO conversion is plotted vs. the reaction temperature. All the catalysts are able to oxidize CO even at 40 °C, though to a very low extent (CO conversion ca. 5 %). Increasing in the temperature up to 80 °C causes a smooth increase in activity, a further, steeper increase being observed, without significant differences between the catalysts, when the temperature is raised beyond this point. For all the samples, the temperature for 50 % conversion ($T_{50}$) is ca. 100 °C. From this point onwards the trend for the pure $Co_3O_4$ oxide differentiates from that of the other samples, which attain 100 % conversion at 140 °C whereas at this same temperature 87 % conversion is reached over $Co_3O_4$. $T_{50}$ values can be used for comparing the performance of the present catalysts with that of $Co_3O_4$ and copper-cobalt oxides previously investigated by other authors. A summary of the literature data is reported in Table 3.2. The superiority

of the present catalysts over a $Co_3O_4$ sample prepared by coprecipitation-oxidation [45] is manifest. At first sight it seems that better results than the present ones have been obtained over copper-cobalt spinels prepared by nitrates calcination [46] ($T_{50}$ = 50 °C), by ultrasonic aerogel pyrolysis [47] (100 % conversion at 52 °C), or by hard template method [13]($T_{50}$ = 70 °C). However, inspection of the reaction conditions shows that the results reported in [10, 46] were obtained with a much higher catalyst amount, a lower flow rate and a higher (for [46]) oxygen concentration; a much higher oxygen concentration, which is known to remarkably promote the catalytic activity of $Co_3O_4$-based catalysts [48], was used in [13]. In view of the sample amount, flow rate and oxygen concentration, the results for the hard-templated $Co_3O_4$ catalyst reported in [11] are comparable to the present ones.

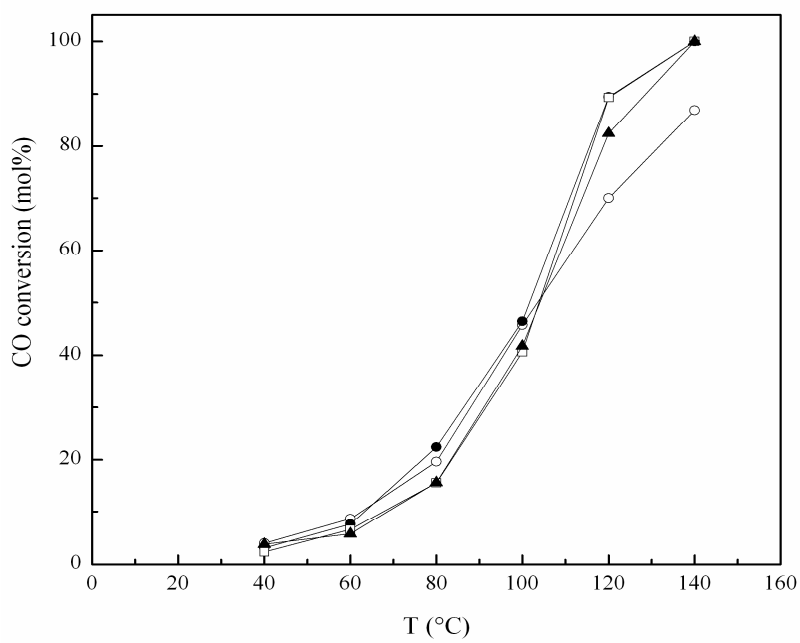


**Figure 3.11**. CO conversion vs. reaction temperature for the CuCo-*x* catalysts in the low temperature CO oxidation: (○), CuCo-*0*; (●), CuCo-*9*; (□) CuCo-*13*; (▲) CuCo-*17*.

**Table 3.2.** Comparison of the experimental conditions used for CO oxidation in the present work with those of literature data.

| Catalyst | Sample weight (m g) | CO (mol%) | $O_2$ (mol%) | Total flow rate ($cm^3$ $min^{-1}$) | $T_{50}$ (°C) | Refs. |
|---|---|---|---|---|---|---|
| $Co_3O_4$ [a] | 50 | 4.0 | 10.0 | 20 | 150 | [14] |
| CuCo spinel [b] | [c] | 5.0 | 20.0 | 15 | 50 | [11] |
| CuCo spinel [d] | 200 | 3.0 | 3.0 | 30 | [e] | [28] |
| $Co_3O_4$ [f] | 16 | 0.5 | 1.0 | 100 | 160 | [49] |
| CuCo spinel [f] | 50 | 1.0 | 20.8 | 100 | 70 | [50] |
| $Co_3O_4$ and CuCo spinel [f] | 30 | 1.5 | 1.5 | 55 | 102 | present work |

[a] Coprecipitation-oxidation method. [b] Nitrates calcination method. [c] 1 $cm^3$ of catalyst (weight not available). [d] Ultrasonic aerogel pyrolisis method. [e] $T_{50}$ not available; 100 % conversion at 325 K. [f] Hard template method.

The influence of the activation treatment of the catalyst prior to the reaction on its performance has been checked on the CuCo-*17* sample. The results are shown in Fig. 3.12. The best performance ($T_{50}$ = ca. 100 °C) is obtained by pretreating the catalyst in air at 500 °C for 1 h. A lower pretreatment temperature (150 °C for 1 h in air) slightly decreases the activity ($T_{50}$ = 110 °C) and a two-step activation procedure (reduction under $H_2$ at 350 °C for 2 h and successive re-oxidation under air flow for 1 h at the same temperature) leads to a poor catalyst ($T_{50}$ = ca. 135 °C). The sensitivity of $Co_3O_4$ to reducing pretreatment conditions (CO- or $H_2$-containing atmosphere) is known [37]. It is ascribed to a drastic change in the $Co^{2+}/Co^{3+}$ balance, the coesistence of $Co^{2+}$ - $Co^{3+}$ pairs in the same material being essential for the catalytic activity. It is worthy of note that the temperature of the first activation step is high enough to allow the accomplishment of the reduction regime (i) (cf. Fig. 3.10), i.e. the collapsing of the spinel structure, and even the establishing, to some extent, of the reduction to the metallic state of the bivalent cations. The catalytic results seem to suggest that the second activation step (under oxidizing conditions) is only partially able to restore the correct ratio between $Co^{3+}$ and the bivalent cobalt and copper ions.

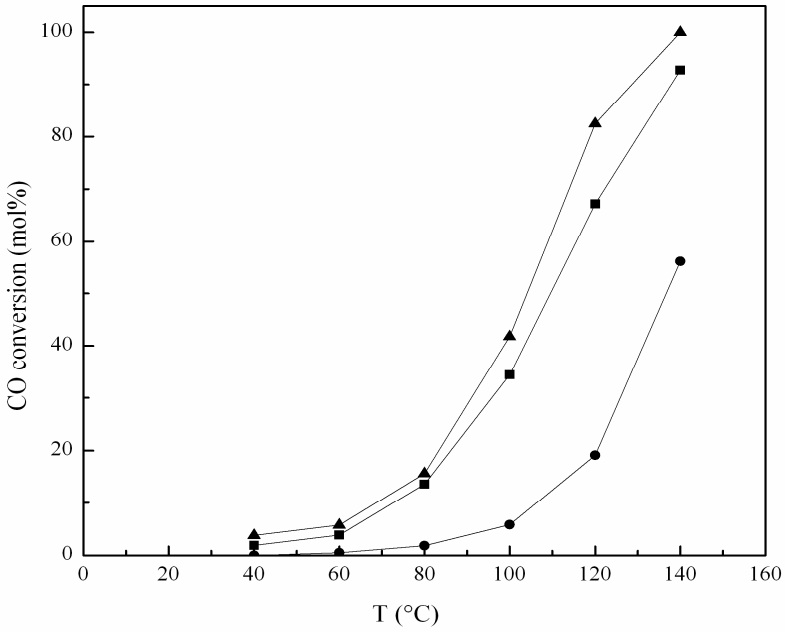


**Figure 3.12**. CO conversion vs. reaction temperature for the CuCo-*17* catalyst in the low temperature CO oxidation: (▲) pretreated under air at 500 °C for 1 h; (■) pretreated under air at 150 °C for 1 h; (●) pretreated under $H_2$ at 350 °C for 2 h and then calcined in air for 1 h at the same temperature.

### *4.4.1. Preferential oxidation of CO (PROX-CO)*

Catalytic results for the CO oxidation in hydrogen-rich atmosphere are presented in Fig. 3.13. For CuCo-*0*, CO conversion (Fig. 3.13a) increases monotonically with the reaction temperature and attains 86 % at 200 °C, whereas for all the Cu-containing catalysts a maximum in the $X_{CO}$ vs. T profile is observed at 160 °C, with CO conversion values of 73-80 %. The temperature for 50 % conversion ($T_{50}$) is ca. 138 °C for CuCo-*0* and decreases to ca. 123-127 °C for the Cu-containing samples, which indicates that the presence of Cu slightly enhances the catalytic activity for CO transformation. The selectivity values in Fig. 3.13b reveal that over CuCo-*0* the reacted CO is completely oxidized to $CO_2$, $S^{CO}_{CO_2}$ being 100 % in the whole range of investigated temperatures. In the case of the Cu-containing catalysts, a decrease in selectivity is observed at the high reaction temperatures (beyond 180 °C over CuCo-*9* and 160 °C over both CuCo-*13* and CuCo-*17*),

which indicates the establishing, besides CO oxidation to $CO_2$, of the methanation reaction (Eq. 3.3).

$$CO + 3\ H_2 \rightleftarrows CH_4 + H_2O \qquad (3.3)$$

At 200 °C ca. 20 % of CO is transformed into $CH_4$ over such catalysts.

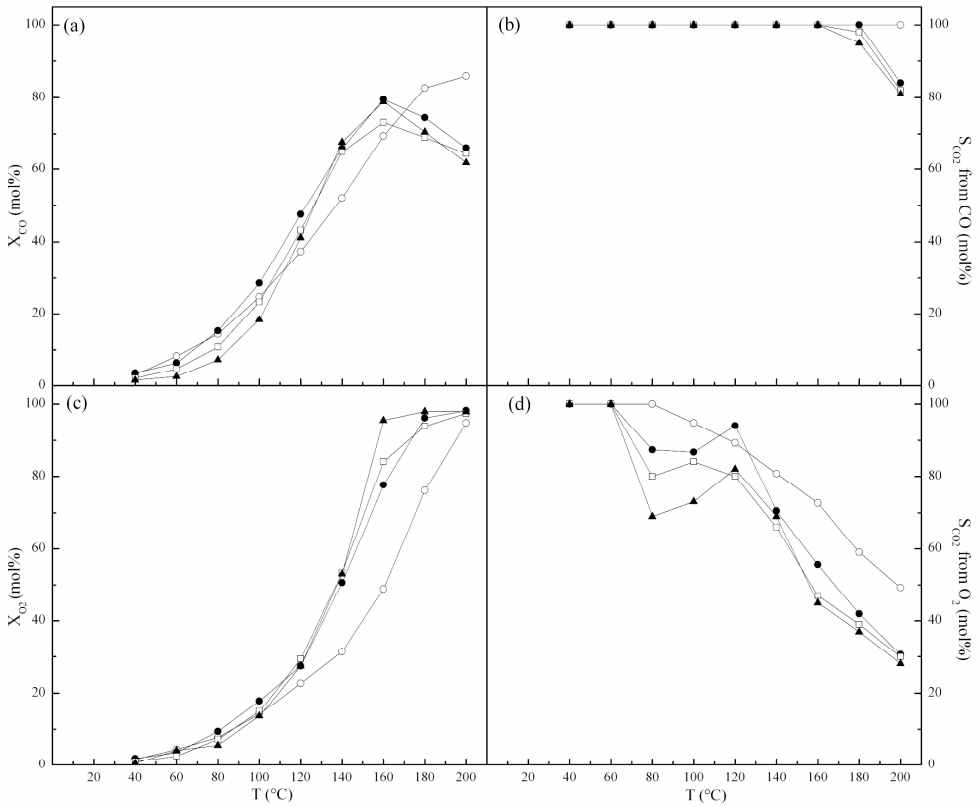


**Figure 3.13**. CO PROX activity vs. reaction temperature for CuCo-*0* (○), CuCo-*9* (●), CuCo-*13* (□), and CuCo-*17* (▲): (a), CO conversion; (b), $CO_2$ selectivity from CO; (c), $O_2$ conversion; (d), $CO_2$ selectivity form $O_2$. Catalyst amount: 0.03 g.

As to the $O_2$ conversion (Fig. 3.13c), a monotonic increase is observed for all the catalysts as the reaction temperature is increased up to 200 °C, $X_{O_2}$ values of 95-98 % being attained at such temperature. Based on the $T_{50}$ values (160 °C for CuCo-*0*, 140 °C for CuCo-*9*, CuCo-*13* and CuCo-*17*), it seems that the oxygen conversion is somewhat favoured by the presence of Cu. As shown by Fig. 3.13d, in the case of CuCo-*0* the oxygen selectivity towards $CO_2$ formation is 100 % for reaction temperatures up to 80 °C; a sharp

decrease is observed beyond this temperature, although 49 % of the reacted oxygen is still converted to $CO_2$ at 200 °C. The presence of Cu in the catalyst results in some worsening of the $O_2$ selectivity towards $CO_2$: regardless of the Cu content, $S_{CO_2}^{O_2}$ remains 100 % only up to 60 °C, being generally well below the value for the pure $Co_3O_4$ when the temperature is increased beyond this point. At variance with the case of CuCo-*0*, for which a monotonic decrease in $S_{CO_2}^{O_2}$ is observed for reaction temperatures above 80 °C, the $S_{CO_2}^{O_2}$ vs. T curves of the Cu-containing catalysts show the presence of a relative minimum, occurring at 100 °C for CuCo-*9* and at 80 °C for both CuCo-*13* and CuCo-*17*. The higher the Cu amount, the deeper the minimum. $S_{CO_2}^{O_2}$ vs. T curves characterized by the presence of a minimum have been observed by several authors [19, 50-51] for both pure and supported $MO_x$-based catalysts (M = Mn, Fe, Ni, Cr, Co, Cu) with different metal compositions; however no comments have appeared so far in the literature regarding this point. Reasons for the presence of such minimum seem difficult to understand and no interpretation will be attempted here.

It is reported in the literature that the catalytic activity of metal oxides in CO conversion can pass through a maximum as the reaction temperature is increased [19, 50-53]. Such a behaviour is also observed on the present Cu-containing catalysts (Fig. 3.13a), and can be ascribed to (i) the different kinetics of the CO and $H_2$ oxidation reactions and/or (ii) the occurrence of the reverse gas shift reaction (RWGS) involving the product $CO_2$ and the reactant hydrogen (Eq.3.4).

$$CO_2 + H_2 \rightleftarrows CO + H_2O \qquad (3.4)$$

Based on literature results showing that no significant RWGS takes place at temperatures ≤ 200 °C over CuO- [53] and $Co_3O_4$-based [54] catalysts, the (ii) possibility can reasonably be ruled out. Concerning point (i), it has been specifically addressed by performing $H_2$ oxidation experiments on CuCo-*0* and CuCo-*17* using a CO-free feed. The $O_2$ conversion values in the hydrogen oxidation are reported as a function of temperature in Figs. 3.14a and b for CuCo-*0* and CuCo-*17*, respectively. For comparison, the $O_2$

conversion values for CO oxidation are also reported in Fig. 3.14, as well as those for the CO PROX. The inherently higher ability of CuCo-*0* in oxidizing CO rather than hydrogen is apparent from the comparison (Fig. 3.14a) between the temperatures for the onset of the former (40 °C) and the latter reaction (80 °C). (Note that this ability in oxidizing CO is maintained even in the presence of large amounts of hydrogen, under which conditions the reaction still sets in at a temperature as low as 40 °C.) Inspection of Fig. 3.14b reveals that for CuCo-*17* the onset of $H_2$ oxidation occurs at 60 °C, i.e. 20 °C below the point at which such reaction is triggered over CuCo-*0*, thus suggesting that the presence of Cu promotes $H_2$ oxidation.

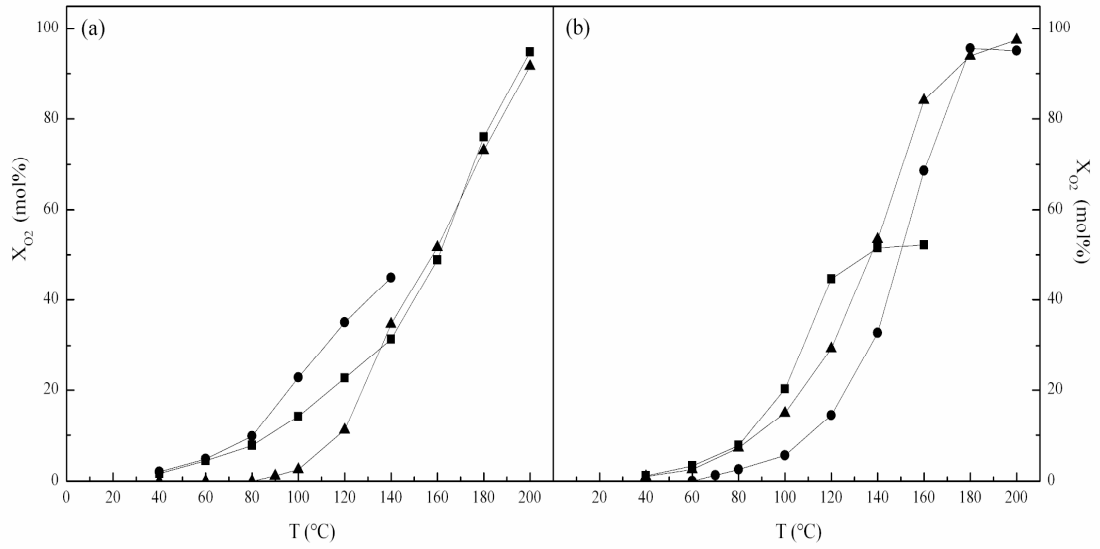


**Figure 3.14.** $O_2$ conversion vs. reaction temperature for CO oxidation (■), $H_2$ oxidation (●), and CO PROX (▲): (a), CuCo-*0*; (b), CuCo-*17*. Catalyst amount: 0.03 g.

Generally speaking, if an increasing amount of oxygen is consumed through the hydrogen combustion rather than through the CO oxidation to $CO_2$, the appearance, after an increasing trend, of a decreasing branch in the $X_{CO}$ vs. T curve should be expected. However this would be actually visible only if the activation energy ($E_a$) values are such that, provided that both the competing reactions have been activated, the reaction temperature is high enough for enhancing more the hydrogen combustion rate than the CO oxidation rate. The apparent $E_a$ value for both hydrogen and CO oxidation has been assessed from the pertinent Arrhenius plots (shown in Fig.3.15), after calculating the

reaction rates by the differential reactor approximation for the runs with oxygen conversion below 20 %. For CuCo-*17*, $E_a$ values of 53 and 45 kJ $mol^{-1}$ were calculated for $H_2$ oxidation and CO oxidation, respectively; a maximum is observed in Fig. 3.13a for this catalyst. The obtained $E_a$ values for $H_2$ oxidation and CO oxidation over CuCo-*0* are 88 and 37 kJ $mol^{-1}$, respectively. The lack of a maximum in the $X_{CO}$ vs. T curve for this catalyst (Fig. 3.13a) would hence stem from the fact that the activation energy for $H_2$ oxidation is too high and the $E_a$ value for CO oxidation so low that, for reaction temperatures below 200 °C, the increase in the rate of the former reaction is lower than the rate enhancement of the latter.

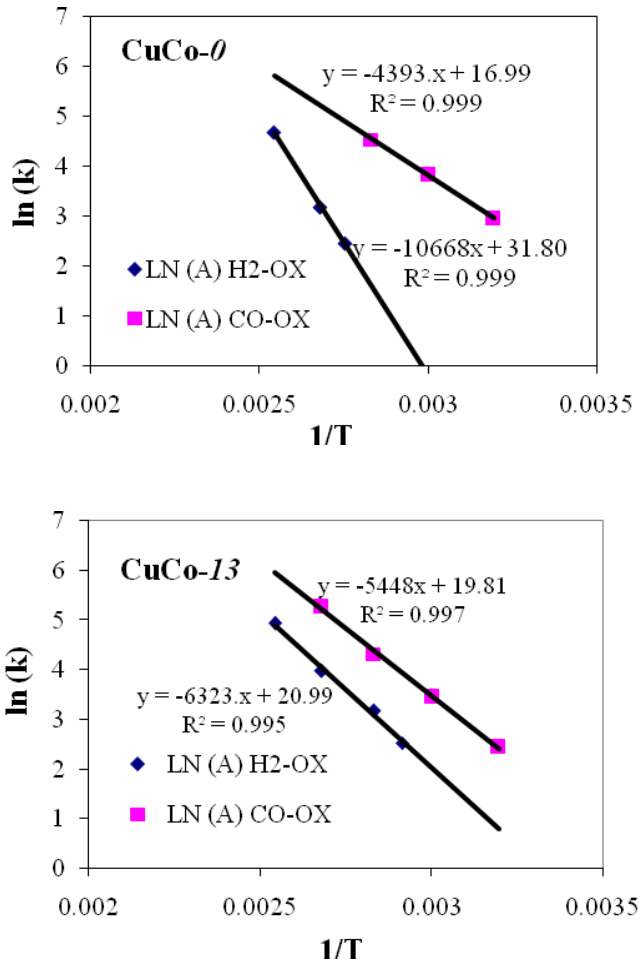


**Figure 3.15.** Arrhenius plot of the specific rate constant of CO oxidation and $H_2$ oxidation over CuCo-*0* and CuCo-*13* catalysts.

It is well known that cobalt is among the most active metals for the methanation reaction [55]. Methanation is observed over the present Cu-containing catalysts, provided that the reaction temperature is high enough: above 180 and 160 °C for CuCo-*9* and both CuCo-*13* and CuCo-*17*, respectively, in high-space velocity runs (Fig. 3.13b. Accordingly, it seems that over these oxides, whose copper-induced easy reducibility is manifest from the TPR experiments, the hydrogen-rich atmosphere of the PROX causes the formation of metallic cobalt, which in turn catalyzes the methanation reaction. By converse, over CuCo-*0*, which - according to the TPR results - requires temperatures well above 200 °C for its reduction, no methanation is observed. The permanent modification undergone by the present Cu-containing catalyst as a consequence of reduction of the oxide to metallic cobalt is apparent from the worsening in their CO PROX performance. This is shown in Fig. 3.16, where 40-200 °C reaction cycles carried out on fresh and regenerated portions of CuCo-*17* are compared. By converse, in the same Fig. 3.16 no differences in the catalytic performance between fresh and regenerated portions of CuCo-*0* are observed, which indicates that no modification of the catalyst has occurred. FTIR experiments on the used samples (Fig. 3.17) definitely confirm that the spinel structure is partially destroyed after the CO PROX reaction in the case of CuCo-*17*, whereas it is preserved in the case of CuCo-*0*.

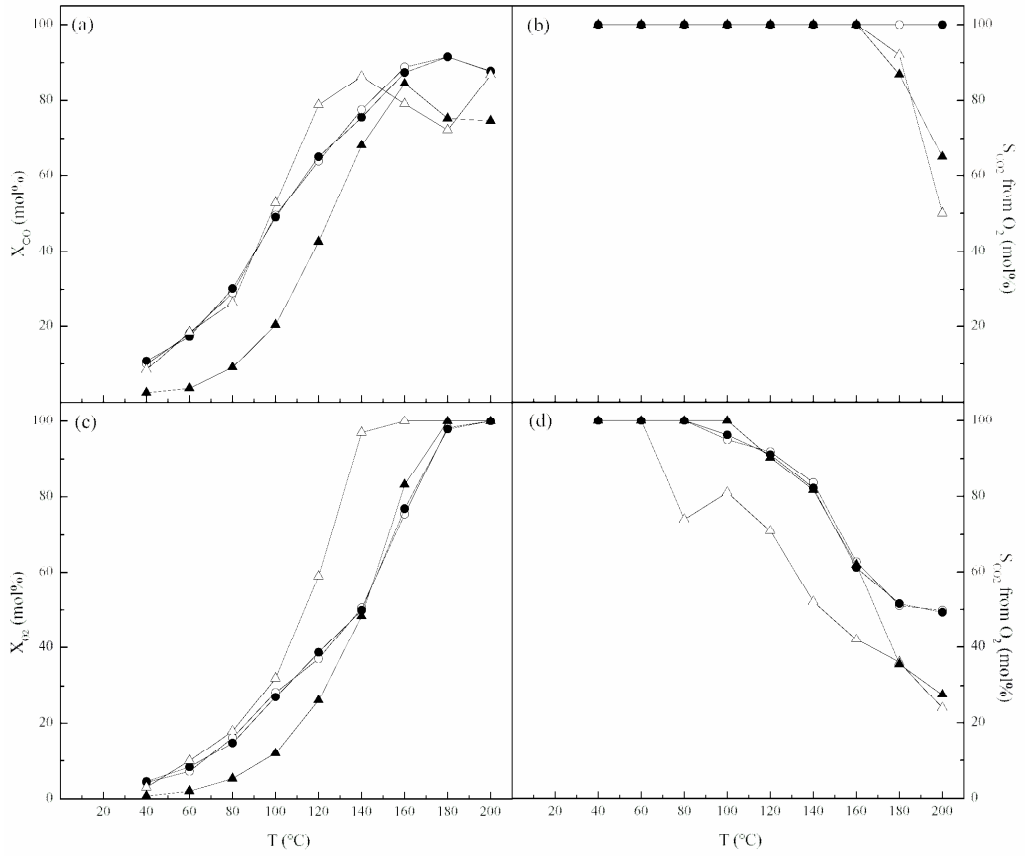


**Figure 3.16**. CO PROX activity vs. reaction temperature for CuCo-*0* (○;●) and (△,▲) CuCo-*17*: (a), CO conversion; (b), $CO_2$ selectivity from CO; (c), $O_2$ conversion; (d), $CO_2$ selectivity form $O_2$. Catalyst amount: 0.1 g. Open and full symbols refer to fresh and regenerated samples, respectively.

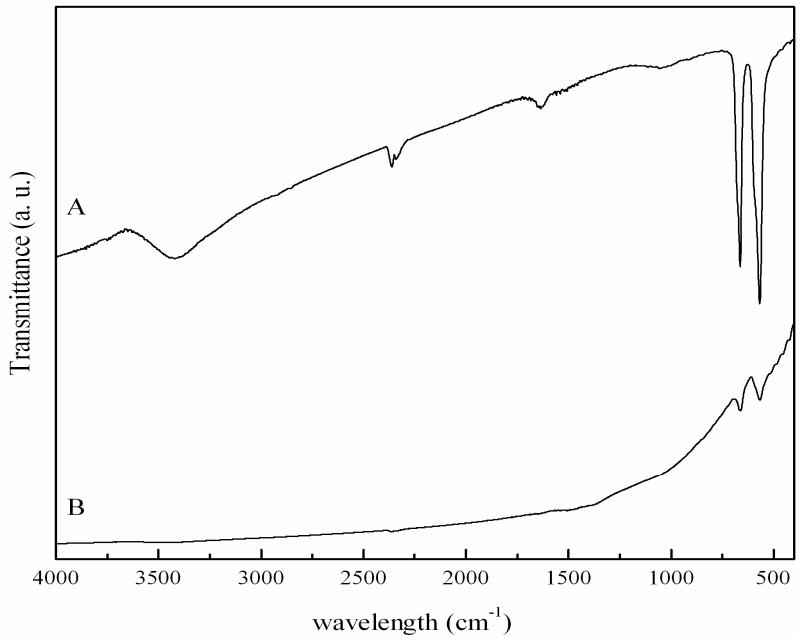


**Figure 3.17.** FTIR spectra of (A), CuCo-*0* and (B), CuCo-*17* catalysts after CO PROX reaction.

## 3.5. Conclusions

Hard-templated, rod-shaped copper-cobalt spinels with appreciably high $S_{BET}$ and $V_p$ values, narrow mesopore distribution, are active catalysts for both CO oxidation and CO PROX reaction. The presence of copper is beneficial in the CO oxidation only at reaction temperatures above ca. 100 °C, which represents the $T_{50}$ for all the catalysts. The activity results are comparable with those reported in the literature for hard-templated samples and seem superior to those for traditionally-prepared catalysts. A reduction-reoxidation pretreatment prior to reaction, probably causing an alteration in the ratio between $Co^{3+}$ and the bivalent cobalt and copper ions, leads to a less active catalyst.

Concerning the CO PROX, the Cu-containing catalysts show increased oxygen ($T_{50}$ = 140 °C) and CO conversion ($T_{50}$ = ca. 123-127 °C) in comparison with pure $Co_3O_4$ ($T_{50}$ = 160 and ca. 138 °C, respectively). The presence of copper however enhances the parasite hydrogen combustion. It also induces the occurrence to some extent of the methanation reaction, provided that the reaction temperature is high enough (≥ 180 or 160 °C, depending on the Cu content). The copper-promoted easier reducibility of the CuCo spinels

in comparison with the pure $Co_3O_4$ oxide (over which methanation does not occur) suggests that methanation is catalyzed by metallic cobalt formed during the PROX run.

## References

[1] J. Hemberger, P. Lunkenheimer, R. Fichtl, H.A. Krug von Nidda, V. Tsurkan, A. Loidl, Nature 434 (2005) 364-367.

[2] H. Jin fan, M. Knez, R. Scholz, K. Nielsch, E. Pippel, D. Hesse, M. Zacharias, U. Gosele, Nat Mater 5 (2006) 627-631.

[3] M. Matsuda, H. Ueda, A. Kikkawa, Y. Tanaka, K. Katsumata, Y. Narumi, T. Inami, Y. Ueda, S.H. Lee, Nat Phys 3 (2007) 397-400.

[4] J.R. Scheffe, J. Li, A.W. Weimer, International Journal of Hydrogen Energy 35 (2010) 3333-3340.

[5] F. Cheng, J. Shen, B. Peng, Y. Pan, Z. Tao, J. Chen, Nat Chem 3 (2011) 79-84.

[6] J.P. Jacobs, A. Maltha, J.G.H. Reintjes, J. Drimal, V. Ponec, H.H. Brongersma, Journal of Catalysis 147 (1994) 294-300.

[7] W.Y. Li, L.N. Xu, J. Chen, Advanced Functional Materials 15 (2005) 851-857.

[8] X. Xie, Y. Li, Z.-Q. Liu, M. Haruta, W. Shen, Nature 458 (2009) 746-749.

[9] K.J. Kim, Y.R. Park, D.H. Hyun, S.H. Lee, Journal of Applied Physics 96 (2004) 1975-1978.

[10] G. Fortunato, H.R. Oswald, A. Reller, Journal of Materials Chemistry 11 (2001) 905-911.

[11] I. Lopes, A. Davidson, C. Thomas, Catalysis Communications 8 (2007) 2105-2109.

[12] Y. Yu, T. Takei, H. Ohashi, H. He, X. Zhang, M. Haruta, Journal of Catalysis 267 (2009) 121-128.

[13] J. Zhu, Q. Gao, Microporous and Mesoporous Materials 124 (2009) 144-152.

[14] Y. Ren, Z. Ma, L. Qian, S. Dai, H. He, P. Bruce, Catalysis Letters 131 (2009) 146-154.

[15] A.A. Mirzaei, R. Habibpour, M. Faizi, E. Kashi, Applied Catalysis A: General 301 (2006) 272-283.

[16] C. Cabet, A.C. Roger, A. Kiennemann, S. Läkamp, G. Pourroy, Journal of Catalysis 173 (1998) 64-73.

[17] H.-K. Lin, C.-B. Wang, H.-C. Chiu, S.-H. Chien, Catalysis Letters 86 (2003) 63-68.

[18] P. Thormählen, E. Fridell, N. Cruise, M. Skoglundh, A. Palmqvist, Applied Catalysis B: Environmental 31 (2001) 1-12.

[19] Z. Zhao, X. Lin, R. Jin, G. Wang, T. Muhammad, Applied Catalysis B: Environmental 115–116 (2012) 53-62.

[20] S. Angelov, D. Mehandjiev, B. Piperov, V. Zarkov, A. Terlecki-Baricˇevic´, D. Jovanovic´, Z. Jovanovic´, Applied Catalysis 16 (1985) 431-437.

[21] U. Chellam, Z.P. Xu, H.C. Zeng, Chemistry of Materials 12 (2000) 650-658.

[22] W. Wei, W. Chen, D.G. Ivey, Chemistry of Materials 20 (2008) 1941-1947.

[23] A. La Rosa-Toro, R. Berenguer, C. Quijada, F. Montilla, E. Morallón, J.L. Vázquez, The Journal of Physical Chemistry B 110 (2006) 24021-24029.

[24] Y. Sharma, N. Sharma, G.V. Subba Rao, B.V.R. Chowdari, Advanced Functional Materials 17 (2007) 2855-2861.

[25] T. Baird, K. C. Campbell, P. J. Holliman, R. W. Hoyle, M. Huxam, D. Stirling, B. Peter Williams, M. Morris, Journal of Materials Chemistry 9 (1999) 599-605.

[26] J.F. Marco, J.R. Gancedo, M. Gracia, J.L. Gautier, R1, amp, x, E. os, F.J. Berry, Journal of Solid State Chemistry 153 (2000) 74-81.

[27] P. Boldrin, A.K. Hebb, A.A. Chaudhry, L. Otley, B. Thiebaut, P. Bishop, J.A. Darr, Industrial & Engineering Chemistry Research 46 (2007) 4830-4838.

[28] D. Zhao, Q. Huo, J. Feng, B.F. Chmelka, G.D. Stucky, Journal of the American Chemical Society 120 (1998) 6024-6036.

[29] E. Xue, M. O'Keeffe, J.R.H. Ross, Catalysis Today 30 (1996) 107-118.

[30] B. Lefez, R. Souchet, K. Kartouni, M. Lenglet, Thin Solid Films 268 (1995) 45-48.

[31] J.L. M. Lenglet, L. Terrier, P. Chartier, J. F. Koenig, P. Nkeng, G. Poillerat, J. Phys. IV France 3 (1993) 477.

[32] S. Li, H. Bi, B. Cui, F. Zhang, Y. Du, X. Jiang, C. Yang, Q. Yu, Y. Zhu, Journal of Applied Physics 95 (2004) 7420-7422.

[33] C.-W. Tang, C.-B. Wang, S.-H. Chien, Thermochimica Acta 473 (2008) 68-73.

[34] F. Boccuzzi, S. Coluccia, G. Ghiotti, C. Morterra, A. Zecchina, The Journal of Physical Chemistry 82 (1978) 1298-1303.

[35] G.-H. Li, L.-Z. Dai, D.-S. Lu, S.-Y. Peng, Journal of Solid State Chemistry 89 (1990) 167-173.

[36] A. Rumplecker, F. Kleitz, E.-L. Salabas, F. Schüth, Chemistry of Materials 19 (2007) 485-496.

[37] D.D. S. Royer, ChemCatChem 3 (2011) 24.

[38] C. Dickinson, W. Zhou, R.P. Hodgkins, Shi, Zhao, He, Chemistry of Materials 18 (2006) 3088-3095.

[39] M.-F. Luo, Y.-J. Zhong, X.-X. Yuan, X.-M. Zheng, Applied Catalysis A: General 162 (1997) 121-131.

[40] A.L. Boyce, S.R. Graville, P.A. Sermon, M.S.W. Vong, Reaction Kinetics and Catalysis Letters 44 (1991) 1-11.

[41] R. Brown, M.E. Cooper, D.A. Whan, Applied Catalysis 3 (1982) 177-186.

[42] B.A. Sexton, A.E. Hughes, T.W. Turney, Journal of Catalysis 97 (1986) 390-406.

[43] L. Xue, C. Zhang, H. He, Y. Teraoka, Applied Catalysis B: Environmental 75 (2007) 167-174.

[44] G. Fierro, M. Lo Jacono, M. Inversi, R. Dragone, P. Porta, Topics in Catalysis 10 (2000) 39-48.

[45] C.-B. Wang, C.-W. Tang, S.-J. Gau, S.-H. Chien, Catalysis Letters 101 (2005) 59-63.

[46] G.N. Pirogova, N.M. Panich, R.I. Korosteleva, Y.V. Tyurkin, Y.V. Voronin, Russian Chemical Bulletin 43 (1994) 1634-1636.

[47] K. Petcharoen, A. Sirivat, Materials Science and Engineering: B 177 (2012) 421-427.

[48] J. Jansson, Journal of Catalysis 194 (2000) 55-60.

[49] N. Bion, F. Epron, M. Moreno, F. Mariño, D. Duprez, Topics in Catalysis 51 (2008) 76-88.

[50] Y. Teng, H. Sakurai, A. Ueda, T. Kobayashi, International Journal of Hydrogen Energy 24 (1999) 355-358.

[51] F. Mariño, C. Descorme, D. Duprez, Applied Catalysis B: Environmental 58 (2005) 175-183.

[52] G. Avgouropoulos, T. Ioannides, H.K. Matralis, J. Batista, S. Hocevar, Catalysis Letters 73 (2001) 33-40.

[53] T. Caputo, R. Pirone, G. Russo, Kinetics and Catalysis 47 (2006) 756-764.

[54] M.P. Woods, P. Gawade, B. Tan, U.S. Ozkan, Applied Catalysis B: Environmental 97 (2010) 28-35.

[55] i.G.C.B. G. R. H. Ross, G. Webb (Eds.), Catalysis, The Royal Society of Chemistry, London, Vol. 7 (198) 13.

CHAPTER

4

# Low temperature CO oxidation and preferential oxidation of CO over $Fe_2O_3$-$Co_3O_4$ binary system

## 4.1. Introduction

Spinels with transition metals have received great research attention in material science field due to its important role in variety of technological applications and heterogeneous processes. Cobalt-containing mixed metal oxide spinels have received special research interest due to its unique physical, chemical and magnetic properties. Cobalt oxide catalyzes wide variety of reactions, however actual nature of the active sites (octahedral versus tetrahedral) is unclear [1]. It is proposed that the catalytic activity and surface properties of the $Co_3O_4$ spinels can be improved by doping its spinel structure with divalent or trivalent metal ions[2-3]. In general, cation distribution of spinels can be explained in terms of cation size, electronegativity and ligand-field effect of transition metals. Iron oxide with $3d^5$ electronic configuration and zero crystal field stabilization energy will be an excellent candidate for doping cobalt spinel. In inverse spinel structure of $Fe_3O_4$, iron can occupy both octahedral and tetrahedral sites [4].Therefore doping cobalt oxide with iron can possibly occupy both tetrahedral and

octahedral sites. Iron doped cobalt oxides are previously prepared with several synthetic route such as, oxidation–precipitation method[5], coprecipitation method[6-8], non-aqueous solution pathway[9] and thermal decomposition method [10]. The catalytic activity of the iron-cobalt systems are investigated for $N_2O$ decomposition [4], Fischer–Tropsch Synthesis[8, 11], catalytic oxidation of phenol[12], catalytic oxidation of cyanides [5], aerobic oxidation of thiols [13] and aqueous phase catalytic oxidation of cyanides [5].

Present work is an effort to investigate the effect of iron doped cobalt oxide for low temperature CO oxidation and preferential oxidation of CO. Hard template method is used to obtain high surface area iron-cobalt spinel. Four catalysts, with 0, 9, 14 and 19 Fe/(Fe+Co) mol%, respectively, were prepared using mesoporous silica SBA-15 as the hard template. They were characterized as to their structure, morphology, texture and redox features by X-ray diffraction (XRD), FTIR spectroscopy, transmission electron microscopy (TEM), $N_2$ physisorption and temperature-programmed reduction with hydrogen ($H_2$-TPR), respectively. Catalytic testing for low temperature CO oxidation and preferential oxidation of CO were carried out in a continuous-flow microreactor operated under atmospheric pressure in the 313- 473 K range.

## 4.2. **Experimental**

### *4.2.1. Materials*

Tetraethylorthosilicate (TEOS, 98%), Pluronic copolymer P123 ($EO_{20}PO_{70}EO_{20}$), $Co(NO_3)_2$. $6H_2O$, $Fe(NO_3)_3$. $9H_2O$, NaOH were supplied by Aldrich. $HAuCl_4$ (Au ≥ 49%) and ethanol (96%) was supplied by Fluka. HCl (37%) was provided by Merck. All the materials were reagent grade.

### *4.2.2. Synthesis of mesoporous silica SBA-15*

Mesoporous silica SBA-15 was prepared under hydrothermal conditions according to [14]. In a typical synthesis, 4 g of Pluronic 123 were added to 120 g of HCl (2M) and 30 g of bi-distilled water. After 15 h under stirring at 308 K, 8.5 g of TEOS were added and the solution was maintained at 308 K for 24 h under stirring. The resulting gel was then transferred into a stainless-steel autoclave and kept at 373 K for 24 h under static conditions. The obtained suspension was filtered and the recovered solid was washed with de-ionized water, dried at 313 K overnight and finally calcined in air at 823 K for

5 h.

*4.2.3. Synthesis of mesoporous iron-cobalt mixed oxides*

Iron-cobalt spinels were prepared by a hard template pathway using SBA-15 as the hard template. In a typical synthesis, $Co(NO_3)_2$ and $Fe(NO_3)_3$, in appropriate amounts to obtain the desired Fe/(Co+Fe) molar ratio, were dissolved in 25 $cm^3$ of ethanol. 1 g of SBA-15 was then added to 15 $cm^3$ of the obtained solution and the suspension was stirred at room temperature for 1 h. Next, the solvent was evaporated at 333 K overnight and the impregnation step was then repeated with the aim of completely filling the SBA-15 pores. The resulting solid was subsequently transferred in a furnace and kept at 823 K for 3 h to decompose the nitrates into oxides. Removal of the SBA-15 template was then performed by leaching with 2M NaOH at 323 K. Finally, the resulting material was

washed up to pH 7 with distilled water and dried at 323 K for 12 h. The obtained samples were named FeCo-*x*, where *x* (= 0, 9, 14, 19) represents the actual Fe/(Co+Fe) molar ratio%.

*4.2.4. Gold deposition on $Fe_2O_3$- $Co_3O_4$ support*

Gold deposition was carried out using deposition precipitation method (DP), as reported by Haruta et-al[15]. In a typical synthesis desired amount of $HAuCl_4$ solution added drop-wise into a slurry containing FeCo-14 support under constant stirring at 60°C. pH of the slurry maintained at 9 by the use of aqueous ammonia solution. After aging for 2 h, the material filtered, washed several times with warm distilled water and then dried at 100°C. Finally calcined under air at 300°C for 2h at a heating rate of 2°C $min^{-1}$. The material after preparation was named as *x*Au/FeCo-14, where *x* represents the amount of gold on the support and it was analysed with ICP and was observed to be 2.4 wt%. Hereafter it will be named as 2.4Au/FeCo-14.

*4.2.5. Catalyst characterization*

Inductively coupled plasma atomic emission spectroscopy (ICP-AES) analyses were performed with a Varian Liberty 200 spectrophotometer to determine the Au content. Samples (15 mg) were dissolved in aqua regia diluted to 100 ml with bi-distilled water.

Structural characteristics of the samples were obtained by XRD using a Seifert diffractometer with 0-0 Bragg Brentano geometry with Cu Kα wavelength. The mean crystallite size was calculated by the Scherrer equation.

The absorption spectra in the medium IR region (4000-400 $cm^{-1}$) were collected using an Equinox 55 (Bruker) spectrophotometer. Pellets of the samples were prepared by dispersing the finely ground powders in KBr.

Transmission electron microscopy (TEM) images were obtained on a JEOL 200CX microscope equipped with a tungsten cathode operating at 200 kV. Finely ground CuCo samples were dispersed in n-octane by sonication, dropped on a carbon-coated copper grid, and dried for observation.

Textural analysis were carried out on a Sorptomatic 1990 System (Fisons Instruments), by determining the nitrogen adsorption/desorption isotherms at 77K. Before analysis, the sample were heated overnight under vacuum up to 523K (heating rate =1K$min^{-1}$).

*4.2.6. Catalytic runs*

CO oxidation in the absence of hydrogen and in a hydrogen-rich stream (CO PROX) were carried out under atmospheric pressure in a quartz-glass fixed-bed continuous-flow microreactor in the 40-140 °C and 40-200 °C temperature range, respectively. The catalyst (0.03 g) was contacted with either a $CO/O_2$ mixture (total flow, 55 $cm^3$ $min^{-1}$; 1.5 vol% CO, 1.5 vol% $O_2$, balance He) or a $CO/O_2/H_2$ stream (total flow, 55 $cm^3$ $min^{-1}$; 1.5 vol% CO, 1.5 vol% $O_2$, 46 vol% $H_2$, balance He). On-line analysis of the reactor effluent was performed on a HP 6890 GC, equipped with a HP Poraplot Q capillary column and both TCD and FID (coupled with a methanator) detectors. At each reaction temperature, samples were collected after 30 min on-stream to allow the attainment of steady-state conditions. Prior to the reaction the catalysts were pretreated in air (15 $cm^3$ $min^{-1}$) at 500 °C (heating rate, 1 °C $min^{-1}$) for 1 h for FeCo-*x* catalysts and 300°C for 2 h for gold deposited catalyst. Conversion and selectivity towards $CO_2$ have been calculated for both CO ($X_{CO}$; $S_{CO_2}^{CO}$) and $O_2$ ($X_{O_2}$; $S_{CO_2}^{O_2}$) by the following equations:

$$X_{CO}\ (\text{mol}\%) = \frac{[CO]_{in} - [CO]_{out}}{[CO]_{in}} \cdot 100; \qquad S^{CO}_{CO_2}\ (\text{mol}\%) = \frac{[CO_2]_{out}}{[CO]_{in} - [CO]_{out}} \cdot 100$$

$$X_{O_2}\ (\text{mol}\%) = \frac{[O_2]_{in} - [O_2]_{out}}{[O_2]_{in}} \cdot 100; \qquad S^{O_2}_{CO_2}\ (\text{mol}\%) = \frac{0.5 \cdot [CO_2]_{out}}{[O_2]_{in} - [O_2]_{out}} \cdot 100$$

where terms in brackets are the inlet and outlet concentrations.

## 4.3. Results and discussions

### *4.3.1. Characterisation of SBA-15*

The low angle X-ray diffraction pattern of SBA-15 in Fig.4.1 shows three well-resolved peaks which can be indexed as the (1 0 0), (1 1 0), and (2 2 0) reflections associated with a hexagonal symmetry. These results are in agreement with the presence of a two-dimensional hexagonal *P6mm* structure with a large unit-cell parameter and indicate that the structure is actually representative of a long-range order. The internal architecture of SBA-15 is clearly visible in the TEM images shown in Fig.4.2: both the viewing directions, parallel (Fig. 2a) and perpendicular (Fig. 2b) to the main axis of the pores, confirm the highly ordered 2-D hexagonal regularity. The ordered arrays of silica channels have a mean diameter of *ca.* 6-7 nm with a wall thickness of about 3 nm.

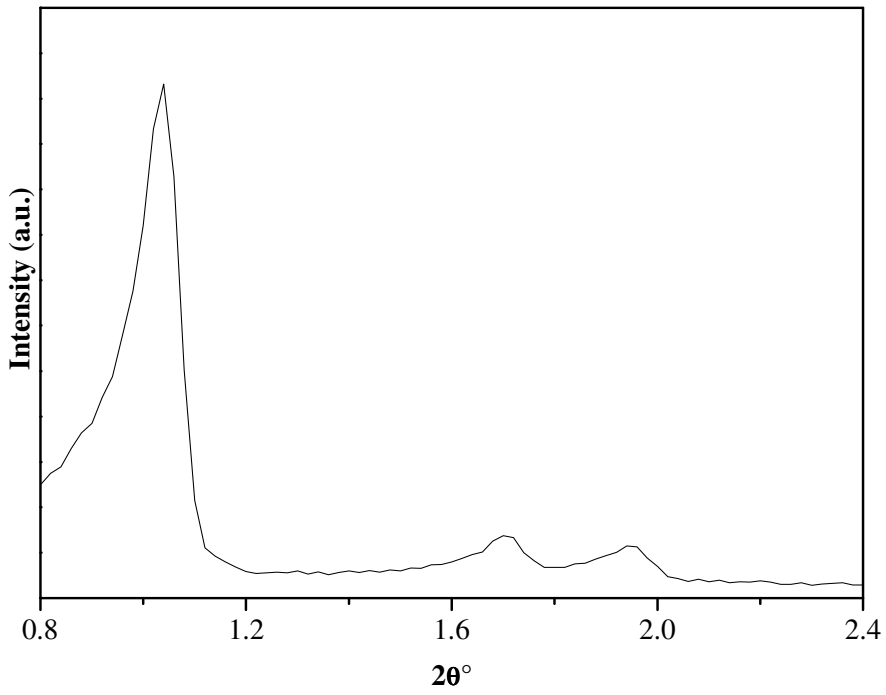


**Figure 4.1.** Low angle XRD diffraction of SBA-15 silica template

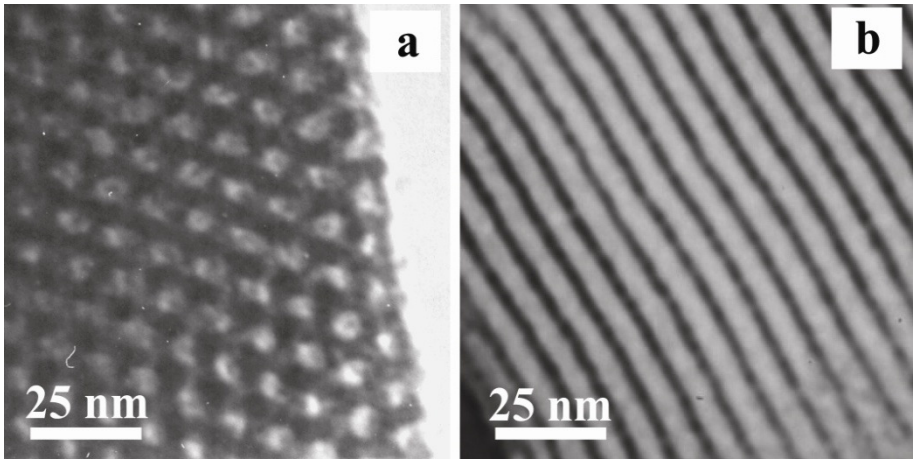


**Figure 4.2**. TEM of SBA-15 silica template

Nitrogen adsorption-desorption isotherm and pore size distribution (insight) of the SBA-15 template is reported in Fig.4.3. The isotherm can be classified as type IV and exhibits an H1-type hysteresis loop at high relative pressure, which are typical features for cylindrical channel mesoporous materials. Multipoint BET specific surface area was calculated from the adsorption branch of the isotherm ($p/p_o$= 0.05–0.25) and equals to 1003.37 $m^2/g$. Pore size distribution of the SBA-15 silica template calculated by Barrett–Joyner–Halenda (BJH) method. A vast majority of pores falls between 4.45 and 7.41 nm, with a maximum at 6.6 nm (insight Fig.2). Total pore volume of the SBA-15 silica was determined from the adsorption branch of the $N_2$ isotherm curve at the ($P/P_0$) = 0.9975 signal point at STP and it was found to be 1.70 $cm^3/g$.

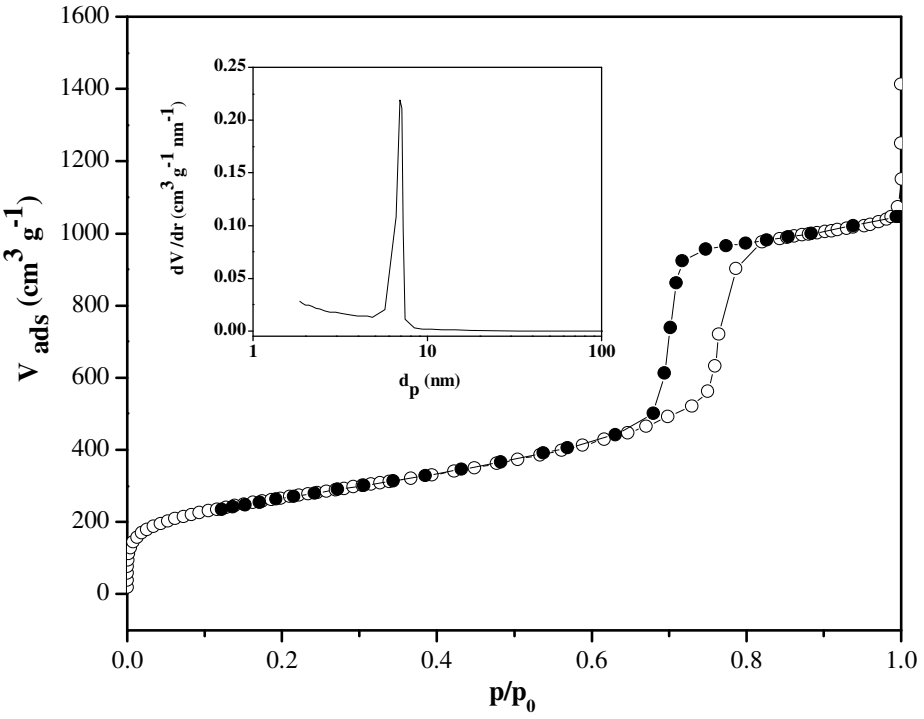


**Figure 4.3.** Nitrogen adsorption-desorption isotherm and pore size distribution (insight) of SBA-15 silica template.

4.3.2. *Characterization of the FeCo-x catalysts*

X-ray diffraction patterns of cobalt oxide and iron doped cobalt oxides are reported in Fig.4.4. The pure crystalline spinel phase was observed with diffraction peaks at 2θ values around 31.4°, 37.1°, 38.6°, 44.9°, 55.9°, 59.5° and 65.3° for the crystal planes (220), (311), (222), (400), (422), (511), and (440), respectively[16]. All the catalysts exhibit the diffraction patterns typical of the cubic spinel phase (space group F*d*-3*m*) of cobalt oxide. However, increasing iron content to 14 and 19 mol% results the formation of magnetite phase at 2θ - 35.5°, 62.6° for the crystal planes (311) and (440), former is the highly intense peak of $Fe_3O_4$ spinel [17], which is clearly visible in the diffraction patterns of FeCo-*14* and FeCo-*19* in Fig.4.4. These results suggest that the FeCo-*14* and *19* systems possess a cobalt rich bi-spinel phase. These types of bi-spinel phase is previously reported for FeCo systems in [7]. In FeCo-9, no peak corresponding to Fe or Fe containing spinel phase is detected, this might be due to the mutual sharing of octahedral sites of the cubic spinel with $Fe^{3+}$ and $Co^{3+}$ [7] or due to the high dispersion of Fe on Co. X-ray diffraction of gold deposited FeCo-*14* are

amorphous, no diffraction peak corresponding to gold are visible in the XRD pattern in Fig.4.4E.

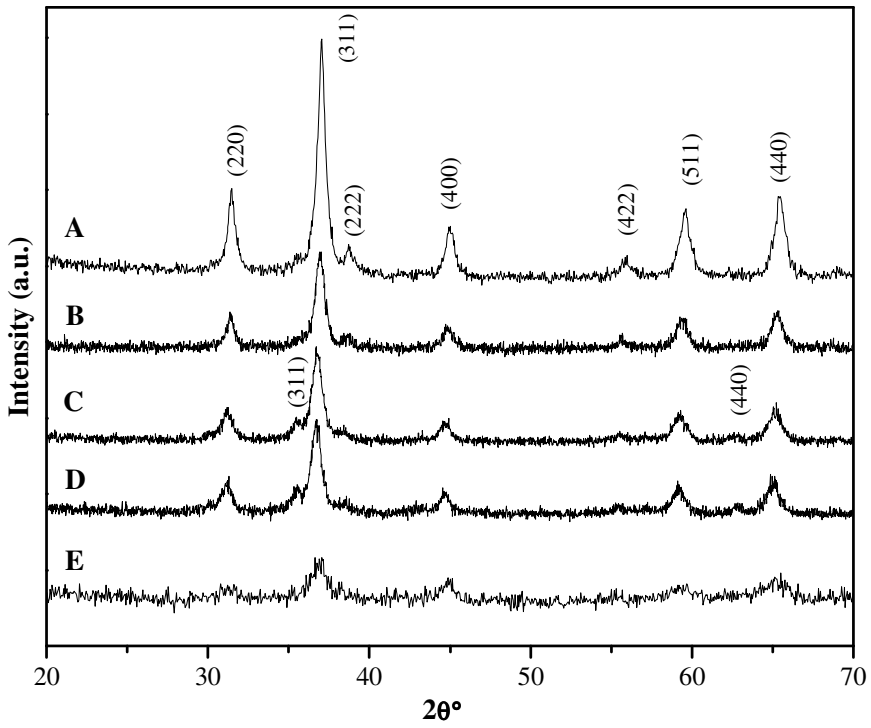


**Figure 4.4.** XRD patterns of FeCo-*x* catalysts: (A), FeCo-0; (B), *FeCo-9*; (C), *FeCo-14*; (D), *FeCo-19*; (E), *2.4Au/FeCo-14*.

TEM images of the FeCo-*x* catalysts are reported in Fig.4.5. FeCo-0 show a nano-rod like structure which resembles structural characteristics of the template SBA-15 reported in Fig.4.2. Partial structural disorder is visible in FeCo-*9*, *14* and *19*, which is also consistent with the adsorption-desorption isotherm and pore size distribution analysis reported in Fig.4.8.

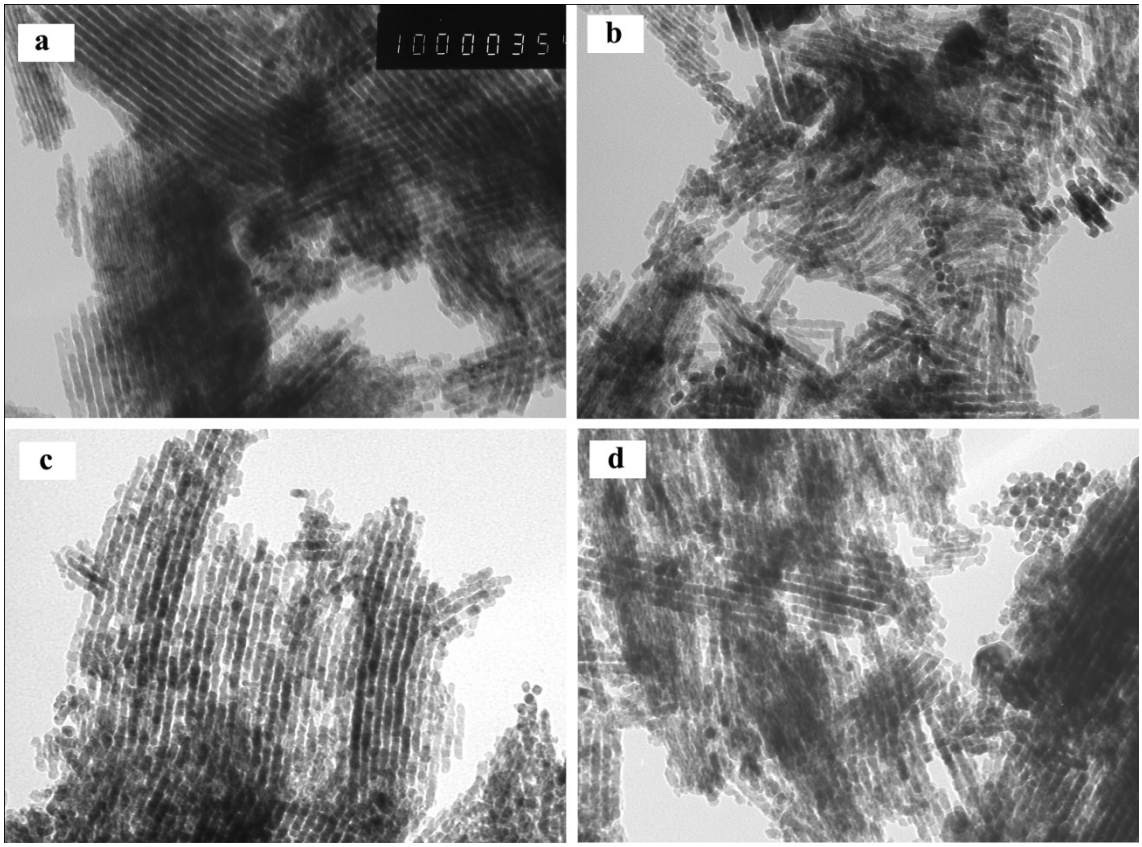


**Figure 4.5.** TEM of FeCo-*x* catalysts: (a), FeCo-0; (b), *FeCo-9*; (c), *FeCo-14*; (d), *FeCo-19*.

FT-IR spectra of the as synthesized FeCo-*x* systems are reported in Fig.4.5. All the FeCo-*x* systems showed similar type spectra at wave numbers 400-4000 $cm^{-1}$. According to literature [18-19], $Co_3O_4$ spinel is characterized by spectral bands in the region 660-650 $cm^{-1}$ and 568-550 $cm^{-1}$ corresponding to the stretching vibrations of metal- oxygen bonds from the tetrahedral and octahedral sites, respectively. For $Fe_3O_4$ spinel, the characteristics stretching vibration of Fe-O bond is at 580 $cm^{-1}$ [20]. The spectral bands in the range 500-700 $cm^{-1}$ in FeCo systems are characteristics of the stretching vibration of cobalt spinel. The bands at 990 $cm^{-1}$, 1635 $cm^{-1}$ and 3430 $cm^{-1}$ are due to (ν–Si-OH), (δ–$H_2O$) and (ν-$H_2O$), respectively [21]. This suggest the presence of very low residual amounts of silica remain in the materials after leaching process. There is no difference observed for the FTIR of gold deposited FeCo-14 catalyst. The FT-IR spectral bands observed in FeCo-*9*, *14* and *19* are in lower frequency range compared to FeCo-*0*. This suggest that the contribution of Fe in the spinel systems (selected regions of the spectra, ie, 500-750 $cm^{-1}$ are reported in Fig.4.6) influences the mobility of the reactive surface oxygen, thereby decreases the surface

metal-oxygen bond strength and shifting the band to lower frequencies (from 567 $cm^{-1}$ to 562, 562, 561 $cm^{-1}$ in FeCo-9, 14 and 19, respectively). It is clear from the figure that the spectral bands are broader in FeCo systems compared to pure cobalt oxide spectral bands, the behavior is observed previously in FeCo spinel [22]. The broadening of the bands are due to the contribution of the stretching vibration of the Fe-O bond at 580 $cm^{-1}$.

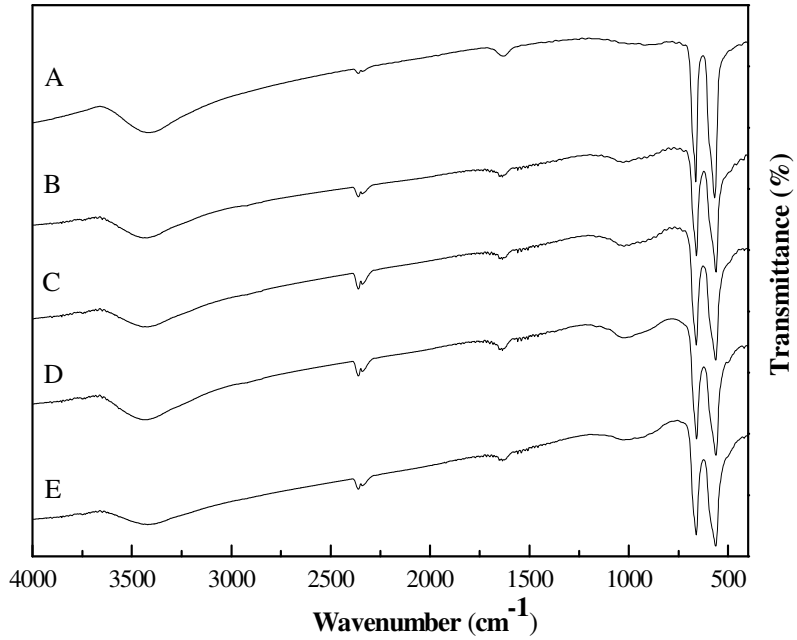


**Figure 4.6.** FTIR spectra of FeCo-*x* catalysts: (A), FeCo-*0* (B), FeCo-9; (C), FeCo-*14*; (D), FeCo-*19*; (E) 2.4 Au/FeCo-14

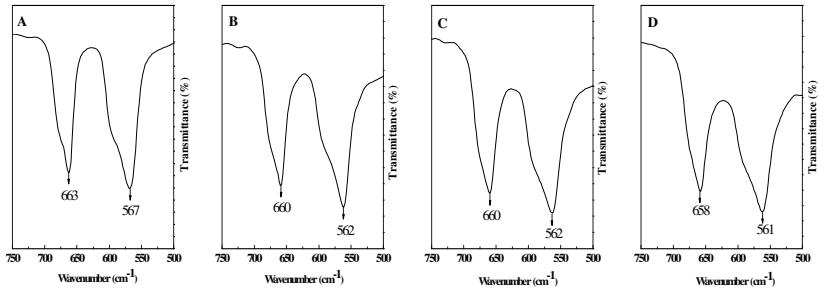


**Figure 4.7.** FTIR spectra of selected regions of FeCo-*x* catalysts: (A), FeCo-*0;* (B), FeCo-9; (C), FeCo-*14*; (D), FeCo-*19*

$N_2$- adsorption-desorption isotherm and pore size distribution (insets) of FeCo-*x* spinel systems are shown in Fig.4.6. All the samples exhibit a type IV isotherm. The isotherm of FeCo-*x* systems showed characteristics behavior of the mesoporous

materials replicated from SBA-15 [23-24]. Pore size distribution (Fig.6 insets) of the FeCo-0 are narrow and centred at 3.7 nm (Table 4.1). The pore size distributions of the FeCo-*9*, *14* and *19* spinel sytems are not regular, this might be due to the partial structural collapse of the material during the leaching process. The calculated values of $d_p$, $v_p$ and $S_{BET}$ are reported in Table.1. All the materials possess high surface area (88 - 133 $m^2/g$) and pore volume, which is not affected by the iron loading. The $d_p$ values (3.1 - 3.7 nm) are in fair agreement with the wall thickness of the silica template SBA-15.

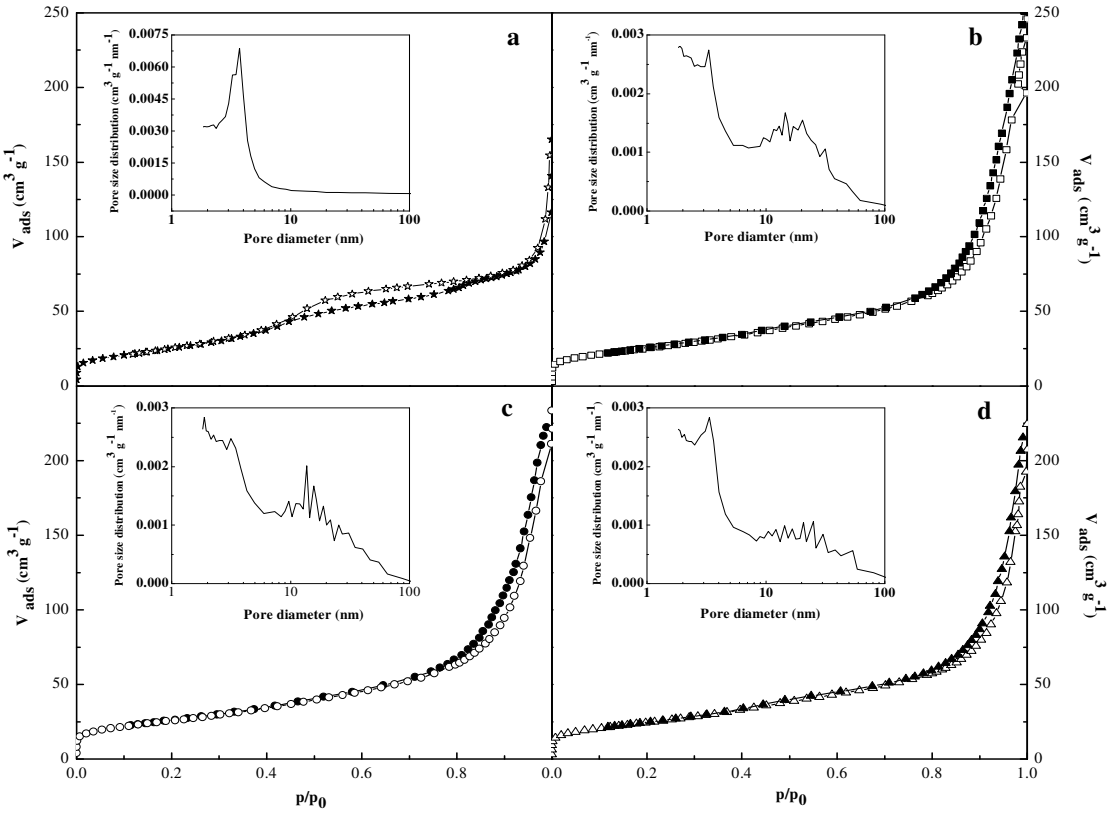


**Figure 4.8.** $N_2$ adsorption-desorption isotherm and pore size distribution (insight) of (a) FeCo-0, (b) FeCo-*9*, (c) FeCo-*14* and (d) FeCo-*19* catalysts.

**Table 4.1.** Textural properties of the FeCo-*x* catalysts

| Catalysts | $S_{BET}$ ($m^2/g$) | Vp ($cm^3/g$) | dp (nm) |
|---|---|---|---|
| SBA-15 | 1003 | 1.70 | 6.6 |
| FeCo-0 | 93 | 0.15 | 3.7 |
| FeCo-9 | 93 | 0.27 | 3.4 |
| FeCo-14 | 93 | 0.28 | 3.1 |
| FeCo-19 | 88 | 0.28 | 3.4 |
| 2.4Au/FeCo-14 | 133 | 0.46 | 3.2 |

To investigate the reduction behavior of FeCo-*x* systems, temperature programmed reduction analysis were carried out. TPR profile of cobalt oxide and iron doped cobalt oxides are reported in Fig 4.6. Pure cobalt oxide showed three well defined peaks between 250 and 600°C is due to the step wise reduction of $Co_3O_4$ to CoO followed by Co°, similar type reduction profile reported for cobalt oxide in [25]. According to literature, $Fe_2O_3$ showed a sharp reduction peaks at 360°C corresponding to the reduction of $Fe_2O_3$ to $Fe_3O_4$ and a broad peak at 680°C is due to the subsequent reduction of $Fe_3O_4$ to Fe° [26-27].The reduction profile of FeCo systems are more complex, It shows three reduction peaks including some shoulders peaks between 280 to 750°C. The reduction peaks at 375 and 664 in FeCo-*9* corresponds to the sequential reduction of $Fe_2O_3$ to $Fe_3O_4$ followed by Fe°. The shoulder at 477°C is assigned to the reduction of $Co_3O_4$ to Co°[26]. FeCo-*14* and *19* reduction profiles resembles that of the FeCo-9, but the increase of Fe concentration causes a shift of the peak maxima to higher temperatures and slight broadening of the peaks, this is in fair agreement with the previous report [28].

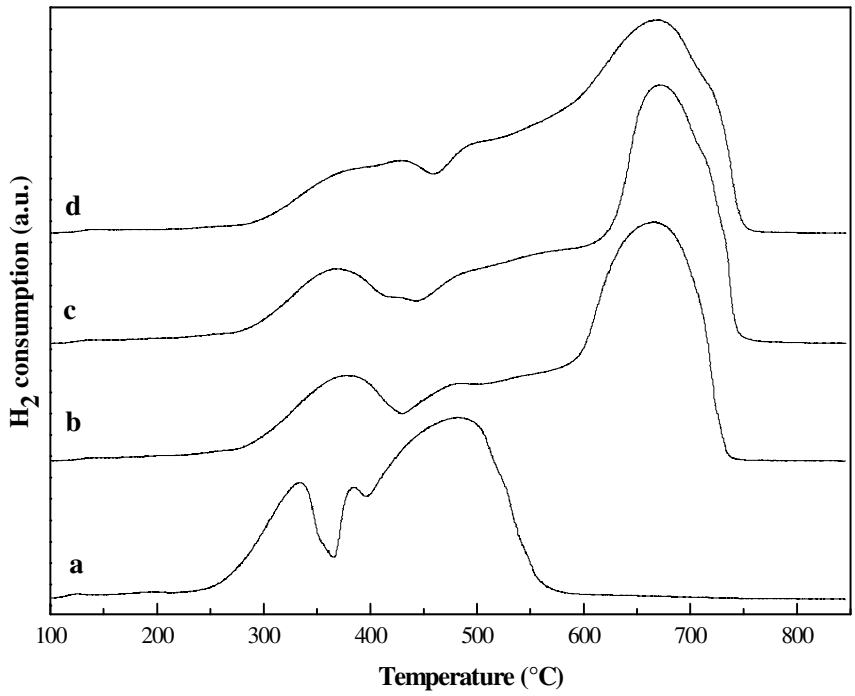


**Figure 4.9.** $H_2$-TPR of FeCo-*x* catalysts: FeCo-*0*, (a); FeCo-*9*, (b); FeCo-*14* (c); FeCo-*19* (d).

## 4.4. Catalytic activity of FeCo-*x* catalysts

### *4.4.1. CO oxidation activity in the absence of $H_2$*

CO oxidation activity of the FeCo-*x* catalysts in the absence of hydrogen are reported in Fig.4.7, where CO conversion plotted against reaction temperature. All the catalysts are found to be active for the reaction at 40-200°C. Pure cobalt oxide spinel (FeCo-0) shows superior activity in oxidizing CO followed by FeCo-*9*, *14*, and *19* for low temperature CO oxidation. At low temperature region 40-80°C, FeCo-*14* show better activity compared to pure cobalt oxide catalyst, beyond this point cobalt oxide showed better activity. All the catalysts showed steep increase in the catalytic activity with an increase of the reaction temperatures until it reaches maximum activity. FeCo-*0* show complete oxidation activity at 140°C, whereas at this temperature 77, 80 and 50% conversion observed over FeCo-*9*, FeCo-*14* and FeCo-*19*, respectively. The temperature for 50% CO conversion ($T_{50}$) is occurred at 101, 116, 112 and 140°C for FeCo-0, FeCo-9, FeCo-14, and FeCo-19, respectively. To improve the catalytic activity of the FeCo spinel system, 2.4 wt% of gold deposited FeCo-14 system. The catalytic activity of the catalysts is reported in Fig.4.7. It is clear from the figure that gold promotes the the CO

oxidation activity of the FeCo-*14* to lower temperatures. At 40°C this catalyst show around 60% CO conversion and at 120° it completely oxidize CO. $T_{50}$ of this catalyst is below 40°C.

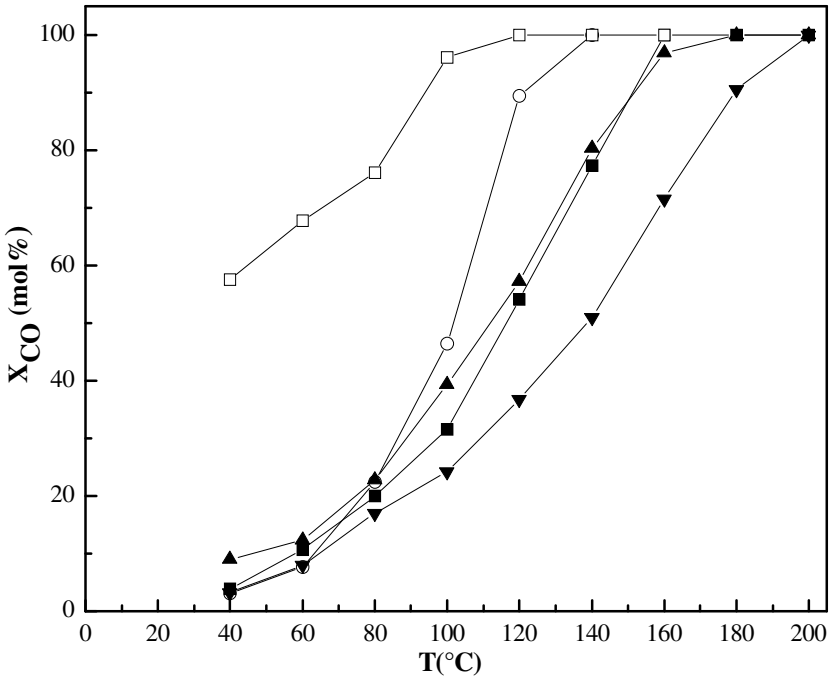


**Figure 4.10**. CO conversion *vs.* reaction temperature of the FeCo-*x* catalysts: (□) 2.4 Au/FeCo-14; (○) FeCo-*0*; (■) FeCo-9; (▲) FeCo-*14*; (▼) FeCo-*19*.

### *4.4.2. Preferential oxidation of CO (PROX-CO)*

CO oxidation activity in the presence of excess hydrogen in investigated over FeCo-*x* catalysts, the activity of the catalysts is reported in Fig.4.8 . For FeCo-*0*, CO conversion (Fig.4.8a) increases with increasing reaction temperature and reaches its maximum of 86% at 200°C. At the same time Fe substituted catalysts shows a maximum conversion of 70-77% conversion. Addition of Fe to the cobalt spinel shows a decrease in the CO oxidation activity. It is reported that the partial substitution of $Co^{3+}$ in the octahedral sites of the cobalt spinel with $Fe^{3+}$ reduces the catalytic activity, because Co3+ is the active site for CO oxidation reaction [29]. However, the CO conversion activity of Fe containing spinels (FeCo-9 and FeCo-14) reported in Fig.4.8a shows improved activity in the low temperature range (40-100°C) compared to FeCo-*0*. FeCo-*9* and *14* shows a CO conversion of 22% at 80°C whereas at the same temperature 14% conversion observed over FeCo-*0*. Gold deposited catalysts show superior activity till 120°C, beyond this point no further improvement observed over this catalyst.

Temperature for 50% CO conversion ($T_{50}$) occurred at 143, 152, 160, 167°C for FeCo-*0*, *9*,*14* and *19*, respectively. Gold deposited catalysts does not reach 50% CO conversion, it completely lost its activity for CO oxidation in presence of hydrogen. The $CO_2$ selectivity from CO for FeCo-x catalysts are shown in Fig.8.4, all the catalysts possess 100% selectivity to $CO_2$. This reveal that all the CO reacted over FeCo-*x* catalysts are converted to $CO_2$ without the any methanation reaction.

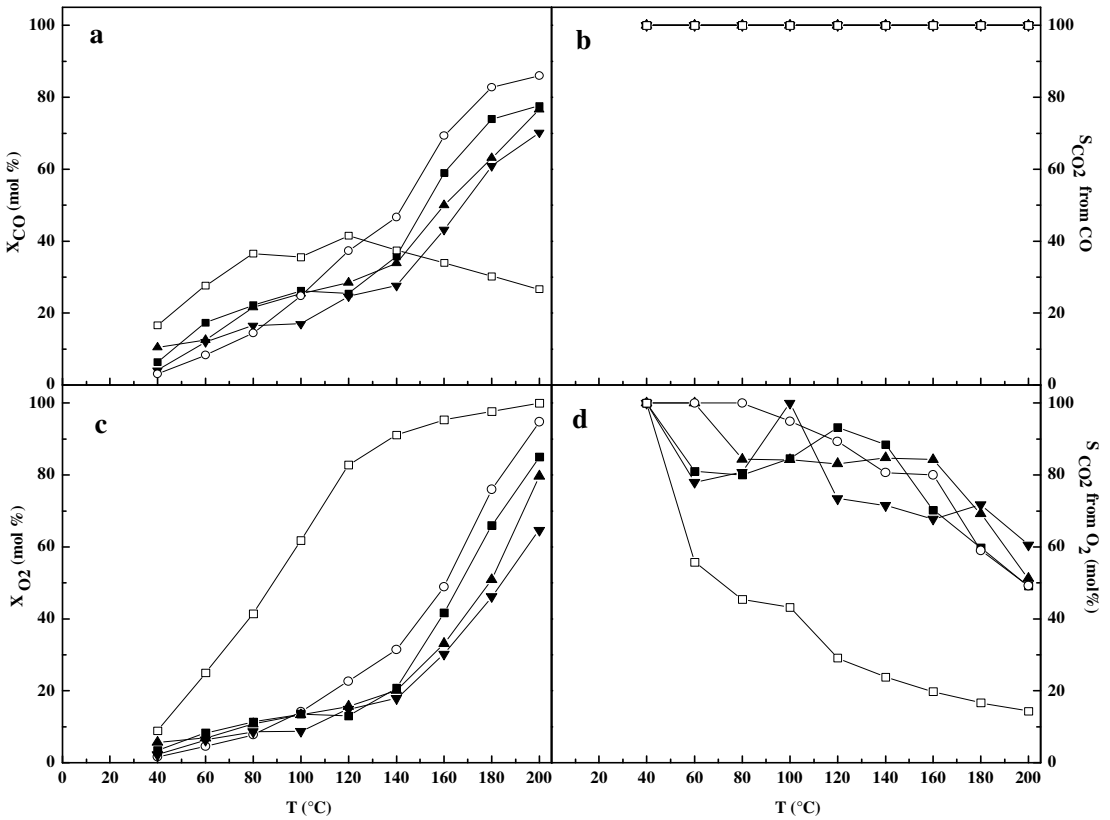


**Figure 4.11**. CO conversion *vs.* reaction temperature of the FeCo-*x* catalysts for PROX-CO: (○) FeCo-*0*; (■) FeCo-*9*; (▲) FeCo-*14*; (▼) FeCo-*19*; (□) *2.4* FeCo-*14*: (a), CO conversion; (b), $CO_2$ selectivity from CO; (c),$O_2$ conversion; (d), $CO_2$ selectivity form $O_2$. Catalyst amount: 0.03 g.

The $O_2$ conversion reported in Fig.4.8c shows similar trend for all FeCo-*x* catalysts, $O_2$ conversion increases with increasing reaction temperature up to 200°C. All the FeCo-*x* catalysts shows almost similar oxygen conversion till 100°C, beyond this point FeCo-*0* consumes more oxygen for CO and $H_2$ oxidation. The $CO_2$ selectivity from $O_2$ is reported in Fig.4.8d, FeCo-0 show 100% $CO_2$ selectivity till 80°C, drop in selectivity observed with increase of reaction temperatures due to the parallel hydrogen oxidation. However, 49 % of the $O_2$ reacted is still converted to $CO_2$ at 200°C. In Fe substituted catalysts show a strange behavior for $CO_2$ selectivity, it shows up and down

behavior with the increase of temperature, similar selectivity behavior is reported for PROX reactions[30]. FeCo-*14* show a stable selectivity of 84% for $CO_2$ from 80°C to 160°C, beyond this point drop in selectivity observed and it show a selectivity of 51% at 200°C. The presence of gold in the catalysts shows an increasing trend in the oxygen conversion(Fig.4.8c), 100% $O_2$ conversion observed over this catalyst at 200°C. The selectivity reported in Fig.4.8d clearly show a sharp decrease in selectivity of the gold catalysts and at 200°C, 14% of the reacted oxygen is converted to $CO_2$, which is the lowest value in the series. It is evident from the results that gold supported catalysts promotes hydrogen oxidation compared to CO oxidation. A collapsed spinel structure observed in the FTIR of gold catalysts after reaction (Fig.4.10)

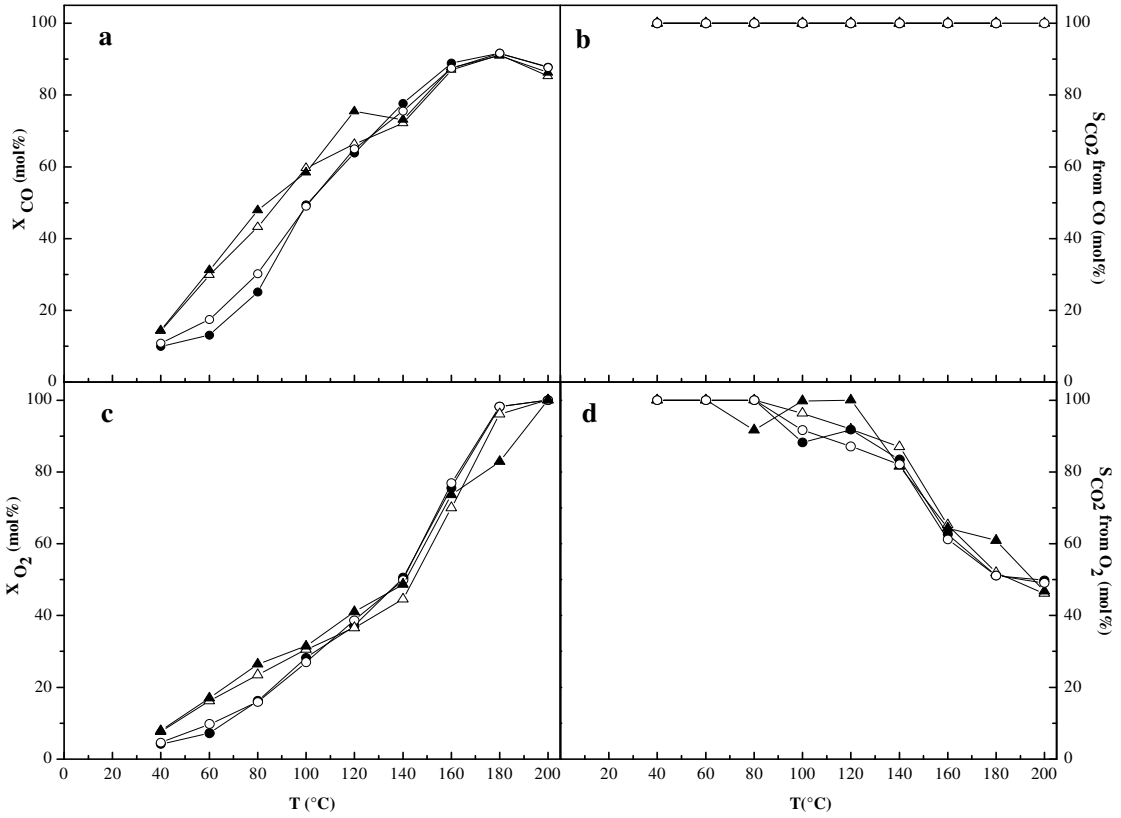


**Figure 4.12**. CO PROX activity vs. reaction temperature for FeCo-*0* (○;●) and FeCo-*14* (△,▲): (a), CO conversion; (b), $CO_2$ selectivity from CO; (c), $O_2$ conversion; (d), $CO_2$ selectivity form $O_2$. Catalyst amount: 0.1 g. Open and full symbols refer to fresh and regenerated samples, respectively.

Fig.4.9. show the activity of FeCo-*0* and FeCo-*14* catalysts in PROX with higher space velocity conditions (W/F ratio of 0.108 g s/cm$^3$). Superior activity of the FeCo-*14* is manifest from Fig.4.9a. FeCo-*14* system show higher CO oxidation activity from 40°C to 120°Ccompared to FeCo-*0*, beyond this point similar CO oxidation activity

observed till 200°C. At high space velocity conditions contact time of the reactant on the surface of the catalysts increases and activity of the catalysts is then enhanced, similar behavior reported for PROX over $Fe_2O_3$ promoted CuO-$CeO_2$ [31]. Calculated $T_{50}$ of the FeCo-*0* and FeCo-*14* are 101°C and 88°C, respectively. Oxygen conversion reported in Fig.4.9c show an increase at the beginning for FeCo-*14* till 100°C, no further difference observed beyond this point. Increase of space velocity show some improvement in the $CO_2$ selectivity of the FeCo-*14* catalysts, it show 100% $CO_2$ selectivity from $O_2$ till 80°C, beyond this point drop in selectivity observed. At 200°C FeCo-0 and FeCo-14 shows almost similar $CO_2$ selectivity ( around 38% of the reacted oxygen converted to $CO_2$). Regenerative study carried out over FeCo-*0* and FeCo-*14* with similar reaction conditions and the results are reported in Fig.4.9., no difference in the catalytic performance observed between the fresh and regenerated FeCo-*0* anf FeCo-*14*, which indicates that no modifications in the catalyst occurred during the reaction, which is evident from the FTIR of FeCo-x systems reported in Fig.4.10.

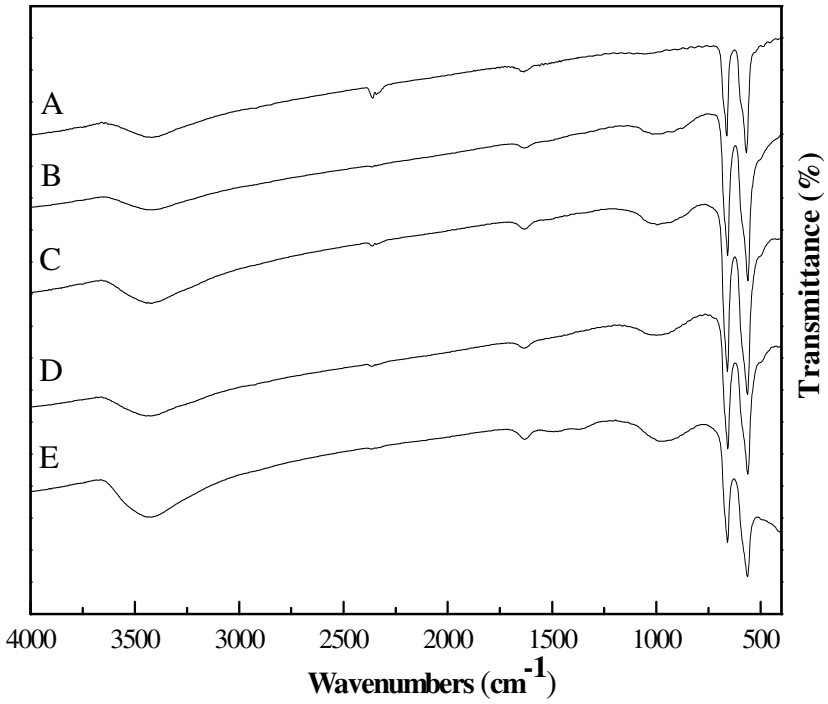


**Fig.4.13**. FTIR spectra of FeCo-*x* catalysts after reaction: (A), FeCo-*0* (B), FeCo-9; (C), FeCo-*14*; (D), FeCo-*19*; (E), 2.4 Au/FeCo-14

## 4.5. Conclusions

A series of iron doped cobalt oxide spinels are prepared by hard template method. Obtained materials possess the structural characteristics of the SBA-15 template, although partial structural collapse observed over Fe substituted spinels compared to pure cobalt spinel. All the materials possess high surface area (93-133 $m^2/g$), pore volume (0.15 - 0.46 $cm^3/g$) and narrow pore size distribution (3.1- 3.7 nm). A bispinel phase observed in FeCo-*14* and FeCo-19. No significant improvement observed in the CO oxidation of FeCo-*x* systems with the increase of Fe content in the catalysts. Gold deposited FeCo-*14* showed higher activity in CO oxidation in the absence of hydrogen, $T_{50}$ of the catalyst is below 40°C.For PROX reaction, FeCo-0 show superior activity in the series with low space velocity conditions. Superiority of the FeCo-*14* catalysts observed over FeCo-*0* at higher space velocity conditions. Compared to FeCo-*0*, FeCo-*14* showed a $T_{50}$ of 88°C at this condition. A higher oxygen conversion and low selectivity observed over gold support catalyst. No methanation reaction observed over FeCo-*x* systems.

## References

[1] J.P. Jacobs, A. Maltha, J.G.H. Reintjes, J. Drimal, V. Ponec, H.H. Brongersma, Journal of Catalysis 147 (1994) 294-300.

[2] M. Wojciechowska, M. Zieliński, A. Malczewska, W. Przystajko, M. Pietrowski, Applied Catalysis A: General 298 (2006) 225-231.

[3] G. Fortunato, H.R. Oswald, A. Reller, Journal of Materials Chemistry 11 (2001) 905-911.

[4] G. Maniak, P. Stelmachowski, J.J. Stanek, A. Kotarba, Z. Sojka, Catalysis Communications 15 (2011) 127-131.

[5] M. Stoyanova, S. Christoskova, M. Georgieva, Applied Catalysis A: General 274 (2004) 133-138.

[6] A.A. Mirzaei, R. Habibpour, E. Kashi, Applied Catalysis A: General 296 (2005) 222-231.

[7] T.A.S. Ferreira, J.C. Waerenborgh, M.H.R.M. Mendonça, M.R. Nunes, F.M. Costa, Solid State Sciences 5 (2003) 383-392.

[8] A.A. Mirzaei, R. Habibpour, M. Faizi, E. Kashi, Applied Catalysis A: General 301 (2006) 272-283.

[9] J. Jiang, L.H. Ai, Materials Letters 64 (2010) 945-947.

[10] C. Altavilla, M. Sarno, P. Ciambelli, Chemistry of Materials 21 (2009) 4851-4858.

[11] H. Romar, R. Lahti, P. Tynjälä, U. Lassi, Topics in Catalysis 54 (2011) 1302-1308.

[12] S.G. Christoskova, M. Stoyanova, M. Georgieva, Applied Catalysis A: General 208 (2001) 243-249.

[13] L. Menini, M.C. Pereira, A.C. Ferreira, J.D. Fabris, E.V. Gusevskaya, Applied Catalysis A: General 392 (2011) 151-157.

[14] D. Zhao, Q. Huo, J. Feng, B.F. Chmelka, G.D. Stucky, Journal of the American Chemical Society 120 (1998) 6024-6036.

[15] M. Haruta, Catalysis Today 36 (1997) 153-166.

[16] Y. Wang, C.M. Yang, W. Schmidt, B. Spliethoff, E. Bill, F. Schüth, Advanced Materials 17 (2005) 53-56.

[17] D. Thapa, V.R. Palkar, M.B. Kurup, S.K. Malik, Materials Letters 58 (2004) 2692-2694.

[18] B. Lefez, P. Nkeng, J. Lopitaux, G. Poillerat, Materials Research Bulletin 31 (1996) 1263-1267.

[19] C.-W. Tang, C.-B. Wang, S.-H. Chien, Thermochimica Acta 473 (2008) 68-73.

[20] K. Petcharoen, A. Sirivat, Materials Science and Engineering: B 177 (2012) 421-427.

[21] F. Boccuzzi, S. Coluccia, G. Ghiotti, C. Morterra, A. Zecchina, The Journal of Physical Chemistry 82 (1978) 1298-1303.

[22] S.G. Christoskova, M. Stoyanova, M. Georgieva, Applied Catalysis A: General 208 (2001) 235-242.

[23] A. Rumplecker, F. Kleitz, E.-L. Salabas, F. Schüth, Chemistry of Materials 19 (2007) 485-496.

[24] J. Zhu, Q. Gao, Microporous and Mesoporous Materials 124 (2009) 144-152.

[25] Z. Zhao, X. Lin, R. Jin, G. Wang, T. Muhammad, Applied Catalysis B: Environmental 115–116 (2012) 53-62.

[26] Q. Yang, H. Choi, S.R. Al-Abed, D.D. Dionysiou, Applied Catalysis B: Environmental 88 (2009) 462-469.

[27] E. Rombi, I. Ferino, R. Monaci, C. Picciau, V. Solinas, R. Buzzoni, Applied Catalysis A: General 266 (2004) 73-79.

[28] V.A. de la Peña O'Shea, N.N. Menéndez, J.D. Tornero, J.L.G. Fierro, Catalysis Letters 88 (2003) 123-128.

[29] K. Omata, T. Takada, S. Kasahara, M. Yamada, Applied Catalysis A: General 146 (1996) 255-267.

[30] D. Gamarra, G. Munuera, A.B. Hungría, M. Fernández-García, J.C. Conesa, P.A. Midgley, X.Q. Wang, J.C. Hanson, J.A. Rodríguez, A. Martínez-Arias, The Journal of Physical Chemistry C 111 (2007) 11026-11038.

[31] K. Sirichaiprasert, S. Pongstabodee, A. Luengnaruemitchai, Journal of the Chinese Institute of Chemical Engineers 39 (2008) 597-607.

CHAPTER

5

# Low temperature CO oxidation and preferential oxidation of CO over mesoporous CuO-$CeO_2$ catalysts

## 5.1. Introduction

Ceria a light rare-earth element discovered in 1803 by Jons Jakob and Wilhelm Hisinger in Sweden, and Martin Heinrich Klaproth in Germany. It wasd named after the dwarf planet Ceres [1]. Monazite, Bastnasite and Loparite are the main cerium cerium containing minerals. Commercially cerium is produced by solvent (liquid-liquid) extraction (SX), selective precipitation and ion exchange (IX) method. Solid cerium compounds obtained from fractional extraction, solvent extraction and ion exchange will produce solutions of cerium. Applications of cerium based materials are related to its potential redox chemistry, its high affinity for oxygen and sulfur, and absorption / excitation energy bands associated with its electronic structures. Major areas of application of ceria based materials include catalysis and chemicals, glass and ceramics, phosphors and metallurgy[2].

Ceria-based materials also used as electrolytes in solid oxide fuel cells due to its good ionic conduction[3].The most successful industrial applications of ceria as an oxygen storage material in automotive three- way catalytic converters (TWCs) due to its temperature stability and $Ce^{3+}$- $Ce^{4+}$ redox cycle [4].

### *5.1.2. Structural properties of ceria*

Cerium has an electronic configuration $4f^2 5d^0 6s^2$ can exhibit +3 and +4 oxidation states. Thermodynamic data indicates that cerium metal is not stable in presence of oxygen, it can easily form $Ce_2O_3$ and $CeO_2$[2].Cerium oxide has the fluorite ($CaF_2$) structure with space group Fm3m, which is named after the mineral form of calcium fluoride. It has a face centered cubic unit cell (Fig.5.1) with all the eight corners and face centers are occupied by Ce ions and all the tetrahedral holes are filled by oxygen (big gray colored atom in Fig.5.1). In this structure each cerium ions are coordinated to eight equivalent nearest neighboring oxygen anions at the corner of a cube and each oxygen anion is tetrahedrally coordinated by four cations (Fig.5.1). When treated in reducing atmosphere at elevated temperature cerium form nonstoichiometric $CeO_{2-x}$ oxides, however, even after the loss of considerable amount of oxygen $CeO_2$ remains it fluorite crystal structure. Interaction of ceria with hydrogen is reported in Fig.5.2.[5-6]

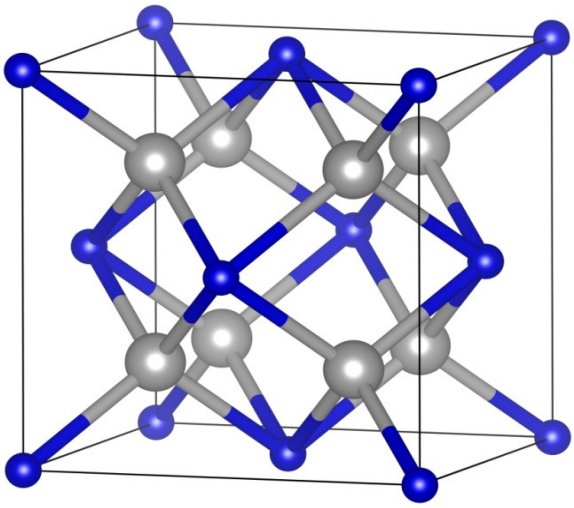

**Figure 5.1**. Schematic representation of fcc cell of $CeO_2$

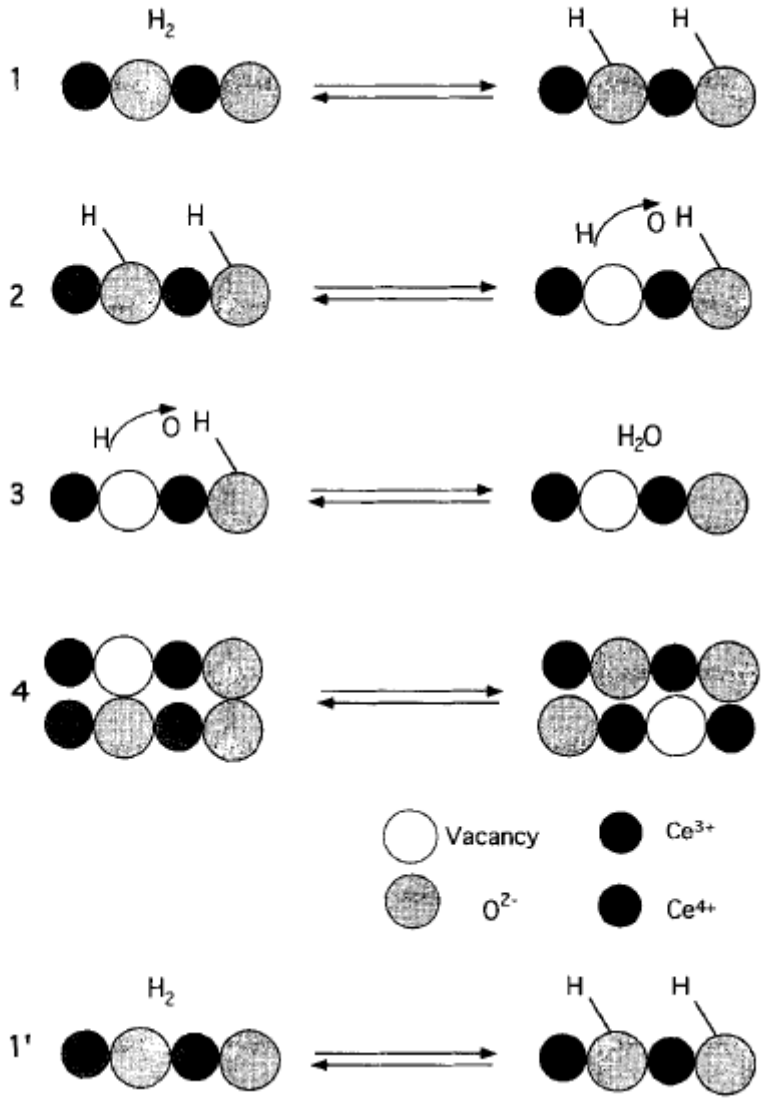


**Figure 5.2**. Proposed pathway for $CeO_2$ surface reduction [5-6]

Ceria based materials are of great interest in the field of catalysis, the suitability of ceria is mainly due to its ability to shift easily between reduced and oxidized state ($Ce^{4+}$/ $Ce^{3+}$), which results in rapid formation and elimination of oxygen vacancy defects and it often leads to a strong metal-support interaction (SMSI)[7]. Ceria lattice doped with metals leads to the formation of a solid solution, which allows the tuning of oxygen conduction, electronic conduction and catalytic properties. An additional advantage of ceria is the stabilization of the active metal phase in a highly dispersed state[8]. The CuO-$CeO_2$ catalytic systems has been examined for several processes include CO oxidation[9], CWO of phenol[10], $SO_2$ reduction[11], NO reduction [12],

methane oxidation[13] and water gas shift reaction [14]. Many authors investigated the effect of preparation method on catalytic activity of $CuO-CeO_2$ systems in water gas shift reaction and CO oxidation[15-16]. Varying preparation method often leads to changes in the morphology and dispersion of copper species. It is believed that increasing the surface area and reducing the particle size to nanoscale will provide numerous, more reactive sites so as to enhance the catalytic activity [17].

Last few years, many published reports regarding preferential oxidation and low temperature CO oxidation over $CuO-CeO_2$ systems. Many studies suggest that well dispersed copper oxide in $CuO-CeO_2$ systems are responsible for good catalytic activity in water gas shift and (selective) CO oxidation. Some authours claimed that the high activity of $CuO-CeO_2$ is linked to the special Cu-Ce-O interaction and not to the dispersion of copper. But the distinction between an active metal supported on ceria or doped into the lattice is often unclear.

Present work we report synthesis, characterization and catalytic activity of three $CuO-CeO_2$ systems with completely dispersed CuO on ceria, a mixed phase where equal amounts of copper and ceria and with higher amount of copper on ceria using hard template method. The materials characterized as to their struture, texture and redox features by X-ray diffraction (XRD), $N_2$ physisorption and temperature-programmed reduction with hydrogen ($H_2$- TPR), respectively. Catalytic activity of the materials were evaluated using low temperatureCO oxidation in the absence of hydrogen and in a hydrogen rich stream.

## 5.2. Experimental

### *5.2.1. Materials*

Tetraethylorthosilicate (TEOS, 98%), Pluronic copolymer P123 ($EO_{20}PO_{70}EO_{20}$), $Cu(NO_3)_2$ $2.5H_2O$, $Ce(NO_3)_3.6H_2O$, NaOH were supplied by Aldrich. CuO was supplied by Thermo Quest as a standard for the calibration of the TPD/R/O 1100 apparatus. HCl (37%) was provided by Merck. All the materials were reagent grade.

### 5.2.2. Synthesis of mesoporous silica SBA-15

Mesoporous silica SBA-15 was prepared under hydrothermal conditions according to the established procedure[18]. In a typical synthesis, 4 g of triblock, poly(ethylene oxide)–poly(propylene oxide)–poly(ethylene oxide) ($EO_{20}$-$PO_{70}$-$EO_{20}$) (Pluronic P123, mw 5800) was dispersed in a mixture of 120 g 2M HCl and 30 g bi-distilled water at 308 K overnight. Finally, 8.5 g of tetra-ethylorthosilicate (TEOS) was added to the homogenous solution under stirring to form a gel at 308K for 24 h. The obtained gel was then transferred into a stainless-steel autoclave and heated at 373 K for 24 h under static conditions. The white solid obtained by filtration was washed with de-ionized water and dried at 313 K. Thereafter, the product was calcined in air at 823 K for 5 h.

### 5.2.3. Synthesis of mesoporous Cu-Ce catalysts

Mesoporous copper-ceria mixed oxide catalyst with varying molar concentrations of copper were synthesized using hard template method, SBA-15 was used as a template for the synthesis. In a typical synthesis appropriate amount of Cu $(NO_3)_2.2.5H_2O$ and $Ce(NO_3)_3.6H_2O$ to obtain the desired (Cu/Cu+Ce) molar ratio, were dissolved in 25 ml of ethanol. 1 g of SBA-15 added and stirred at room temperature for 1 hour in order to allow and penetrate the solution to fill pores of SBA-15 completely. Afterwards the solid was dried overnight at 60°C.The obtained solid precursor was heated in a ceramic crucible in an oven at 500°C for 3 hrs to remove the nitrate species, the step was then repeated to completely fill the pores of SBA-15. The silica template was removed from the sample by leaching with 2M NaOH at 50°C. Finally CuO-$CeO_2$ mixed oxide sample dried overnight at 50°C and calcined again at 400°C for 2 h. The catalyst after preparation was named as $Cu_xCe$, "*x*" represents the mol% of copper in the catalyst and it was found to be *17*, *43* and *76* mol %. Here after the catalysts are named to be $Cu_{17}Ce$, $Cu_{46}Ce$ and $Cu_{76}Ce$.

### 5.2.4. Characterisation

Inductively coupled plasma atomic emission spectroscopy (ICP-AES) analyses were performed with a Varian Liberty 200 spectrophotometer to determine the Cu

content. Samples (30 mg) were dissolved in hydrofluoric acid and diluted to 250 ml with bi-distilled water.

Transmission electron microscopy (TEM) images were obtained on a JEOL 200CX microscope equipped with a tungsten cathode operating at 200 kV. Finely ground samples were dispersed in n-octane in an ultrasonic bath. The suspension was then dropped on a carbon-coated copper grid for observation.

Structural characteristics of the samples were obtained by XRD using a Seifert diffractometer with 0-0 Bragg Brentano geometry with Cu Kα wavelength. The mean crystallite size was calculated by the Scherrer equation.

Textural analyses were carried out on a Sorptomatic 1990 System (Fisons Instruments), by determining the nitrogen adsorption/desorption isotherms at 77K. Before analysis, the sample were heated overnight under vacuum up to 523K (heating rate =1K$min^{-1}$).

TPR profiles were obtained on a TPD/R/O 1100 apparatus (Thermo Quest), under the following conditions: sample weight 0.05g, heating rate (from 313 to 1173 K) 10 K$min^{-1}$, flow rate 30 $cm^3$ $min^{-1}$, $H_2$ 5% by volume in $N_2$; the hydrogen consumption was monitored by a thermal conductivity detector (TCD).

### *5.2.5. Catalytic runs*

CO oxidation in the absence of hydrogen and in a hydrogen-rich stream (CO PROX) were carried out under atmospheric pressure in a quartz-glass fixed-bed continuous-flow microreactor in the 40-140 °C and 40-200 °C temperature range, respectively. The catalyst (0.03 g) was contacted with either a $CO/O_2$ mixture (total flow, 55 $cm^3$ $min^{-1}$; 1.5 vol% CO, 1.5 vol% $O_2$, balance He) or a $CO/O_2/H_2$ stream (total flow, 55 $cm^3$ $min^{-1}$; 1.5 vol% CO, 1.5 vol% $O_2$, 46 vol% $H_2$, balance He). On-line analysis of the reactor effluent was performed on a HP 6890 GC, equipped with a HP Poraplot Q capillary column and both TCD and FID (coupled with a methanator) detectors. At each reaction temperature, samples were collected after 30 min on-stream to allow the attainment of steady-state conditions. Prior to the reaction the catalysts were pretreated in air (15 $cm^3$ $min^{-1}$) at 500 °C (heating rate, 1 °C $min^{-1}$) for 1 h.

Conversion and selectivity towards $CO_2$ have been calculated for both CO ($X_{CO}$; $S_{CO_2}^{CO}$) and $O_2$ ($X_{O_2}$; $S_{CO_2}^{O_2}$) by the following equations:

$$X_{CO}\ (\text{mol}\%) = \frac{[CO]_{in} - [CO]_{out}}{[CO]_{in}} \cdot 100; \qquad S_{CO_2}^{CO}\ (\text{mol}\%) = \frac{[CO_2]_{out}}{[CO]_{in} - [CO]_{out}} \cdot 100$$

$$X_{O_2}\ (\text{mol}\%) = \frac{[O_2]_{in} - [O_2]_{out}}{[O_2]_{in}} \cdot 100; \qquad S_{CO_2}^{O_2}\ (\text{mol}\%) = \frac{0.5 \cdot [CO_2]_{out}}{[O_2]_{in} - [O_2]_{out}} \cdot 100$$ where

terms in brackets are the inlet and outlet concentrations.

## *5.3.* Results and discussion

### *5.3.1. Characterization of SBA-15*

The low angle X-ray diffraction pattern of SBA-15 (Fig. 6.1) shows three well-resolved peaks which can be indexed as the (100), (110), and (200) reflections characteristic of the 2-D hexagonal (*P6mm*) structure.

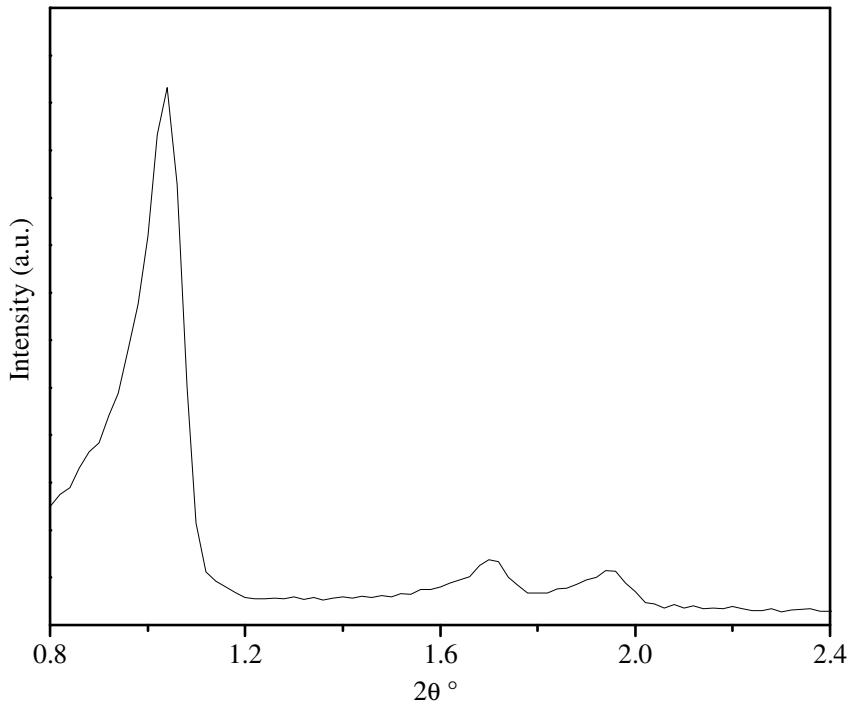


**Figure 5.3**. Low angle XRD pattern of the SBA-15 silica template.

The transmission electron microscopy (TEM) of SBA-15 is shown in Fig. 6.2. The internal architecture of SBA-15 is clearly visible in the TEM images both the viewing directions, parallel (Fig. 6.2a) and perpendicular (Fig. 6.2b) to the main axis of the pores, confirm the highly ordered 2-D hexagonal regularity. The ordered arrays of silica channels have a mean diameter of *ca.* 6-7 nm with a wall thickness of about 3 nm.

Nitrogen physorption isotherm of SBA-15 template are reported in Fig. 6.3, which shows a type IV isotherm with an H1 hysteresis loop expected for mesoporous silica with cylindrical pore geometry. A surface area of 951 $m^2$ $g^{-1}$ and a pore volume of 1.65 $cm^3$ $g^{-1}$ (Table 6.2) were calculated from the BET equation. The BJH method was applied to the desorption branch of the isotherm to obtain the pore size distribution curve (Fig. 6.3, inset) which appears quite narrow and centered at 6.9 nm (Table 6.2), in agreement with the TEM results.

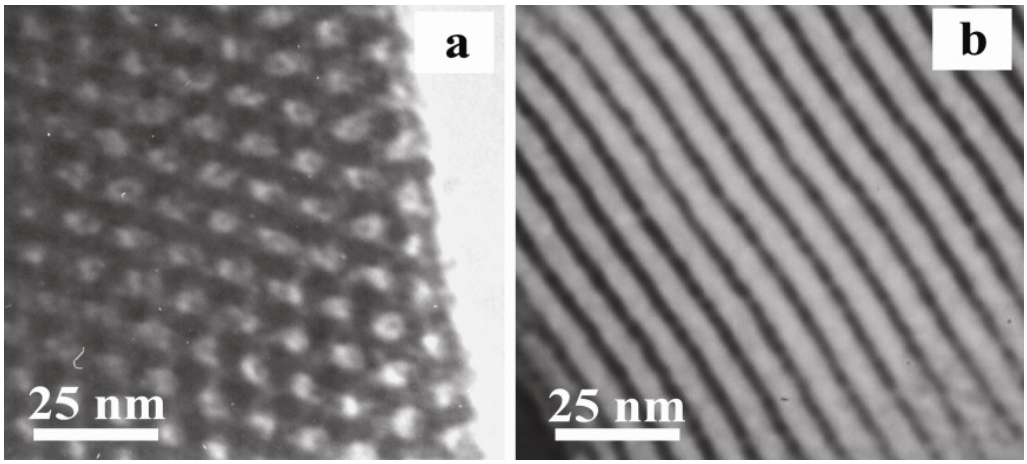


**Figure 5.4.** TEM images of the SBA-15 silica template.

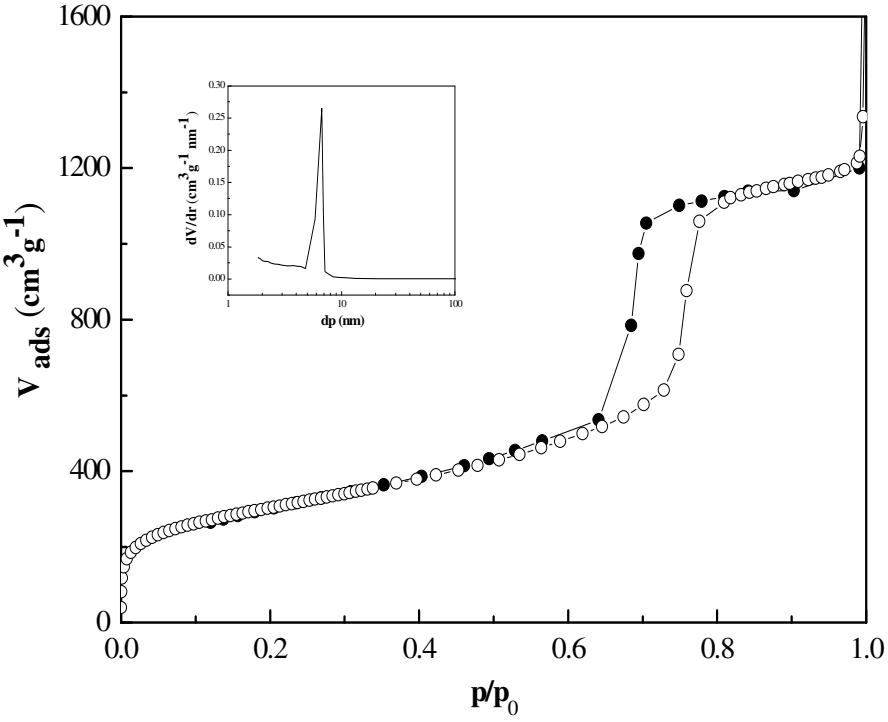


**Figure 5.5.** Nitrogen adsorption/desorption isotherm and pore size distribution plot (inset) of the SBA-15 silica template.

### *5.3.2. Characterization of $Cu_xCe$ catalysts*

X-ray diffraction patterns of the $Cu_xCe$ catalysts are shown in Fig.1. All the catalysts exhibit the presence of a fluorite-type cubic crystal structure typical of $CeO_2$ with diffraction peaks at 2θ= *28.5, 33.1, 47.5, 56.3* and *69.4°*. $Cu_{43}Ce$ catalysts presents two narrow diffraction peaks of highly crystalline monoclinic tenorite-phase CuO at $2\theta$ = *35.5, 38.7°* as well as some weak peaks in $2\theta$ = *32.6, 48.4, 58.3, 61.6°*, these peaks are highly intense in $Cu_{76}Ce$. No peaks corresponding to CuO are visible in $Cu_{17}Ce$ catalysts, the absence of CuO diffraction peaks ascribed to the substitution of copper in the ceria lattice or the formation of extremely small copper oxide clusters, indicating homogeneous dispersion of copper species on the ceria matrices. These results indicated that only a part of the $Cu^{2+}$ enter the ceria lattice due to smaller ionic radius of copper compared to ceria, ($Cu^{2+}$- *0.79 Å* , $Ce^{4+}$- *0.92 Å*) [19] to form a solid solution and rest of the $Cu^{2+}$ formed bulk metal oxide particles on the surface of $CeO_2$ when copper loading exceeds 17 mol% and it is visible with X-ray diffraction. The average particle size of

$CeO_2$ and CuO are calculated using Scherer formula and the details are reported in Table 5.1.

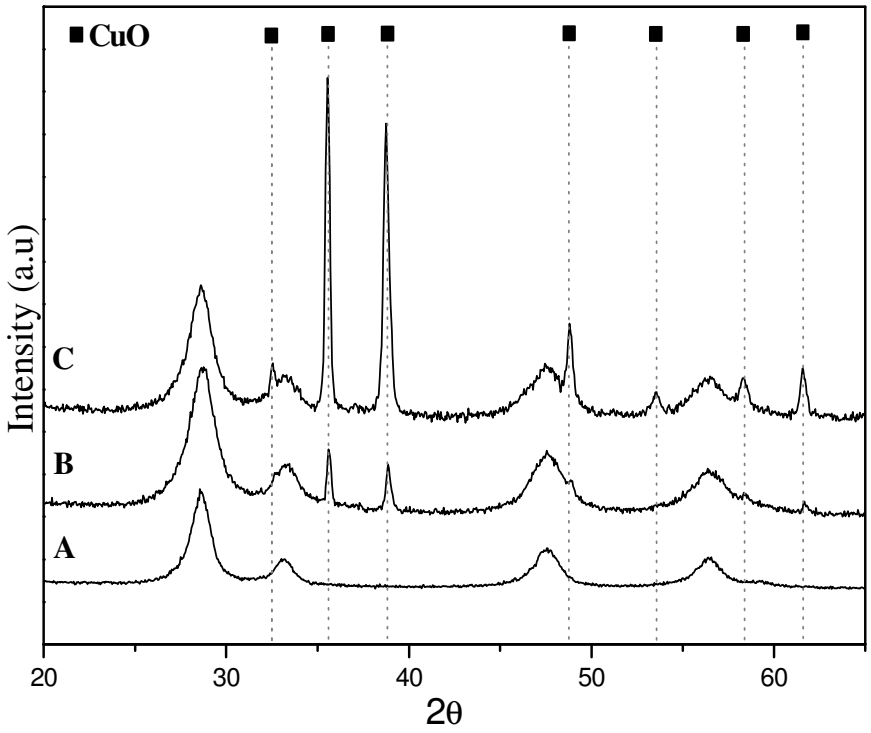


**Figure 5.6.** XRD patterns of $Cu_xCe$ catalysts: (A), $Cu_{17}Ce$; (B), $Cu_{43}Ce$; (C), $Cu_{76}Ce$.

Table 5.1. Structural parameters of $Cu_xCe$ catalysts

| Catalyst | $d_{CeO2}$ [a] (nm) | $d_{CuO}$ [a] (nm) |
|---|---|---|
| **$Cu_{17}Ce$** | 8.5 | - |
| **$Cu_{43}Ce$** | 6.5 | 29.2 |
| **$Cu_{76}Ce$** | 7.4 | 33.2 |

[a] Calculated using Scherrer formula

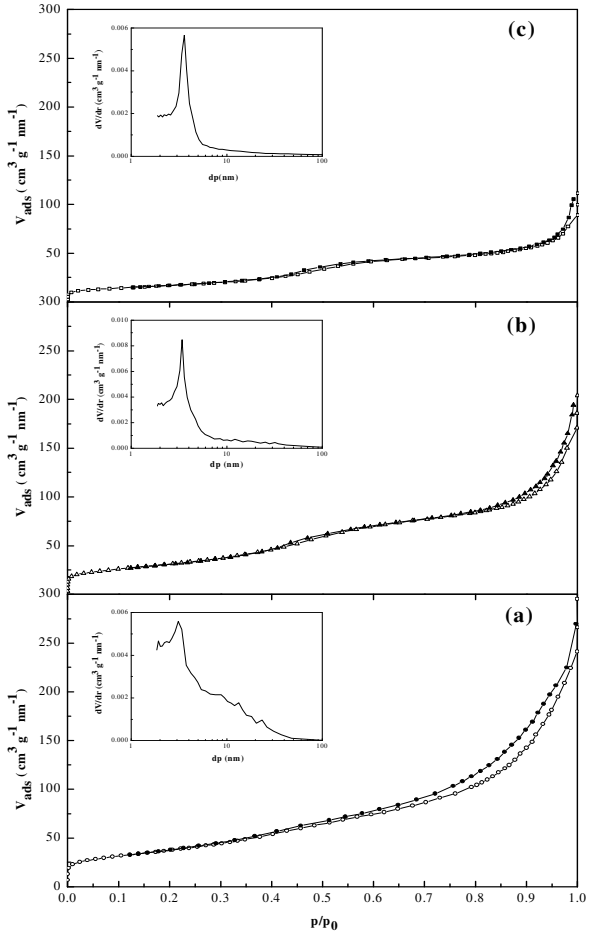


**Figure 5.7**. Nitrogen adsorption/desorption isotherm and pore size distribution plot (inset) of $Cu_xCe$ catalysts: $Cu_{17}Ce$, (a); $Cu_{43}Ce$, (b); $Cu_{76}Ce$, (c).

$N_2$ adsorption–desorption isotherm and pore size distribution (insight) of $Cu_xCe$ catalysts are presented in Fig.2. All the $Cu_xCe$ catalysts exhibit similar adsorption/desorption isotherm typical of mesoporous transition metal oxides prepared through hard template method [16]. We observe a decreasing trend in specific surface area and pore volume of $Cu_xCe$ catalysts with increasing the CuO loading, similar trend was observed for CuO-$CeO_2$ systems prepared by co-precipitation method[20]. The trend is not usual for materials prepared with hard template method[21], but the careful investigation in the materials preparation, it is clear that the obtained materials are not calcined after the silica removal. The drop in surface area and pore volume of our materials might me due to the partial structural collapse by thermal treatment (at 400° C ) after leaching off the template, even though it possesses higher surface area compared the traditional co-precipitation method[20, 22]. The BJH pore size

distribution of $Cu_xCe$ catalysts reported in Fig.2 (insight). All the $Cu_xCe$ catalysts exhibits narrow unimodal pore size distribution with maximum pore size of *3.1, 3.4* and *3.6* nm for $Cu_{17}Ce$, $Cu_{43}Ce$, and $Cu_{76}Ce$ respectively, these values are expected for the replicas of SBA-15, which in fair agreement with our previous result[23]. Details about the surface area, pore volume and pore diameter of the template and $Cu_xCe$ catalysts are reported in Table 1.

**Table 5.2**. Textural properties of the SBA-15 and $Cu_xCe$ catalysts.

| Sample | BET surface area ($m^2/g$) | Pore Volume ($cm^3/g$) | Pore diameter (nm) |
|---|---|---|---|
| SBA-15 | 1151 | 1.67 | 6.5 |
| $Cu_{17}Ce$ | 136 | 0.23 | 3.1 |
| $Cu_{43}Ce$ | 114 | 0.35 | 3.4 |
| $Cu_{76}Ce$ | 62 | 0.12 | 3.6 |

The $H_2$-TPR profiles of CuO-$CeO_2$ catalytic systems are shown in Fig.3. The reduction profile of pure CuO was characterised by a single peak at 367° C, which in agreement with the previous literature result [24]. Pure $CeO_2$ (not shown in figure) reduction occurs at 450° C and 900° C, ascribed to the reduction of surface and bulk oxygen[15]. The reduction features of ceria dramatically changed in the presence of copper. An entirely different reduction profile observed for CuO-$CeO_2$ catalytic systems, it exhibit well defined reduction peaks in the range 150-300° C (as in Fig.3).The presence of two reduction peaks in $Cu_{17}Ce$ at 169° C and 229° C for α and β-peaks, respectively, corresponds to the two step reduction of CuO to $Cu^0$. The calculated hydrogen consumption for the CuO reduction in $Cu_{17}Ce$ is considerably larger (1316.2 $\mu mol/g_{cat}$), compared to be the value expected for the reduction of CuO to $Cu^0$ (1108 $\mu mol/g_{cat}$), the excess hydrogen consumption for the CuO reduction in $Cu_{17}Ce$ expected to be the reduction of ceria together with copper and storage of $H_2$ in the catalyst, which is well documented in literature [14, 25]. Increase in CuO content results the formation of a new peak at higher temperature region, called the γ- peak (a shoulder peak in $Cu_{43}Ce$ and a broad peak in $Cu_{76}Ce$). The presence of three reduction peaks in $Cu_{43}Ce$ and $Cu_{76}Ce$ systems is an indication of three different Cu species in the catalysts. First two peaks of $Cu_xCe$ (α and β peaks) indicates the step wise reduction of

$Cu^{2+}$ to $Cu^{+}$, closely followed by the reduction from $Cu^{+}$ to $Cu^{0}$. The higher temperature peak, called γ peak, in $Cu_{43}Ce$ and $Cu_{76}Ce$ represents the reduction of bulk copper oxide (crystalline forms). This result is in agreement with the XRD results reported in Fig.1. Details of hydrogen consumption for $Cu_xCe$ systems are reported in table 2. It is clear from the table that the hydrogen consumption for the stepwise reduction of CuO species to $Cu^0$ in $Cu_{43}Ce$ is similar (i.e, for the α, β and γ peaks). This suggests that all the three copper species are homogeneously distributed in $Cu_{43}Ce$ compared to $Cu_{17}Ce$ and $Cu_{76}Ce$. All the $Cu_xCe$ systems reduced at lower temperatures compared to pure oxide, this suggests the strong interaction of copper-ceria in all system.

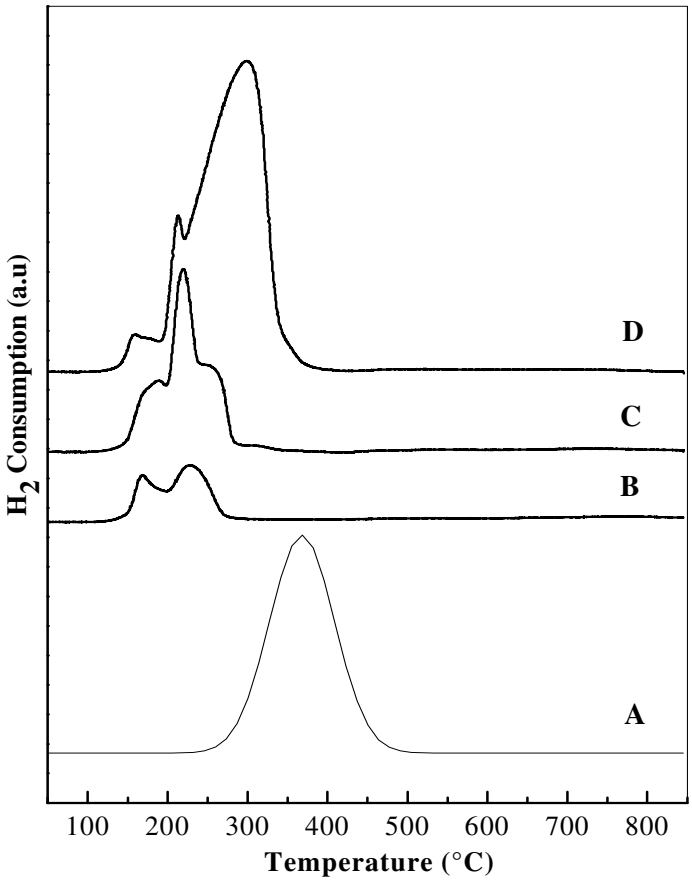


**Figure 5.8**. $H_2$-TPR profile of (A) CuO, (B) $Cu_{17}Ce$, (C) $Cu_{43}Ce$, (D) $Cu_{76}Ce$.

**Table 5.3**. Summary of TPR results over $Cu_xCe$ catalysts

| Catalysts | $H_2$ consumption (μmol/$g_{cat}$) | | | Total amount (μmol/$g_{cat}$) |
|---|---|---|---|---|
| | α (°C) | β (°C) | γ (°C) | |
| $Cu_{17}Ce$ | 483.5 (169) | 832.7 (229) | - | 1316.2 |
| $Cu_{43}Ce$ | 1046.2[a] (188) | 1109.2[a] (220) | 1180.4[a] (255) | 3335.8 |
| $Cu_{76}Ce$ | 427.5 (159) | 839.0 (213) | 7908.5 (296) | 9175.0 |

[a] *calculated using deconvolution method*

## *5.4.* Catalytic activity of $Cu_xCe$ catalysts

### *5.4.1. CO oxidation activity in the absence of hydrogen*

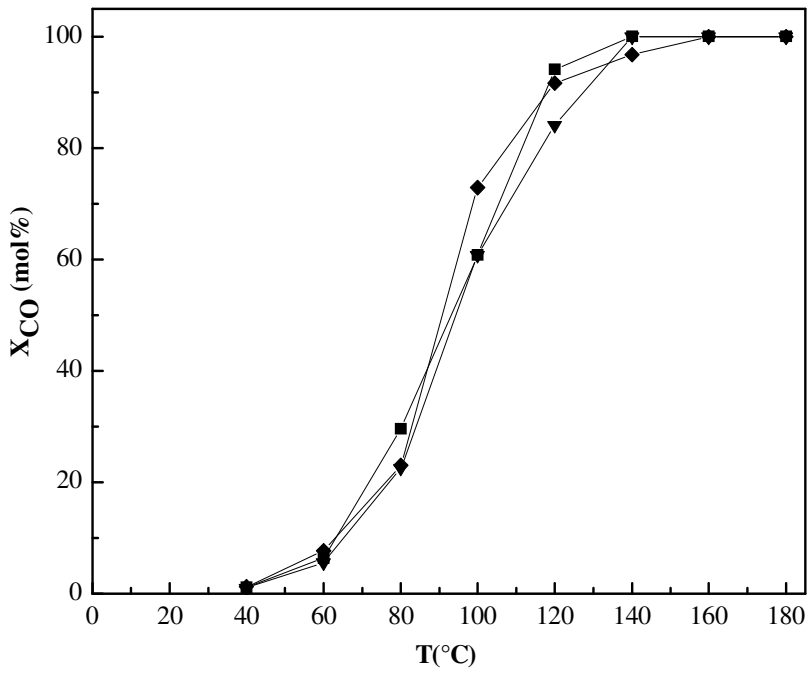


**Figure 5.9**. CO conversion *vs.* reaction temperature of the $Cu_xCe$ catalysts: (▲) $Cu_{17}Ce$; (■) $Cu_{43}Ce$; (♦) *$Cu_{73}Ce$*.

The catalytic activity of $Cu_xCe$ catalysts in low temperature CO oxidation, plotted against temperature are presented in Fig.5 (A). All the catalysts are active in the reaction and the activity of the catalysts increases with temperature. Increasing the temperature up to 80°C causes a smooth increase in activity, a further increase of temperatures results a steeper increase in activity without any difference between catalysts. All the catalysts achieve 100% CO conversion at 160°C. No remarkable

difference in the catalytic activity observed with the increase of CuO in $Cu_xCe$ systems. Temperature for 50% CO conversion ($T_{50}$) is presented in Fig.5 (B), almost similar activity observed for all catalysts, $Cu_{76}Ce$ is the lowest in the series, it achieves 50% conversion at 91 °C. $Cu_{17}Ce$ and $Cu_{43}Ce$ exhibit 50% conversion at 95 and 93 °C, respectively.

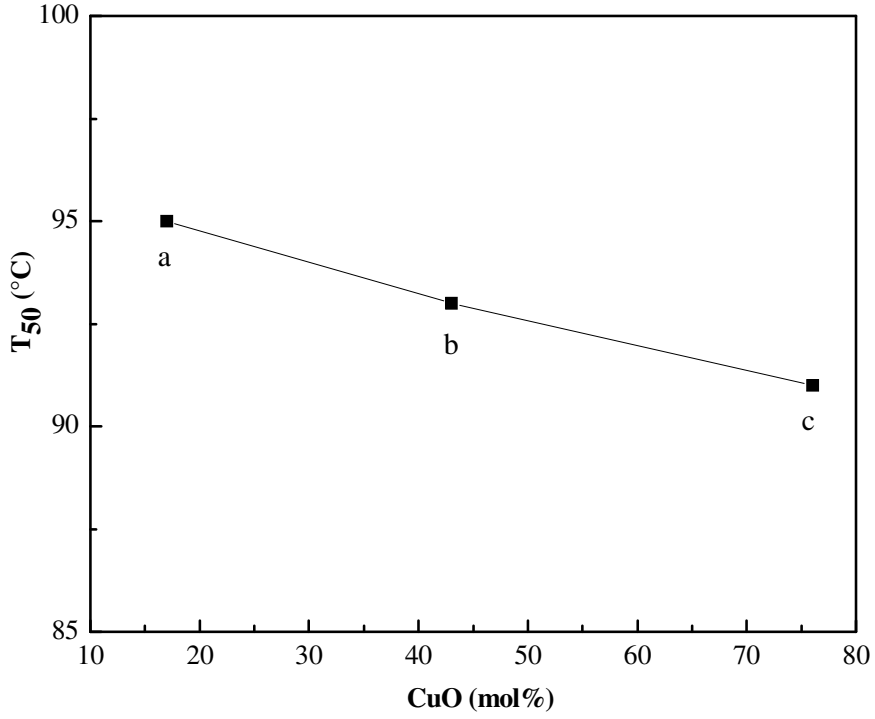


**Figure 5.10.** Temperature for 50% CO conversion vs CuO mol%

In the present study we observed that the $T_{50}$ decreases slightly with increasing CuO concentration from *17-76* mol% (Fig.5 (B)), this is in contrast to most of the published results in the literature, where the CO conversion increases with increasing CuO loading to a particular concentration, further increase of CuO loading increases the $T_{50}$ [26-27]. The reason of increasing the $T_{50}$ is due to the formation of crystalline phase of CuO, which decreases the number of accessible active phase species with the increase of CuO crystalline phase and consequently the catalytic activity. In present study we observed almost similar activity for all the catalysts, $T_{50}$ of the present catalytic systems decreases with increasing CuO content. An increase in catalytic activity observed by *SKA°RMAN* et al[28] in 80 % CuO-$CeO_2$ system, their report suggest that the dispersion of ceria crystallites over copper oxide support increases the

surface area thereby it promotes the reaction at higher CuO loading. For comparing, the performances of the present catalysts with copper-ceria catalyst previously reported by other authors are reported in Table 5.4, present work is comparable even if their reaction conditions and preparation methods are different than ours.

**Table 5.4.** Comparison of the preparation method and experimental conditions used for CO oxidation in the present work with those of literature data.

| Preparation method | Sample weight (mg) | CO (vol %) | $O_2$ (vol %) | Total flow rate ($cm^3$ $min^{-1}$) | $T_{50}$ (°C) | Refs. |
|---|---|---|---|---|---|---|
| Surfactant -templated | 500 | 1 | 1 | 80 | *(a)* | [9] |
| Hydrothermal + DP* | 400 | 1 | 2 | *(b)* | *(c)* | [29] |
| Co-precipitation | 250 | 1 | 1 | 43 | *(d)* | [30] |
| DP* | 200 | 1 | 1 | 43 | *(e)* | [31] |
| Hard template + WI* | 150 | 1 | 5 | 50 | 116 | [26] |
| Urea-nitrate combustion | 50 | 2 | 1.25 | 50 | 107 | [32] |
| Hard template | 30 | 1 | *(f)* | 50 | 77 | [27] |
| Alcohothermal | 50 | 1 | *(f)* | 33.6 | 105 | [33] |
| Sol-gel + impregnation | 50 | 1 | *(f)* | 33.6 | 115 | [34] |
| Hard template | 30 | 1.5 | 1.5 | 55 | 91 | Present work |

*(a)* 90 % conversion at 80°C *(b)* Space velocity 120,000 $h^{-1}$ *(c)* 100% conversion at 150°C
*(d)* 100 % conversion at 85°C *(e)* 100% conversion at 100°C *(f)* Balanced with air
DP: Deposition –precipitation WI: Wetness – impregnation

### *5.4.2. Preferential oxidation of CO (PROX-CO)*

Preferential oxidation activity of the $Cu_xCe$ catalysts is reported in Fig.5.11. All the catalysts show similar trend in CO oxidation activity (Fig.5.11 a) with the increase of reaction temperature. All the catalysts show maximum CO oxidation activity at 160°C beyond this point drop in activity observed due to the parallel hydrogen oxidation. No appreciable differences in CO conversion activity and selectivity observed as the CuO content varied from *17* to *43* mol%, catalyst with *76* mol% of

copper show lowest activity in the series from 40-200°C. Both $Cu_{17}Ce$ and $Cu_{43}Ce$ catalysts perform well in the overall temperature range compared to $Cu_{76}Ce$. A $T_{50}$ of 88°C observed over these catalysts, whereas at the same time $Cu_{76}Ce$ show $T_{50}$ at 95°C. These values are in fair agreement with the previously published result[35]. The $CO_2$ selectivity of the $Cu_xCe$ catalysts from CO is reported in Fig.5.11b. All the catalysts exhibit 100% selectivity.

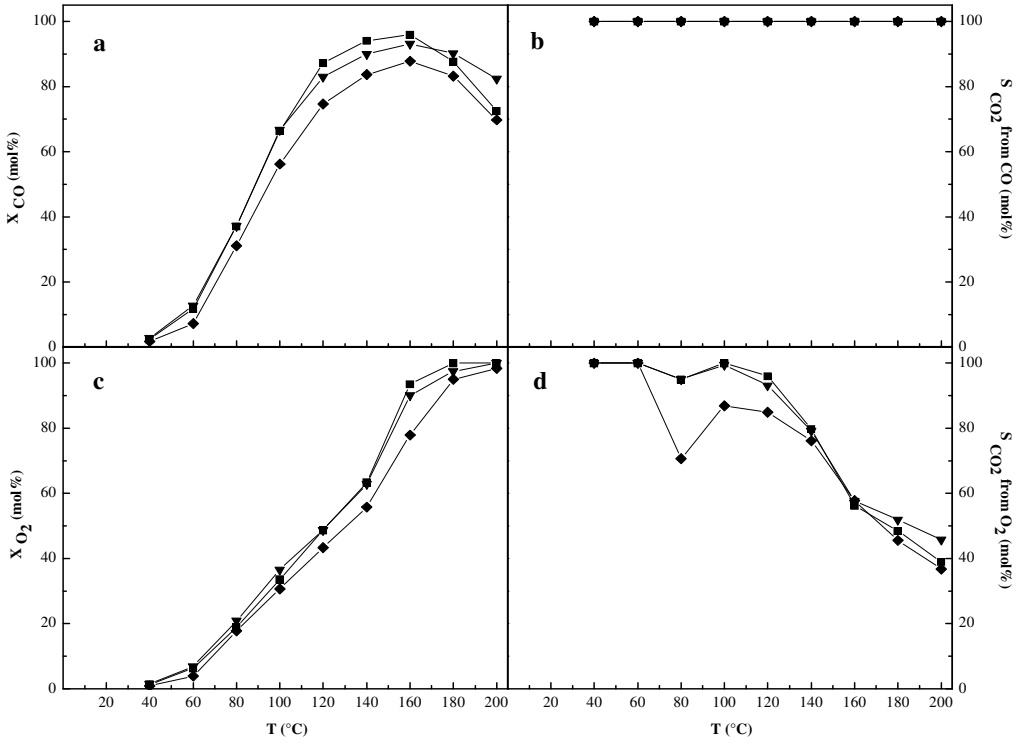


**Figure 5.11.** Effect of copper deposition method on preferential CO oxidation of CuO/CeFe-25 catalysts: (▼) $Cu_{17}Ce$, (■) $Cu_{43}Ce$ (♦) $Cu_{76}Ce$: (a), CO conversion; (b), $CO_2$ selectivity from CO; (c), $O_2$ conversion; (d), $CO_2$ selectivity form $O_2$. Catalyst amount: 0.03 g.

Total $O_2$ conversion of the $Cu_xCe$ catalysts is reported in Fig.5.11c. Steep increase in conversion observed with the increase of reaction temperature. All the catalysts show 100% conversion at 200°C except $Cu_{43}Ce$, this catalyst attain 100% $O_2$ conversion at 180°C. $Cu_{17}Ce$ and $Cu_{43}Ce$ show similar oxygen conversion activity in the series but in $Cu_{76}Ce$ the peak is slightly shifted to right. $CO_2$ selectivity from $O_2$ is reported in Fig.5.11d, $Cu_{17}Ce$ and $Cu_{43}Ce$ shows 100% $CO_2$ selectivity till 100°C (slight decrease at 80°C observed over these catalysts) beyond this point drop in selectivity observed due to the parallel hydrogen oxidation. Different behaviour observed in the

$CO_2$ selectivity of $Cu_{76}Ce$ at lower temperature range. It shows 100 % selectivity till 60°C beyond this point it drop the $CO_2$ selectivity. It is reported that the amount of copper beyond the dispersion capacity of Ce favour undesirable hydrogen oxidation [36]. But in the case of $Cu_{43}Ce$ this trend is not observed, which might be due to the smaller size of the copper particles in the system (29.2 nm) compared to $Cu_{76}Ce$ (CuO particle size is 33.2 nm) (Table 5.1). At 200°C, 45% of the oxygen is converted to $CO_2$ over $Cu_{17}Ce$, whereas at the same time $Cu_{43}Ce$ and $Cu_{76}Ce$ show 36 and 39 % $CO_2$ selectivity, respectively. The selectivity of the $Cu_xCe$ catalysts at 100- 200°C range is promising for its use in PEM fuel cell applications. Compared to the noble metal based catalysts the selectivity observed in this range is higher in Cu-Ce catalysts [37]. Minor differences in actiivty obsevred over Cu-Ce catalysts with different preparation methods [38]. However, the real mechanism of PROX over Cu-Ce catalysts is still unclear.

## *5.5.* Conclusions

Mesoporous copper-ceria catalysts with higher surface area (62-136 $m^2g^{-1}$) and pore volume (0.12-0.35 $cm^3g^{-1}$) were prepared using hard template method. All the $Cu_xCe$ catalysts showed similar behaviour in CO oxidation in the absence of hydrogen, however, $Cu_{76}Ce$ showed a low $T_{50}$ value of 91°C compared to $Cu_{17}Ce$ (95°C) and $Cu_{43}Ce$ (93°C). The activity of the catalyst in presence of hydrogen is little bit different, $Cu_{17}Ce$ and $Cu_{43}Ce$ showed similar CO oxidation activity and selectivity. $Cu_{76}Ce$ was the lowest active and selective catalyst in the series. Lowest $T_{50}$ of 88°C observed over $Cu_{17}Ce$ and $Cu_{43}Ce$ catalysts with 97% selectivity.

## References

[1] J. Beckers, G. Rothenberg, Green Chemistry 12 (2010) 939-948.

[2] A. Trovarelli, catalysis by ceria related materials, CRC press Vol.12.

[3] H. Inaba, H. Tagawa, Solid State Ionics 83 (1996) 1-16.

[4] A. Trovarelli, C. de Leitenburg, M. Boaro, G. Dolcetti, Catalysis Today 50 (1999) 353-367.

[5] J. El Fallah, S. Boujana, H. Dexpert, A. Kiennemann, J. Majerus, O. Touret, F. Villain, F. Le Normand, The Journal of Physical Chemistry 98 (1994) 5522-5533.

[6] A. Trovarelli, Catalysis Reviews 38 (1996) 439-520.

[7] H. Imagawa, A. Suda, K. Yamamura, S. Sun, The Journal of Physical Chemistry C 115 (2011) 1740-1745.

[8] T. Tabakova, M. Manzoli, D. Paneva, F. Boccuzzi, V. Idakiev, I. Mitov, Applied Catalysis B: Environmental 101 (2011) 266-274.

[9] M.-F. Luo, J.-M. Ma, J.-Q. Lu, Y.-P. Song, Y.-J. Wang, Journal of Catalysis 246 (2007) 52-59.

[10] S. Hočevar, U.O. Krašovec, B. Orel, A.S. Aricó, H. Kim, Applied Catalysis B: Environmental 28 (2000) 113-125.

[11] W. Liu, C. Wadia, M. Flytzani-Stephanopoulos, Catalysis Today 28 (1996) 391-403.

[12] P. Bera, S.T. Aruna, K.C. Patil, M.S. Hegde, Journal of Catalysis 186 (1999) 36-44.

[13] W. Liu, M. Flytzanistephanopoulos, Journal of Catalysis 153 (1995) 304-316.

[14] A. Pintar, J. Batista, S. Hočevar, Journal of Colloid and Interface Science 307 (2007) 145-157.

[15] X. Tang, B. Zhang, Y. Li, Y. Xu, Q. Xin, W. Shen, Catalysis Today 93-95 (2004) 191-198.

[16] P. Djinović, J. Batista, J. Levec, A. Pintar, Applied Catalysis A: General 364 (2009) 156-165.

[17] L. Yin, Y. Wang, G. Pang, Y. Koltypin, A. Gedanken, Journal of Colloid and Interface Science 246 (2002) 78-84.

[18] D. Zhao, Q. Huo, J. Feng, B.F. Chmelka, G.D. Stucky, Journal of the American Chemical Society 120 (1998) 6024-6036.

[19] Y. Liu, T. Hayakawa, K. Suzuki, S. Hamakawa, T. Tsunoda, T. Ishii, M. Kumagai, Applied Catalysis A: General 223 (2002) 137-145.

[20] P.V.D.S. Gunawardana, H.C. Lee, D.H. Kim, International Journal of Hydrogen Energy 34 (2009) 1336-1341.

[21] P. Djinović, J. Batista, J. Levec, A. Pintar, Applied Catalysis A: General 364 (2009) 156-165.

[22] P. Djinović, J. Batista, A. Pintar, Applied Catalysis A: General 347 (2008) 23-33.

[23] M.G.C. S.Varghese, E.Rombi, D.Meloni, R.Monaci,F.Sini, I.Ferino, advances in zeolite science and technology. An international symposium celebrating Carmine Colella's 70th birthday (2011) 309-312.

[24] M.-F. Luo, Y.-J. Zhong, X.-X. Yuan, X.-M. Zheng, Applied Catalysis A: General 162 (1997) 121-131.

[25] G. Wrobel, C. Lamonier, A. Bennani, A. D'Huysser, A. Aboukais, Journal of the Chemical Society, Faraday Transactions 92 (1996) 2001-2009.

[26] W. Shen, X. Dong, Y. Zhu, H. Chen, J. Shi, Microporous and Mesoporous Materials 85 (2005) 157-162.

[27] J. Zhu, Q. Gao, Z. Chen, Applied Catalysis B: Environmental 81 (2008) 236-243.

[28] B. Skårman, D. Grandjean, R.E. Benfield, A. Hinz, A. Andersson, L.R. Wallenberg, Journal of Catalysis 211 (2002) 119-133.

[29] K. Zhou, R. Xu, X. Sun, H. Chen, Q. Tian, D. Shen, Y. Li, Catalysis Letters 101 (2005) 169-173.

[30] X. Tang, B. Zhang, Y. Li, Y. Xu, Q. Xin, W. Shen, Catalysis Today 93–95 (2004) 191-198.

[31] X. Tang, B. Zhang, Y. Li, Y. Xu, Q. Xin, W. Shen, Applied Catalysis A: General 288 (2005) 116-125.

[32] G. Avgouropoulos, T. Ioannides, Applied Catalysis A: General 244 (2003) 155-167.

[33] X. Zheng, S. Wang, S. Wang, S. Zhang, W. Huang, S. Wu, Catalysis Communications 5 (2004) 729-732.

[34] X.-C. Zheng, S.-H. Wu, S.-P. Wang, S.-R. Wang, S.-M. Zhang, W.-P. Huang, Applied Catalysis A: General 283 (2005) 217-223.

[35] Z. Liu, R. Zhou, X. Zheng, Journal of Molecular Catalysis A: Chemical 267 (2007) 137-142.

[36] L. Dong, Y. Hu, M. Shen, T. Jin, J. Wang, W. Ding, Y. Chen, Chemistry of Materials 13 (2001) 4227-4232.

[37] G. Avgouropoulos, T. Ioannides, C. Papadopoulou, J. Batista, S. Hocevar, H.K. Matralis, Catalysis Today 75 (2002) 157-167.

[38] G. Avgouropoulos, T. Ioannides, H. Matralis, Applied Catalysis B: Environmental 56 (2005) 87-93.

CHAPTER

6

# Low temperature CO oxidation and preferential oxidation of CO over mesoporous $CuO/CeO_2$-$Fe_2O_3$ catalysts

## 6.1. Introduction

The research over $CeO_2$ containing materials got rapid growth over the last few decades due to its diverse applications, unique structure and properties[1-2]. Wide applications of $CeO_2$ in heterogeneous catalysis is mainly due to its redox behavior, i.e, ability to switch between $Ce^{4+}$ and $Ce^{3+}$ oxidation states and its oxygen storage capacity. The amount of oxygen that can be reversibly exchanged from the lattice is defined as oxygen storage capacity[3]. Due to its oxygen storage/release capacity (OSC) $CeO_2$ has become the main component of three-way catalyst (TWC). Despite its wide spread applications, its poor thermal stability and rapid sintering at high temperatures reduces its crucial oxygen storage capacity[4]. A general approach to improve the thermal stability and oxygen storage capacity of ceria is doping its fluorite structure with other metal ions [5].

Ceria- based mixed oxides $(Ce_xM_{1-x})O$ are versatile oxygen exchangers, compared to pure ceria, ceria based solid solutions show enhanced thermal stability,

oxygen storage capacity and catalytic properties[6-7]. It is observed that substitution of a lower-valent metal ion (e.g., $M^{III}$) by cerium lowers the energy barrier for the oxygen migration[8]. However, improvement in oxygen storage capacity observed by substitution of smaller homovalent ions ($Zr^{IV}$) by decreasing the activation energy for the reduction ($Ce^{IV}$ to $Ce^{III}$) and retarding the oxygen storage degradation at high temperature. Ce has 8-fold coordination in $CeO_2$, all the Ce-O bond lengths are equal to 2.34Å, but the substitution of smaller ions like $Zr^{4+}$ (ionic radii, r= 0.84 Å) and $Ti^{4+}$ (r=0.74 Å) for $Ce^{4+}$ ions (r=0.99 Å) distorts its local 8-fold coordination around the dopant site, therefore the smaller ions prefer coordination number smaller than eight[9]. The distortion in oxygen sublattice elongated the M-O bond, which is responsible for the higher oxygen storage capacity of ceria-based solid solutions[10].

Higher oxygen storage capacity observed for Ce-Cr solid solution compared to Ce-Zr. The higher oxygen storage capacity (OSC) at lower temperature is due to the interaction of redox couples in the solid solutions and its lower redox potential ($Cr^{6+}/Cr^{3+}$ =1.33V) compared to Ce ($Ce^{4+}/Ce^{3+}$= 1.61 V). The redox potential of $Fe^{3+}$ is 0.77V, therefore, $Fe^{3+}$ will be cheapest substituent for $Ce^{4+}$ in $CeO_2$ and promising candidate for higher oxygen storage material[11]. Ceria - iron mixed oxide have been investigated as a catalyst for water gas shift reaction [11], $N_2O$ decomposition [12], CO oxidation[13-14], Fisher-Tropsch synthesis[15] and ethanol steam reforming[16].

Present chapter, we discuss the synthesis, characterization and catalytic activity of a series of CuO/CeFe catalysts for CO oxidation and preferential oxidation reaction. The Ce-Fe support is prepared by a hard template method using SBA-15 mesoporosus silica as a template structure. Copper deposition is carried out over the support by using chelating-impregnation method. For comparison traditional incipient wetness impregnation method is applied for copper deposition on the support. Gold deposited CeFe solid solution is also investigated for the reaction. Copper based catalysts shows better catalytic performance for CO oxidation and preferential oxidation reaction.

## 6.2. Experimental

### *6.2.1. Materials*

Tetraethylorthosilicate (TEOS, 98 %), Pluronic copolymer P123 ($EO_{20}PO_{70}EO_{20}$), $Cu(NO_3)_2.2.5H_2O$, $Ce(NO_3)_3.6H_2O$, and NaOH were supplied by

Aldrich. Ammonium hydroxide was supplied by Fluka. Fe $(NO_3)_3.9H_2O$ and HCl (37 %) were provided by Merck. All the materials were of reagent grade.

### *6.2.2. Synthesis of mesoporous silica SBA-15*

Mesostructured silica SBA-15 was prepared under hydrothermal conditions. In a typical synthesis, 4 g of Pluronic P123 were added to 120 g of HCl (2 M) and 30 g of distilled water. After 15 h under stirring at 35 °C, 8.5 g of TEOS were added and the solution was maintained at 35 °C for 24 h under stirring. The resulting gel was then transferred into a stainless-steel autoclave and kept at 100 °C for 24 h under static conditions. The obtained suspension was filtered and the recovered solid was washed with distilled water, dried at 40 °C overnight and finally calcined in air at 550 °C for 5 h.

### *6.2.3. Preparation of Ceria-Iron bimetal oxides*

Ceria-Iron mesoporous bimetal oxide with 25 mol % of iron was synthesized using hard-template method, SBA-15 was used as a template. Total concentration of the metal ion solution used for the synthesis was 0.7 M. In a Typical synthesis appropriate amount of $Ce(NO_3)_3.\ 6H_2O$ and Fe $(NO_3)_3.9H_2O$ were dissolved in 25ml of ethanol. Into 15ml of this solution, 1 g of SBA-15 was added and stirred at room temperature for one hour to penetrate and fill the pores of SBA-15 completely. Afterwards, the solution was dried overnight at 60°C. The obtained solid precursor was heated in a ceramic crucible in an oven at 550°C for 3 h to decompose the nitrate species. The impregnation step was repeated with 10 ml metal-ethanol salt mixture. After overnight drying at 60° C, the obtained material was again calcined at 550°C for 3 hours.

The silica template was removed from the sample by leaching with 2M NaOH (1:25 S/L ratio) at 50°C. The traces of NaOH were removed by continuous washing with distilled water until the pH of the slurry reached 7. Finally Ce-Fe mixed oxide sample dried overnight at 50°C. The material after preparation was analysed with ICP and $Fe_2O_3$ content was observed to be 25 mol%. Hereafter it will be referred as CeFe-*25*, where 25 represents the mol% of Fe in the catalyst.

### 6.2.4. Copper deposition on $CeO_2$-$Fe_2O_3$ support

The CuO supported CeFe-*25* catalysts were prepared by chelating-impregnation (CI) method[17] with aqueous $[Cu(NH_3)_4]^{2+}$ solution, which was acquired by adding definite $Cu(NO_3)_2$ 2.5 $H_2O$ to the ammonia solution. The CeFe-*25* support was added to $[Cu(NH_3)_4]^{2+}$ solution followed by continuous stirring at room temperature and then the material is dried overnight at 100°C. For comparison, a catalyst was also prepared by incipient wetness impregnation (IWI) method with aqueous $Cu(NO_3)_2$ $2.5H_2O$ solution. All the materials were calcined at 550°C for 3 h in air. The obtained samples were named *XCuO*/CeFe-*25*, where *X = 8, 12, 16, 24* for CI and *17* for IWI.

### 6.2.5. Gold deposition on $CeO_2$-$Fe_2O_3$ support

Gold deposition was carried out using deposition precipitation method (DP), as reported by Haruta et-al[18]. In a typical synthesis desired amount of $HAuCl_4$ solution added drop-wise into a slurry containing CeFe-*25* support under constant stirring at 60°C. pH of the slurry maintained at 9 by the use of aqueous ammonia solution. After aging for 2 h, the material filtered, washed several times with warm distilled water and then dried at 100°C. Finally calcined under air at 300°C for 2h at a heating rate of 2°C $min^{-1}$. The material after preparation was named as *x*Au/CeFe-25, where *x* represents the amount of gold on the support and it was analysed with ICP and was observed to be 1.8 wt%. Hereafter it will be named as 1.8 Au/CeFe-25.

### 6.2.6. Characterization

Inductively coupled plasma atomic emission spectroscopy (ICP-AES) analyses were performed with a Varian Liberty 200 spectrophotometer to determine the Cu content. Samples (0.03 g) were dissolved in concentrated nitric acid and the solution was diluted to 250 $cm^3$ with bi-distilled water.

Transmission electron microscopy (TEM) images were obtained on a JEOL 200CX microscope equipped with a tungsten cathode operating at 200 kV. Finely ground samples were dispersed in n-octane in an ultrasonic bath. The suspension was then dropped on a carbon-coated copper grid for observation.

X-ray diffraction patterns were recorded on a Seifert X3000 diffractometer with a θ-θ Bragg Brentano geometry with Cu Kα radiation.

Textural analysis was carried out on a Sorptomatic 1990 System (Fisons Instruments), by determining the nitrogen adsorption/desorption isotherms at -196 °C. Before analysis, the sample was heated overnight under vacuum up to 250 °C (heating rate = 1 °C $min^{-1}$).

TPR profiles were recorded on a TPD/R/O 1100 apparatus (Thermo Quest), under the following conditions: sample weight, 0.05 g; heating rate (from 40 to 800 °C), 10 °C $min^{-1}$; flow rate, 30 $cm^3$ $min^{-1}$; $H_2$, 5 vol% in $N_2$. The hydrogen consumption was monitored by a thermal conductivity detector (TCD).

### *6.2.7. Catalytic runs*

CO oxidation in the absence of hydrogen and in a hydrogen-rich stream (CO PROX) were carried out under atmospheric pressure in a quartz-glass fixed-bed continuous-flow microreactor in the 40-140 °C and 40-200 °C temperature range, respectively. The catalyst (0.03 g) was contacted with either a $CO/O_2$ mixture (total flow, 55 $cm^3$ $min^{-1}$; 1.5 vol% CO, 1.5 vol% $O_2$, balance He) or a $CO/O_2/H_2$ stream (total flow, 55 $cm^3$ $min^{-1}$; 1.5 vol% CO, 1.5 vol% $O_2$, 46 vol% $H_2$, balance He). On-line analysis of the reactor effluent was performed on a HP 6890 GC, equipped with a HP Poraplot Q capillary column and both TCD and FID (coupled with a methanator) detectors. At each reaction temperature, samples were collected after 30 min on-stream to allow the attainment of steady-state conditions. Prior to the reaction the catalysts were pretreated in air (15 $cm^3$ $min^{-1}$) at 500 °C (heating rate, 1 °C $min^{-1}$) for 1 h. Conversion and selectivity towards $CO_2$ have been calculated for both CO ($X_{CO}$; $S_{CO_2}^{CO}$) and $O_2$ ($X_{O_2}$; $S_{CO_2}^{O_2}$) by the following equations:

$$X_{CO}\ (\text{mol}\%) = \frac{[CO]_{in} - [CO]_{out}}{[CO]_{in}} \cdot 100; \qquad S_{CO_2}^{CO}\ (\text{mol}\%) = \frac{[CO_2]_{out}}{[CO]_{in} - [CO]_{out}} \cdot 100$$

$$X_{O_2}\ (\text{mol}\%) = \frac{[O_2]_{in} - [O_2]_{out}}{[O_2]_{in}} \cdot 100; \qquad S_{CO_2}^{O_2}\ (\text{mol}\%) = \frac{0.5 \cdot [CO_2]_{out}}{[O_2]_{in} - [O_2]_{out}} \cdot 100$$

where terms in brackets are the inlet and outlet concentrations.

## 6.3. Results and discussion

### *6.3.1. Characterization of SBA-15*

The low angle X-ray diffraction pattern of SBA-15 (Fig. 6.1) shows three well-resolved peaks which can be indexed as the (100), (110), and (200) reflections characteristic of the 2-D hexagonal (*P6mm*) structure.

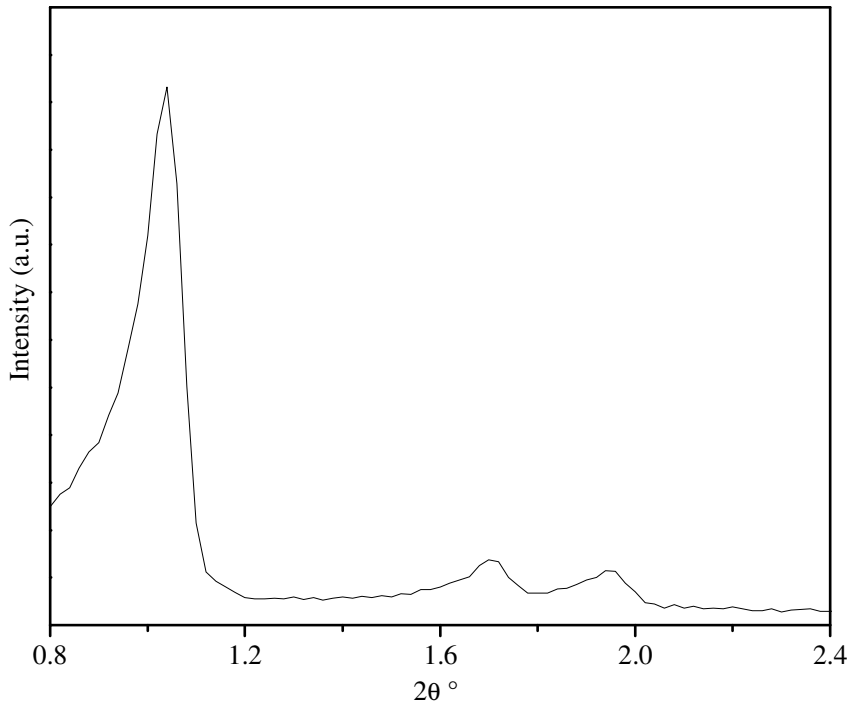


**Figure 6.1**. Low angle XRD pattern of the SBA-15 silica template.

The transmission electron microscopy (TEM) of SBA-15 is shown in Fig. 6.2. the internal architecture of SBA-15 is clearly visible in the TEM images both the viewing directions, parallel (Fig. 6.2a) and perpendicular (Fig. 6.2b) to the main axis of the pores, confirm the highly ordered 2-D hexagonal regularity. The ordered arrays of silica channels have a mean diameter of *ca.* 6-7 nm with a wall thickness of about 3 nm.

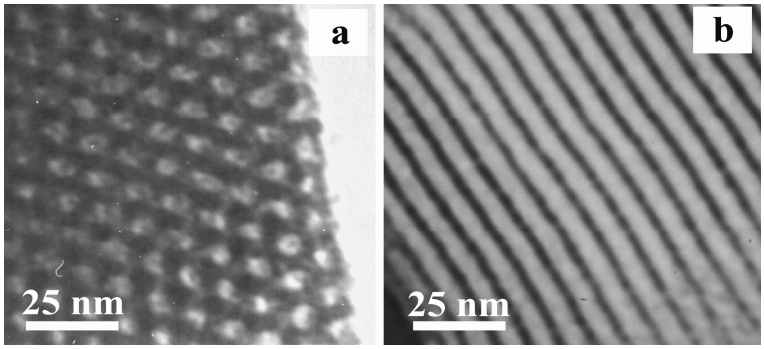


**Figure 6.2.** TEM images of the SBA-15 silica template.

Nitrogen physorption isotherm of SBA-15 template are reported in Fig. 6.3, which shows a type IV isotherm with an H1 hysteresis loop expected for mesoporous silica with cylindrical pore geometry. A surface area of 951 $m^2$ $g^{-1}$ and a pore volume of 1.65 $cm^3$ $g^{-1}$ (Table 6.2) were calculated from the BET equation. The BJH method was applied to the desorption branch of the isotherm to obtain the pore size distribution curve (Fig. 6.3, inset) which appears quite narrow and centered at 6.9 nm (Table 6.2), in agreement with the TEM results.

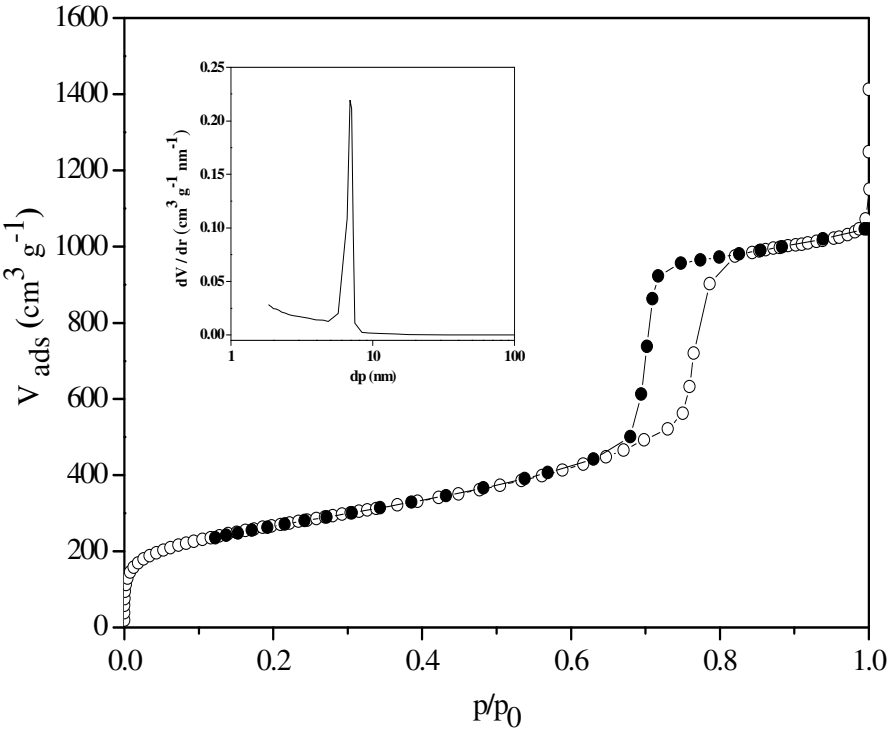


**Figure 6.3.** Nitrogen adsorption/desorption isotherm and pore size distribution plot (inset) of the SBA-15 silica template.

### *6.3.2. Characterization of CuO/CeFe-25 catalysts*

X-ray diffraction patterns of CeFe-*25* support is shown in Fig. 6.4. The diffraction patterns reveal that the CeFe-*25* matches with the cubic $CeO_2$ fluorite structure. There are no peaks corresponding to $Fe_2O_3$ observed in the diffraction pattern of CeFe-*25*. The lattice parameter obtained from the calculation of (111) peak is about 5.378 Å (Table 6.1), which is in fair agreement with the Ce-Fe solid solutions prepared with other route[11]. It is well documented in the literature that the lattice parameter of pure ceria is 5.41 Å [9, 12, 14-15]. The reduction in lattice parameter and the absence of Fe diffraction peaks in the X-ray diffraction of CeFe-*25* strongly support the formation of Ce-Fe solid solution by the substitution of smaller $Fe^{3+}$ [ionic radii, $r$ = 0.64 Å, $Ce^{4+}$ ionic radii, $r$ = 1.01 Å] in the ceria lattice. [15-16].

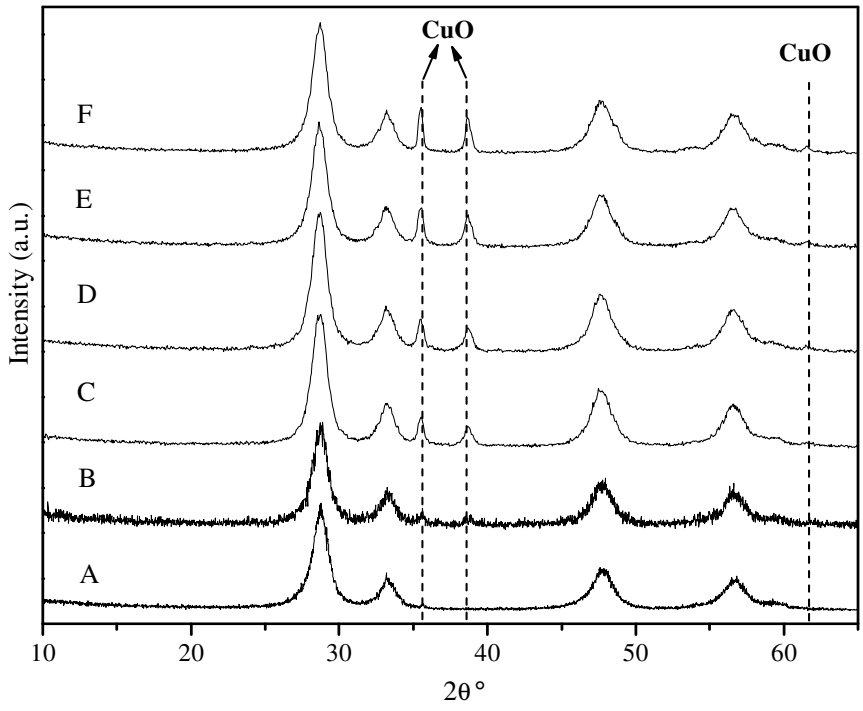


**Figure 6.4.** XRD patterns of CeFe-*25* and CuO / CeFe-*25* catalysts: (A), CeFe-*25*; (B), *8* CuO/CeFe-*25*; (C), *12* CuO/CeFe-*25*; (D), *16* CuO/CeFe-*25*; (E), *24* CuO/CeFe-*25*; (F), *17* CuO/ CeFe-*25* (IWI).

XRD patterns of a series of copper (8 - 24 wt. %) deposited CeFe-*25* catalysts are reported in Fig. 6.4. All samples exhibit the characteristic diffraction peaks of crystalline CuO at 2θ = 35.5 and 38.7°, which are referred to tenorite-phase CuO. This

suggests that the dispersion capacity of CeFe-*25* solid solution is below 8 wt %. By increasing the copper concentrations the diffraction peaks corresponding to CuO are more intense and the formation of a new peak observed at 2θ = 61.6°. The mean crystallite size and lattice parameter of the copper deposited CeFe-*25* are reported in table 6.1. Slight increase in crystallite size observed by the addition of copper to the CeFe -25 support. Addition of copper increases the lattice parameter slightly but it remains almost constant for all copper- support systems except *8*CuO/CeFe-*25*.

**Table 6.1**. Structural parameters of CeFe-*25* and CuO/CeFe-*25* system

| Sample | $CeO_2$ crystallite size [a] (nm) | Lattice parameter (Å) |
|---|---|---|
| CeFe-*25* | 6.9 | 5.378 |
| *8* CuO/ CeFe-*25* | 7.5 | 5.380 |
| *12* CuO/ CeFe-*25* | 7.6 | 5.391 |
| *16* CuO/ CeFe-*25* | 7.6 | 5.394 |
| *24* CuO/ CeFe-*25* | 8.1 | 5.396 |
| *17* CuO/ CeFe-*25*[b] | 7.4 | 5.391 |

[a] Calculated using Scherrer formula
[b] Copper deposition using IWI method

**Table 6.2**. Textural properties of the SBA-15, CeFe-*25* and *X* CuO/CeFe-*25*.

| Sample | BET surface area ($m^2/g$) | Pore volume ($cm^3/g$) | Pore diameter (nm) |
|---|---|---|---|
| SBA-15 | 951 | 1.65 | 6.9 |
| CeFe-*25* | 118 | 0.30 | 3.4 |
| *8* CuO/ CeFe-*25* | 83 | 0.26 | 3.2 |
| *12* CuO/ CeFe-*25* | 81 | 0.24 | 3.2 |
| *16* CuO/ CeFe-*25* | 73 | 0.27 | 3.2 |
| *24* CuO/ CeFe-*25* | 69 | 0.23 | 2.9 |
| *17* CuO/ CeFe-*25*[b] | 77 | 0.24 | 3.1 |

[b] Copper deposition using IWI method

Nitrogen adsorption-desorption isotherm and pore size distribution curves of CeFe-*25* and copper deposited CeFe-*25* catalysts are reported in Fig.6.5. All the catalyst exhibits typical characteristics of a mesoporous material with type IV isotherms. Similar

isotherms are reported for materials prepared with nano-casting method [19]. The Barret-Joyner-Halenda (BJH) pore size distribution for the CeFe-*25* calculated from desorption branch show a narrow distribution (Fig.6.5 (a), insest) centered at 3.4 nm (Table 6.2), which is consistent with the wall thickness of the template SBA-15. The Brunauer- Emmett-Teller (BET) surface area of the CeFe-*25* material is 118 $m^2$ $g^{-1}$, which is comparable with the values obtained from HT method using SBA-15 template [20]. It is observed that addition of copper (8-24 wt %) affected the surface area of the catalysts, it ranges between 69-83 $m^2$ $g^{-1}$. Pore volume and pore diameter of the catalysts are not more affected by the copper deposition, which range between (0.23 - 0.27 $cm^3$ $g^{-1}$) and (2.9 – 3.2 nm) (Table 6.2), respectively.

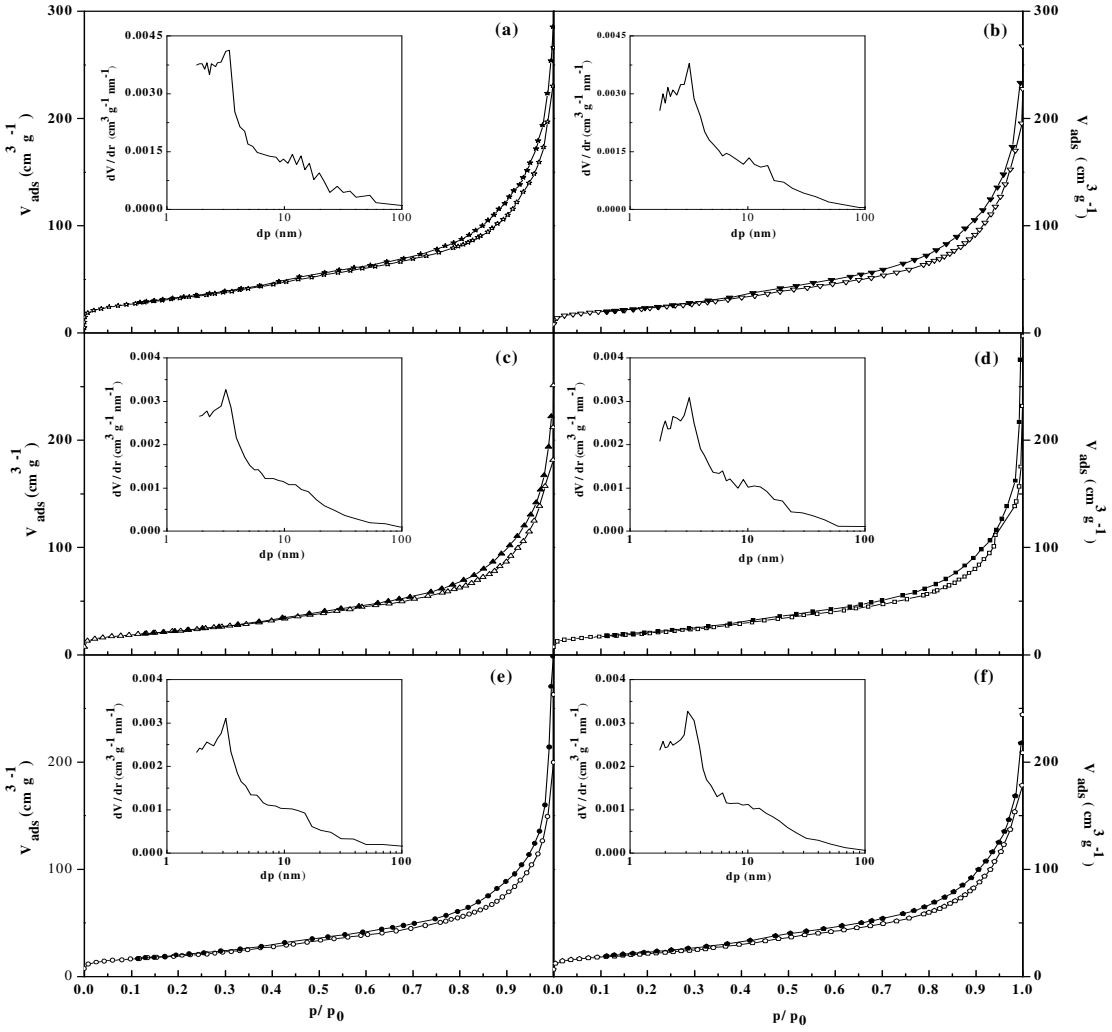


**Figure 6.5**. Nitrogen adsorption/desorption isotherm and pore size distribution plot (inset) of CeFe-*25* and CuO/CeFe-*25* catalysts: CeFe-*25*, (a); *8* CuO/CeFe-*25*, (b); *12* CuO/CeFe-*25*, (c); *16* CuO/ CeFe-*25* (d); *24* CuO/ CeFe-*25* (e); *17* CuO/ CeFe-*25* (IWI) (f).

$H_2$- temperature programmed reduction ($H_2$-TPR) analysis was carried out to study the redox behaviour of CeFe-*25* and copper loaded CeFe-*25*, the reduction profiles are reported in Fig.6.6 (A and B). It is well documented in the literature that the reduction profile of pure ceria (not shown in figure) occurs at 450 and 900°C, ascribed to the reduction of surface and bulk oxygen, respectively[21]. According to literature, $Fe_2O_3$ reduction show a sharp peak at 360°C corresponding to the reduction of $Fe_2O_3$ to $Fe_3O_4$ and a broad peak at 680°C is due to the subsequent reduction of $Fe_3O_4$ to Fe° [22-23]. The CeFe-*25* (Fig. 6.6 A) mixed oxide show a complex reduction profile. It shows sharp reduction peaks at 447, 523, and 700°C and shoulder peaks at 312, 491, and 607°C. Compared to the pure metal oxides, CeFe-*25* mixed oxide reduce at lower temperatures, it starts to reduce at 220°C. This means that the presence of iron in ceria weakens the Ce-O bond in the solid solution and promotes its reduction. Similar observation previously reported for Ce-Fe solid solution [12, 16].

The reduction profile of copper deposited CeFe-*25* solid solutions are reported in Fig.6.6 (B). The addition of copper dramatically changes the reduction features of the CeFe-*25* solid solution to lower temperatures. The reduction profile of *X* CuO/CeFe-25 shows reduction peaks of copper in the range 150-300°C, this region is characterized to the step wise reduction of $Cu^{2+}$ to $Cu^0$, this reduction behaviour is familiar for copper – ceria catalysts reported in the literature [24-25]. In *8* CuO/CeFe-25 show three peaks at lower temperatures, 175 (α), 206 (β), and 266°C (γ), among these the first two peaks, ie, α and β, corresponds to the stepwise reduction of well dispersed copper species, i.e., $Cu^{2+}$ to $Cu^{+1}$ and $Cu^{+1}$ to $Cu^0$ [26]. The peak at higher temperature (266°C, γ peak) represents the reduction of bulk copper in the surface of the support. Intensity of the third (γ) peak increases with CuO loading due to the formation of bulk CuO on the catalysts surface, which is visible in X-ray diffraction of CuO/CeFe samples reported in Fig.6.4. When the CuO loading increases the second and third peak merged to form a broad peak at higher temperatures (Fig.6.6). There are two other peaks observed in the TPR profile of CuO/CeFe-25, one at the lower temperature region (308-335°C) and another one at higher temperature region (521-588°C), which might be due to the reduction of $Fe_2O_3$ to $Fe_3O_4$ and $Fe_3O_4$ to Fe, respectively. All the CuO/CeFe systems are reduced at lower temperatures compared to pure oxide, this suggests the strong

interaction of Cu-Ce-Fe-O in the catalyst combinations, similar trend observed in the reduction of CuO/CeFe system[27].

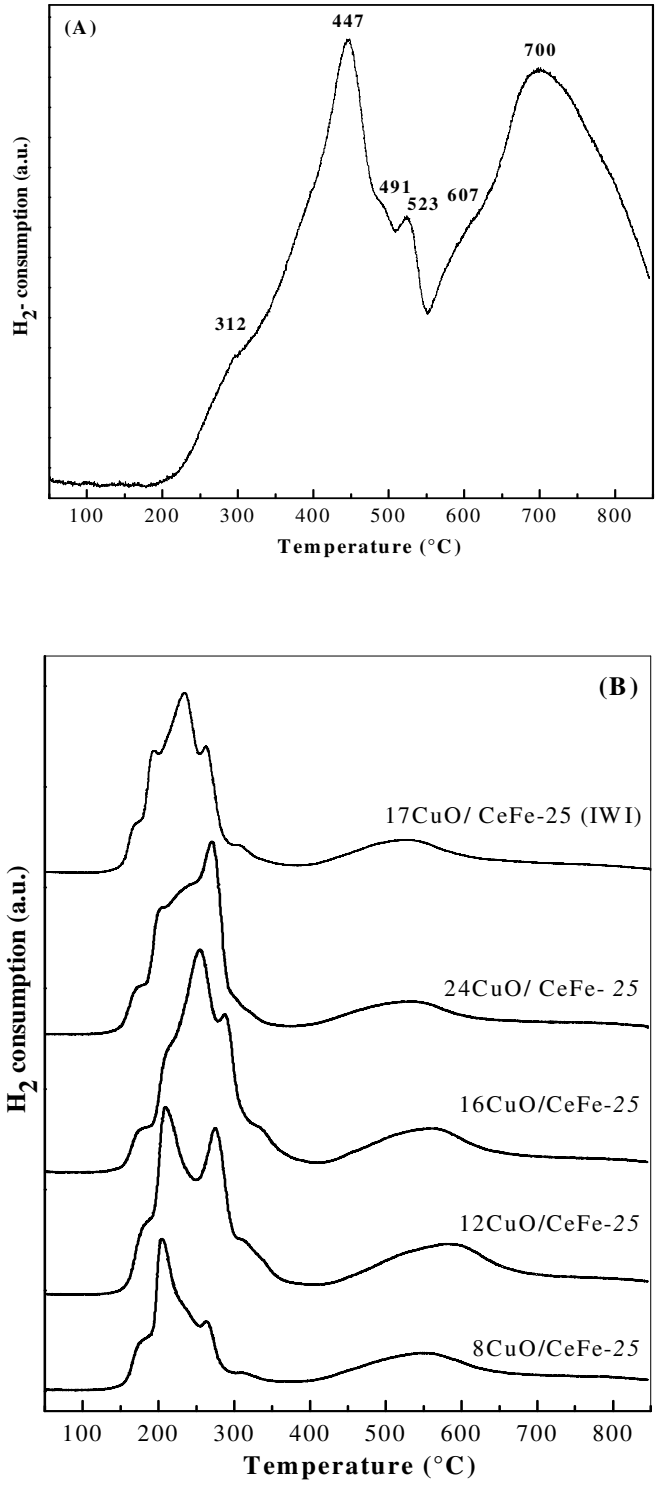


**Figure 6.6**. $H_2$-TPR of CeFe-*25*(A) and CuO/CeFe-*25*(B) catalysts: *8* CuO/CeFe-*25*, (a); *12* CuO/CeFe-*25*, (b); *16* CuO/ CeFe-*25* (c); *24* CuO/ CeFe-*25* (d); *17* CuO/ CeFe-*25* (IWI) (e).

## 6.4. Catalytic activity of CuO/CeFe-25

### *6.4.1. CO oxidation activity in the absence of $H_2$*

The catalytic activity results of CuO/CeFe catalysts for the low temperature CO oxidation are shown in Fig.6.7, where CO conversion is plotted against reaction temperature. CeFe-*25* support is inactive for CO oxidation, it starts the reaction above 120°C and no further improvement observed with the increase of reaction temperature, but the addition of copper promotes the activity at low temperatures. Copper promoted CeFe-25 starts to react at 40°C, further increase of reaction temperature results steep increase in CO conversion curve and reaches maximum conversion at 160°C (Fig.6.7). There are no remarkable differences in the activity of the catalysts, however, slight differences in temperature for 50% CO conversion ($T_{50}$) observed for *16* CuO/CeFe ($T_{50}$ of 98°C), *8* CuO/CeFe=*12* CuO/CeFe ($T_{50}$= 100°C) and *24* CuO/CeFe ($T_{50}$= 103°C) catalysts.

Effect of copper deposition method for CO conversion investigated using chelating-impregnation (CI) and incipient wetness impregnation method (IWI). The activity of the catalysts for CO oxidation is reported in Fig.6.8. There is no difference in activity observed over the catalysts prepared with chelating-impregnation (CI) and incipient wetness impregnation (IWI) method, a $T_{50}$ of 98°C observed over the catalysts. Present study observed no significant effect of CuO deposition method in CO oxidation activity. Gold deposited reducible oxides are highly active for CO oxidation reaction at low temperature, for comparison in present study we deposited gold on CeFe-*25* support. The CO oxidation activity of gold deposited and CuO deposited CeFe-*25* catalysts are reported in Fig.6.9, where CO oxidation *vs* reaction temperature is plotted. Gold deposited catalyst shows better activity for CO oxidation till 80°C beyond this point no significant difference observed in the catalytic activity of the material. Temperature for 50% CO conversion is found to be 100 and 98°C for 1.8 Au/CeFe-25 and 16CuO/CeFe-25 (CI), respectively. The performance of the copper catalysts are not superior compared to gold based catalysts, however it shows similar activity for CO oxidation. Copper based catalysts are promising alternative for CO oxidation compared to high cost precious metal catalysts.

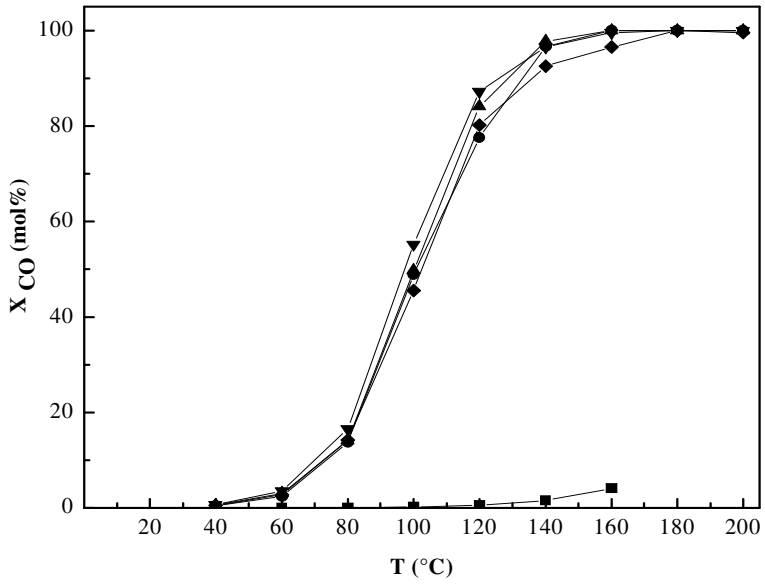


**Figure 6.7**. CO conversion *vs.* reaction temperature of the *X* CuO/CeFe-25 catalysts: (■) CeFe-*25*; (●) *8* CuO/CeFe-*25*; (▲) *12* CuO/CeFe-*25*; (▼) *16* CuO/ CeFe-*25*; (♦) *24* CuO/ CeFe-*25*.

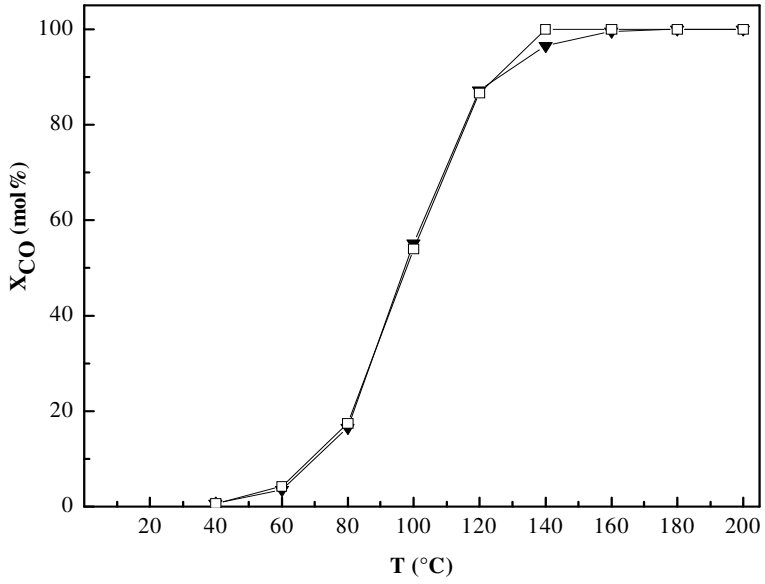


**Figure 6.8**. Effect of copper deposition method on CO oxidation of CuO/CeFe-25 catalysts: (▼)16 CuO/CeFe-25 (CI), (□) 17CuO/CeFe-25 (IWI).

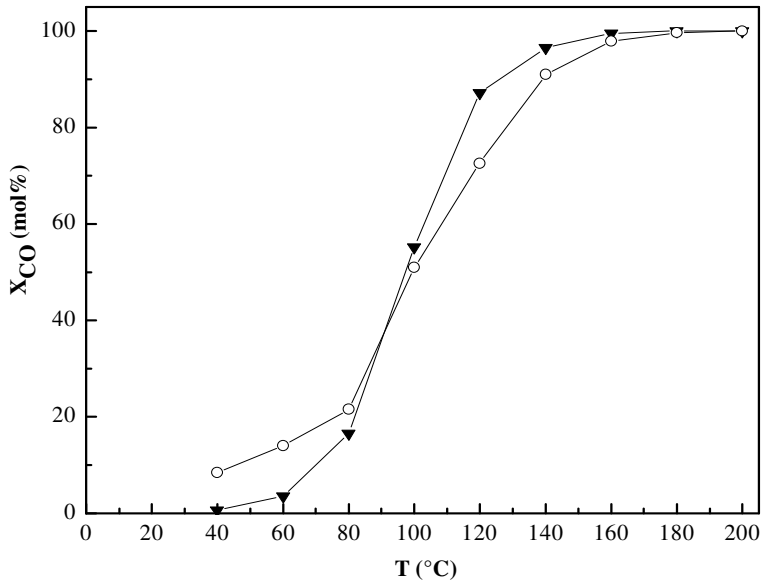


**Figure 6.9**. CO oxidation over (○)1.8 Au/CeFe-25 and (▼) 16 CuO/CeFe-25 (CI) catalysts.

### *6.4.2. Preferential oxidation of CO(PROX-CO)*

Preferential oxidation of CO in presence of excess hydrogen are reported in Fig. 6.10. CeFe-*25* support is less active in preferential CO oxidation (Fig.6.10 a), no improvement in activity observed over the support by the increase of reaction temperature, at 200°C it show a maximum CO conversion of 19 %. But the addition of copper promotes the CO oxidation activity to lower temperatures (Fig.6.10 a), there is no remarkable difference in activity observed over the CuO supported catalysts. The CO conversion as a function of temperature expresses an *S*-shaped curve. The CO conversion increases with temperature and reaches maximum at 180°C, beyond this point it drop its activity due to hydrogen oxidation and slight methane formation (Fig.6.10 b), at 200°C 0.7% of the CO is transformed to $CH_4$. The temperature at which 50% CO conversion ($T_{50}$) occurs is 111°C for 8CuO/CeFe-25 (S= 83.3), 112°C for 16CuO/CeFe-25 (S= 97.3), 113°C for 12CuO/CeFe-25(S=87), and 114°C for 24CuO/CeFe-25 (S= 93) catalysts, respectively, where the values in parenthesis corresponds to the selectivity. These values are in good agreement with the previously reported results, where $O_2$ pre-treated Cu-Ce-Fe-O catalysts show a $T_{50}$ of 115°C [27].

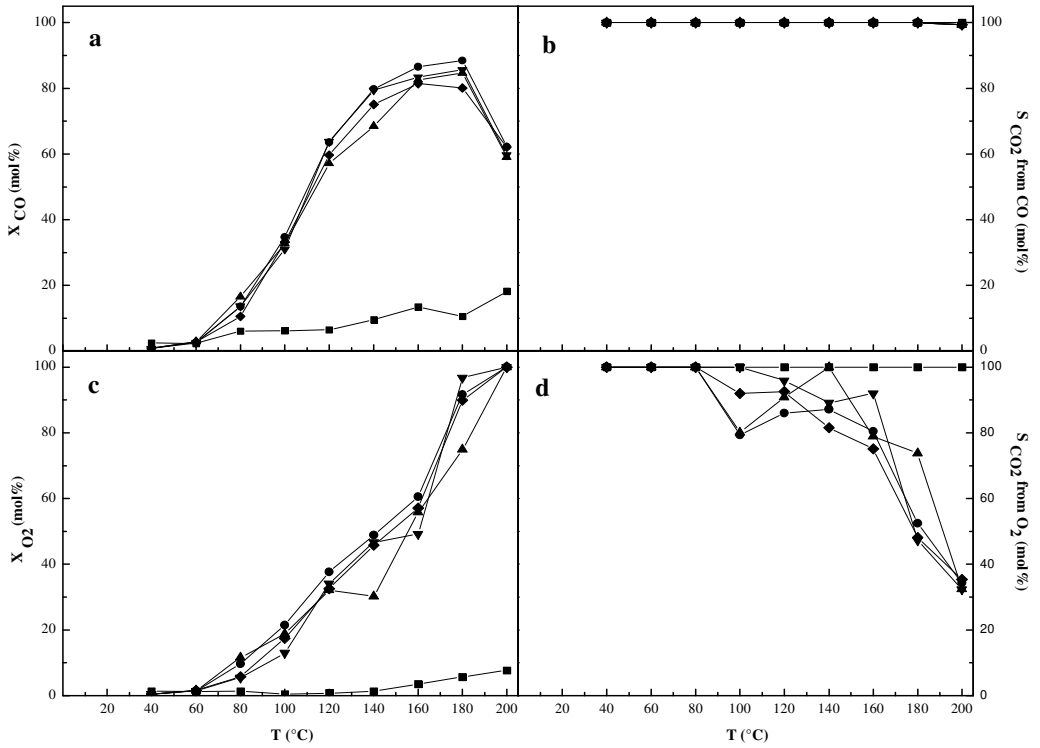


**Figure 6.10**. CO conversion *vs.* reaction temperature of the *X* CuO/CeFe-25 catalysts for PROX-CO: (■) CeFe-*25*; (●) *8* CuO/CeFe-*25*; (▲) *12* CuO/CeFe-*25*; (▼) *16* CuO/ CeFe-*25*; (♦) *24* CuO/ CeFe-*25*: (a), CO conversion; (b), $CO_2$ selectivity from CO; (c),$O_2$ conversion; (d), $CO_2$ selectivity form $O_2$. Catalyst amount: 0.03 g.

The total $O_2$ conversion over the CuO/CeFe-25 caralysts is reported in Fig. 6.10 c. All the catalysts show a steep increase in $O_2$ conversion with an increase of temperature. At 200°C, 100 % $O_2$ conversion observed over all catalysts. Compared to CeFe-*25*, it seems that oxygen conversion is favored by the presence of copper. As shown in Fig.6.10d, CeFe-25 show 100% oxygen selectivity $CO_2$ formation at all reaction temperatures, but in the case of CuO/CeFe-*25*catalysts oxygen selectivity to $CO_2$ formation is 100% till 80°C, beyond this point a sharp decrease observed over all the catalyst. At 200°C, around 35% of the reacted oxygen is converted to $CO_2$ over all copper based catalysts.

It is reported that catalyst preparation method has some influence on the catalytic activity of the catalyst[17]. To investigate the effect of preparation method, we prepared a catalyst with 17 wt% CuO on CeFe-25 using incipient wetness impregnation method (IWI). The activity of the catalysts in PROX are reported in Fig.6.11 (a-d). There are no remarkable difference in catalytic activity, however, minor difference in CO conversion activity observed over the catalyst prepared with incipient wetness

impregnation, this results is contradictory to the results reported earlier [17], where $CuO$-$CeO_2$ catalyst prepared with chelating- impregnation showed superior activity for PROX. Temperature for 50% CO conversion occurred over these catalysts are 112°C for 16CuO/CeFe-25(CI) and 103 °C for 17 CuO/CeFe-25(IWI). In 16CuO/CeFe-25 (CI) catalysts, methane formation observed at 200°C, about 0.7% of the CO is converted to $CH_4$ (Fig.6.11b), but in 17 CuO/CeFe-25(IWI) 100% conversion of CO to $CO_2$ is observed. Both catalysts show similar oxygen selectivity to $CO_2$ formation till 160°C, beyond this point 17 CuO/CeFe-25(IWI) possesses higher selectivity. At 200°C, 17 CuO/CeFe-25 (IWI) show 40% selectivity, at the same time 16 CuO/CeFe-25(CI) show 32 % selectivity to $CO_2$. There are no remarkable differences observed in the characterization data and CO oxidation activity in the absence of hydrogen over 17CuO/CeFe-25 (IWI), however, minor difference in activity for PROX might be due to the special Cu-Ce-Fe-O interaction or it behave differently in the reaction compared to 16CuO/CeFe-25(CI).

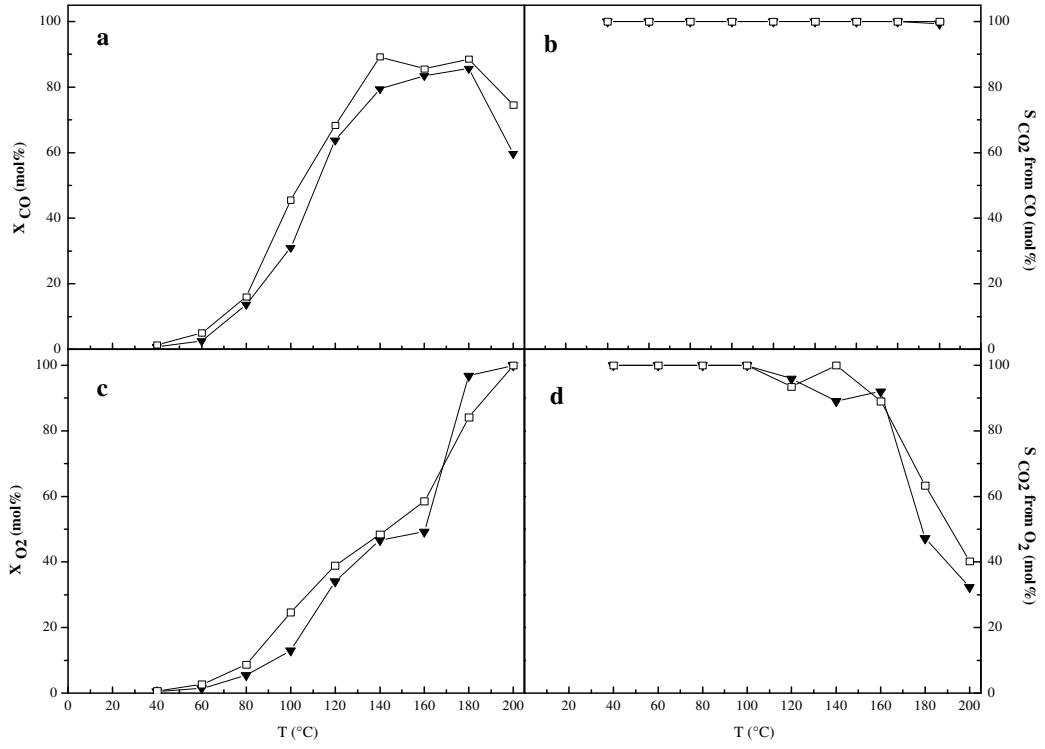


**Figure 6.11**. Effect of copper deposition method on preferential CO oxidation of CuO/CeFe-25 catalysts: (▼)16 CuO/CeFe-25 (CI), (□) 17CuO/CeFe-25 (IWI): (a), CO conversion; (b), $CO_2$ selectivity from CO; (c), $O_2$ conversion; (d), $CO_2$ selectivity form $O_2$. Catalyst amount: 0.03 g.

Gold supported reducible oxides catalysts are highly active for preferential oxidation of CO [28-29].In present study we investigated the effect gold on CeFe-*25* support for preferential oxidation of CO. For comparison activity of the copper deposited (16CuO) and gold deposited (1.8 Au) CeFe-*25* catalysts are reported in Fig.6.12. It is clear from the figure 6.12a, that gold deposited CeFe-*25* show less activity for selective CO oxidation. Temperature for 50% CO conversion observed over 1.8Au/CeFe-*25* is 164°C, at the same time 16CuO/CeFe-25 (CI) show a $T_{50}$ of 112°C. Almost similar oxygen conversion activity observed over gold and copper deposited samples (Fig.6.12c), but oxygen selectivity to $CO_2$ formation is remarkably less in gold deposited catalyst. Both catalysts show 100 % selectivity to $CO_2$ till 80°C, beyond this point a sharp decrease observed over gold deposited catalyst, it show a selectivity of 27 % to $CO_2$ at 200°C, at the same time 33% selectivity observed over 16CuO/CeFe-25 (CI) catalyst.

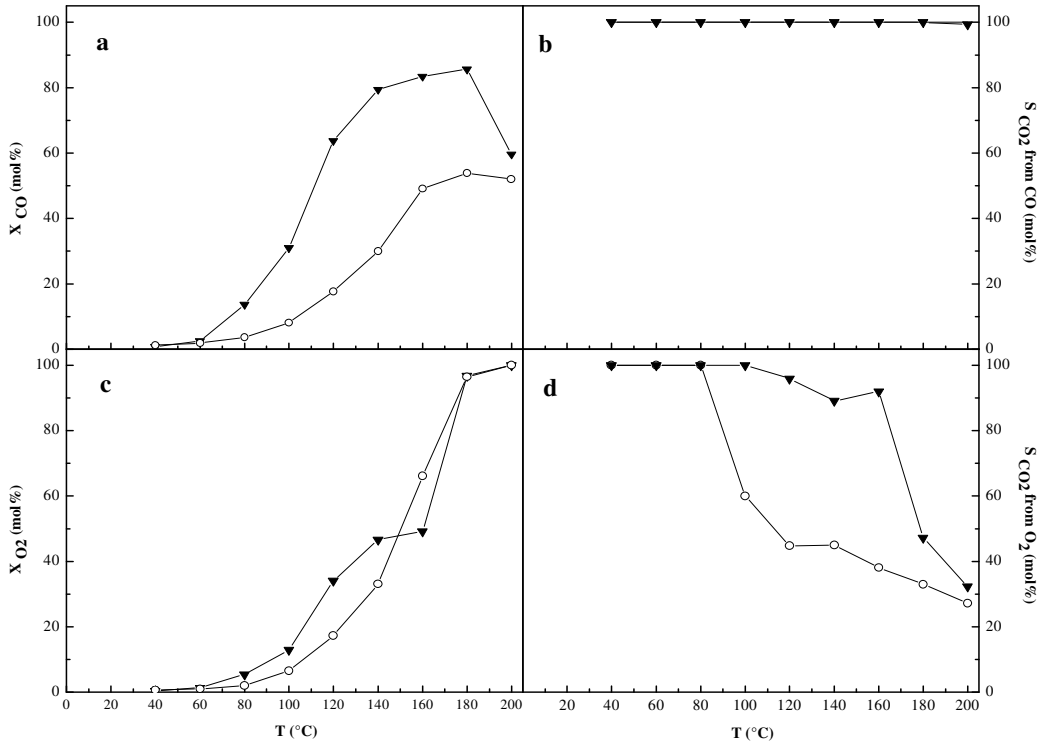


**Figure 6.12**. Preferential oxidation of CO over (○)1.8 Au/CeFe-25 and (▼) 16 CuO/CeFe-25 (CI) catalysts: (a), CO conversion; (b), $CO_2$ selectivity from CO; (c),$O_2$ conversion; (d), $CO_2$ selectivity form $O_2$. Catalyst amount: 0.03 g.

## 6.5. Conclusions

High surface area ceria-iron solid solution support prepared by hard template method. A series of copper (8-24 wt.%) deposited catalysts are prepared by chelating–impregnation method. All the catalysts possesses higher surface area, pore volume and narrow pore size distribution. Easier reducibility observed for copper deposited CeFe-*25* catalyst compared to its pure oxides. It is observed that copper remarkably increases the activity of the catalyst for CO oxidation and PROX. All the copper deposited samples showed similar activity in CO oxidation and PROX. Temperature for 50% CO conversion is observed at 98°C for 16CuO/CeFe-25(CI) for CO oxidation in the absence of hydrogen and in preferential oxidation the $T_{50}$ is shifted to 112°C for 16CuO/CeFe-25 (CI).

Effect of other copper deposition method investigated for the CO oxidation and preferential oxidation reaction. Catalyst prepared with chelating-impregnation and incipient wetness impregnation show similar activity in CO oxidation, however in preferential oxidation slight difference in activity observed over catalyst prepared with incipient wetness impregnation (IWI). A $T_{50}$ of 103°C observed over the catalyst prepared with incipient wetness impregnation (IWI) method compared to chelating-impregnation method (CI). Compared to gold deposited catalyst, copper based catalyst perform well in CO oxidation (at higher temperatures) and preferential oxidation. High activity and good selectivity observed over copper based catalyst for PROX.

## References


[1] A. Trovarelli, Catalysis Reviews 38 (1996) 439-520.

[2] S. Park, J.M. Vohs, R.J. Gorte, Nature 404 (2000) 265-267.

[3] H.C. Yao, Y.F.Y. Yao, Journal of Catalysis 86 (1984) 254-265.

[4] J.E. Kubsh, J.S. Rieck, N.D. Spencer, in: A. Crucq (Ed.), Studies in Surface Science and Catalysis, Elsevier, 1991, pp. 125-138.

[5] P. Fornasiero, R. Dimonte, G.R. Rao, J. Kaspar, S. Meriani, A. Trovarelli, M. Graziani, Journal of Catalysis 151 (1995) 168-177.

[6] E.P. Murray, T. Tsai, S.A. Barnett, Nature 400 (1999) 649-651.

[7] T. Masui, K. Fujiwara, K.-i. Machida, G.-y. Adachi, T. Sakata, H. Mori, Chemistry of Materials 9 (1997) 2197-2204.

[8] A. Trovarelli, Comments on Inorganic Chemistry 20 (1999) 263-284.

[9] A. Gupta, A. Kumar, U.V. Waghmare, M.S. Hegde, Chemistry of Materials 21 (2009) 4880-4891.

[10] G. Dutta, U.V. Waghmare, T. Baidya, M.S. Hegde, K.R. Priolkar, P.R. Sarode, Chemistry of Materials 18 (2006) 3249-3256.

[11] P. Singh, M.S. Hegde, Dalton Transactions 39 (2010) 10768-10780.

[12] F.J. Perez-Alonso, I. Melián-Cabrera, M. López Granados, F. Kapteijn, J.L.G. Fierro, Journal of Catalysis 239 (2006) 340-346.

[13] H. Bao, X. Chen, J. Fang, Z. Jiang, W. Huang, Catalysis Letters 125 (2008) 160-167.

[14] P. Singh, M.S. Hegde, Journal of Solid State Chemistry 181 (2008) 3248-3256.

[15] F.J. Pérez-Alonso, M. López Granados, M. Ojeda, P. Terreros, S. Rojas, T. Herranz, J.L.G. Fierro, M. Gracia, J.R. Gancedo, Chemistry of Materials 17 (2005) 2329-2339.

[16] C. Liang, Z. Ma, H. Lin, L. Ding, J. Qiu, W. Frandsen, D. Su, Journal of Materials Chemistry 19 (2009) 1417-1424.

[17] Z. Wu, H. Zhu, Z. Qin, H. Wang, J. Ding, L. Huang, J. Wang, Fuel.

[18] M. Haruta, Catalysis Today 36 (1997) 153-166.

[19] Y. Ren, Z. Ma, L. Qian, S. Dai, H. He, P. Bruce, Catalysis Letters 131 (2009) 146-154.

[20] J. Zhu, Q. Gao, Microporous and Mesoporous Materials 124 (2009) 144-152.

[21] X. Tang, B. Zhang, Y. Li, Y. Xu, Q. Xin, W. Shen, Catalysis Today 93–95 (2004) 191-198.

[22] Q. Yang, H. Choi, S.R. Al-Abed, D.D. Dionysiou, Applied Catalysis B: Environmental 88 (2009) 462-469.

[23] E. Rombi, I. Ferino, R. Monaci, C. Picciau, V. Solinas, R. Buzzoni, Applied Catalysis A: General 266 (2004) 73-79.

[24] M.-F. Luo, Y.-J. Zhong, X.-X. Yuan, X.-M. Zheng, Applied Catalysis A: General 162 (1997) 121-131.

[25] T. Caputo, L. Lisi, R. Pirone, G. Russo, Applied Catalysis A: General 348 (2008) 42-53.

[26] P. Zimmer, A. Tschöpe, R. Birringer, Journal of Catalysis 205 (2002) 339-345.

[27] K. Sirichaiprasert, A. Luengnaruemitchai, S. Pongstabodee, International Journal of Hydrogen Energy 32 (2007) 915-926.

[28] G. Avgouropoulos, T. Ioannides, C. Papadopoulou, J. Batista, S. Hocevar, H.K. Matralis, Catalysis Today 75 (2002) 157-167.

[29] H. Imai, M. Daté, S. Tsubota, Catalysis Letters 124 (2008) 68-73.

CHAPTER

7

# Summary and conclusions

Hydrogen is considered as the promising fuel for the future and most suitable for fuel cells. Its pollution free combustion and diversity of sources makes it an attractive alternative candidate to fossil fuels. Production of hydrogen with very low concentrations of CO is of crucial importance for the PEM fuel cell applications. The gas streams coming out from the water gas shift reactors are not suitable for the fuel cell applications. Possible way to reduce CO to a few ppm are (i) preferential oxidation of CO, (ii) CO Methanation, and (iii) pressure swing adsorption processes. Preferential oxidation is the most effective method for the trace removal of CO from the reformate stream before its introduction into the PEM fuel cell. Traditionally precious metal based catalysts are used for preferential oxidation reaction, but high cost and less availability of the precious metals extends the research to search an alternative base metal oxide catalysts without precious metals in their combinations. It is worthy to develop a base metal oxide catalyst combinations for preferential oxidation of CO. The present thesis investigate the performance of four base metal oxide catalyst combinations for low temperature CO oxidation (LT-CO) and preferential oxidation of CO (PROX-CO). Four base metal oxide catalytic systems (two of them are cobalt based catalysts and other two

are ceria based catalysts) have been synthesized, characterized and studied for CO oxidation and preferential oxidation of CO.

The first chapter of the thesis deals with the detailed introduction about the hydrogen production and purification processes. Various hydrogen production methods and catalyst systems used for the reactions are described in detail. Removal of CO from the reformate stream by using HTS and LTS adiabatic reactors, catalysts used for the processes and factors affecting the reactions are clearly described. Final CO removal using preferential CO oxidation reaction and the catalytic systems involved for the processes are described in detail. The aim and scope of the present thesis are also discussed in the introduction.

Chapter two gives the details about the catalysts synthesis method, techniques used for the characterization of the catalysts, experimental setup and conditions used for the CO oxidation and preferential CO oxidation reactions.

Chapter three describes the synthesis, characterization and catalytic activity of $Cu^{2+}$ doped cobalt oxide catalytic systems for the low temperature CO oxidation and preferential CO oxidation. Characterization results showed that the synthesized CuCo-*x* materials possess ordered rod like structure with high surface area and narrow pore size distributions. All the CuCo-*x* catalysts are active in CO oxidation but remarkable difference in activity observed above 100°C over CuCo-*x* catalysts compared to pure cobalt oxide. Reduction-reoxidation treatment of the CuCo-*x* prior to the reaction results a bad catalysts for CO oxidation. For preferential CO oxidation, copper containing catalysts show increased oxygen and CO conversion in comparison with pure cobalt oxide catalysts. CO methanation observed over Cu containing catalysts at ≥180°C due to the ease of reducibility of CuCo-*x* catalysts at lower temperature compared to pure cobalt oxide. Partial structural collapse of copper doped catalysts observed after the reaction.

Chapter four discusses the synthesis, characterization and catalytic activity of $Fe^{3+}$ doped cobalt oxide systems. For low temperature CO oxidation pure cobalt oxide catalyst showed superior activity in comparison with iron-cobalt oxide catalysts. Gold deposited iron-cobalt system found to be more active in the series for CO oxidation. In preferential CO oxidation iron doped cobalt oxide system showed improved activity and

selectivity compared to pure cobalt oxide when the reaction was carried out with higher catalyst amount. Regenerative study confirmed that the no modifications occurred on the catalysts after the reaction. No methane formation observed over iron-cobalt catalytic systems. Gold supported iron-cobalt oxide system was the worst catalyst in the series for preferential CO oxidation reaction. It showed more oxygen conversion and less selectivity to $CO_2$. Structural stability observed over the iron-cobalt catalysts after reaction, whereas partial structural collapse observed over gold supported catalyst.

Chapter five of the thesis gives a detailed report about the development of copper-ceria catalytic systems. All the copper-ceria systems are found to be active for low temperature CO oxidation and preferential CO oxidation reaction. No remarkable differences in the activity of the copper-ceria catalysts observed for low temperature CO oxidation even at higher copper loading. In preferential CO oxidation minor difference in the CO oxidation activity and $CO_2$ selectivity observed over higher copper containing catalysts ($Cu_{76}Ce$). No Methane formation observed over these systems. The selectivity observed at higher temperatures over copper-ceria catalysts are promising compared to noble metal based catalysts.

Sixth chapter of the thesis discusses the development of a copper-ceria-iron catalytic systems for CO oxidation and preferential oxidation reaction. Solid solutions of ceria-iron support are not active for CO oxidation and preferential CO oxidation at lower temperatures. Improvement in activity observed for the catalysts with copper deposition. All the copper deposited catalysts showed similar trend in CO oxidation and preferential oxidation with no remarkable differences in the CO oxidation activity. Effect of copper deposition methods investigated by using chelating-impregnation (CI) and incipient wetness impregnation (IWI) method. For CO oxidation similar activity observed over the catalysts prepared with chelating-impregnation (CI) and incipient wetness impregnation (IWI) method, but in preferential CO oxidation minor difference in CO oxidation activity observed between the catalysts prepared with chelating-impregnation (CI) and incipient wetness impregnation (IWI). For comparison, CO oxidation and preferential CO oxidation reactions are carried out over gold-ceria-iron and copper-ceria-iron catalysts. Good performance of the copper-ceria-iron catalyst observed at higher reaction temperature compared to gold-ceria-iron oxide catalyst for CO oxidation. In preferential CO oxidation superior activity observed over copper-

ceria-iron catalyst compared to gold-ceria-iron catalyst for oxidizing CO selectively. Gold-ceria-iron oxide system seem to be deactivated in presence of hydrogen.